UNIVERSITÀ DEGLI STUDI DI MILANO-BICOCCA
Facoltà di Scienze Matematiche, Fisiche e Naturali
Dipartimento di Scienza dei Materiali

Doctorate in Materials Science

XXVth cycle

Continuum models of heteroepitaxial growth on patterned substrates

Doctorate Thesis of
Roberto Bergamaschini

Supervisor: Prof. Francesco Montalenti
Coordinator: Prof. Gian Paolo Brivio

January 2013

Contents

Introduction **5**

1 Outline of crystal growth **9**
1.1 Growth modalities of heteroepitaxial systems 9
1.2 Stranski-Krastanow growth: Ge/Si 10
1.2.1 Nanometric islands 11
1.3 Plastic relaxation 13
1.4 Intermixing 14
1.5 Growth on patterned substrates 15
1.6 Growth techniques 17

2 Free energy and driving forces **21**
2.1 Dynamics equation 21
2.1.1 Non-conserved dynamics. Attachment/Detachment limited growth 22
2.1.2 Conserved dynamics. Diffusion limited growth 23
2.2 Surface energy 24
2.2.1 Equilibrium crystal shape and Wulff plot 26
2.2.2 Corner regularization 28
2.3 Elastic energy 28
2.3.1 Inhomogeneous system 30
2.3.2 Mechanical equilibrium 32
2.3.3 Flat-Island Approximation 33
2.3.4 Asaro-Tiller-Grinfeld instability 36
2.4 Intermixing and entropy 39

3 Tersoff model **43**
3.1 Model definition 43
3.1.1 Free energy definition and local chemical potentials 45
3.1.2 Two-layers model for surface segregation 47
3.1.3 MBE Deposition Flux 49
3.1.4 Surface mobility 50

3.2 Growth simulations on flat substrates . . . 52
3.3 Growth simulations on pit-patterned substrates . . . 55
3.3.1 Smoothing of single component pit . . . 55
3.3.2 Anomalous pit filling and island growth . . . 57

4 Phase-Field model 65
4.1 Phase-field approach . . . 66
4.1.1 Finite element method . . . 68
4.2 Model definition . . . 71
4.2.1 Free energy definition and local chemical potentials . . . 72
4.2.2 MBE deposition flux . . . 74
4.2.3 Local mobility: surface vs. bulk dynamics . . . 74
4.3 Single component system: mean curvature flow . . . 76
4.4 Two components system: mixing entropy . . . 78
4.5 Elasticity via Phase-Field . . . 82
4.5.1 Static mechanical equilibrium . . . 82
4.5.2 Elasticity in a solid defined by phase-field . . . 83

5 Growth model for micrometric crystal arrays on pillar patterns 85
5.1 Growth kinetics . . . 87
5.1.1 Fully faceted description . . . 90
5.1.2 Quasi-stationary solution without diffusion . . . 92
5.2 Ge/Si pillars . . . 93
5.2.1 Model definition . . . 94
5.2.2 Simulation results . . . 97
5.3 GaAs/Si pillars . . . 104
5.3.1 Model definition . . . 105
5.3.2 Simulation results . . . 107

Conclusion 113

List of publications 117

Bibliography 127

Introduction

The continuous advancing of semiconductor technologies in micro-electronics, optics, energy production, . . . , constantly demands for an improvement in the choice of suitable materials. Heteroepitaxial systems represents a class of materials that has been largely exploited to achieve such enhancements thanks to the possibility to combine properties of the different material with a large degree of customization and tuning.

Many different heteroepitaxial systems are possible, from small nanostructures (e.g. quantum dots, islands), to microscopic crystals or films. Generally such structures form spontaneously during the growth in consequence of a self-assembly process. If the growth is operated on flat undifferentiated substrate the self-assembly process can be controlled only on a rather limited extent, by properly tuning the growth conditions responsible for the material rearrangement during the growth. The possibility to achieve a major control on the formation of the different structures along the surface is highly desirable. Substrate patterning techniques strongly evolved in the last decade allowing for a better control of the system evolution through the introduction of preferential sites where the growing material can accumulate and evolve in a more controllable way. With this respect, the understanding of the mechanisms underlying the specific growth modes observed experimentally is crucial to proficiently define the optimal growth conditions for the desired behavior. Growth models for heteroepitaxial systems are then widely used on very different scales. Due to the large variability of the systems, different models need to be in general considered for the several typologies of materials and growth methods.

In this Thesis we essentially focus our attention on two different physical systems: the Stranski-Krastanow growth of three-dimensional islands on pit-patterned substrates [1], and the growth of 3D crystals on substrate patterned with pillar structures, on the micrometer size scale [2]. In order to define the appropriate way of modeling, the characteristic size and time scale of the systems should be taken into account. The typical periodicity of patterns used for island growth in Stranski-Krastanow pit is $\gtrsim$100 nm and the grown islands can in general become very large, including several milions of atoms. Deposition of few atomic layers are usually considered but the growth rate is typically slow so that the growth process lasts for minutes. The growth on pillar patterns is performed on even larger size scale, with typical dimensions of µm; also, several µm of material are deposited

so that the growth can even require hours. Evidently, an atomistic description is not feasible so that a coarsened scale must be considered. Continuum models are hence the best choice for the description of these kind of systems, as they allow to efficiently describe the overall profile evolution for long time scales, including most of the physics resulting from the underlying atomic events in an average way.

The problem of Stranski-Krastanow island growth can be mainly defined on the basis of thermodynamic arguments as it is typically obtained by slow Molecular Beam Epitaxy at temperature high enough to guarantee an effective diffusion dynamics of the atoms along the surface. Such conditions can be considered close enough to equilibrium so that the main driving force for the system evolution is the free energy minimization, although, as largely discussed in this work, thermodynamics applies only to the surface region. Thermodynamic-driven profile evolution has been object of large interest since the seminal work by *W.W. Mullins* [3], more than fifty years ago. Several models accounting for the effects of surface energy and profile faceting have been developed [4, 5]. Strain effects have also been successfully included [6, 7], offering a deeper insight on the islanding mechanisms in connection with the raise of morphological instability of a flat film [8–10]. Several studies have been devoted also to the characterization of the role of substrate patterning [11–17]. However, most of these models were based on a single component picture losing a crucial element that proved to play an essential role in the evolution of the growth process: intermixing between the deposited material and the substrate one. Some attempts to account for this effect, accounting for the evolution of the composition profile have been proposed in Refs. [18–21]. In 2003 *J. Tersoff* [22] developed a successful description of the coupled evolution of profile and composition, based on the restriction of intermixing within a small layer around the surface, that proved to be particularly well suited to capture the main physics of Stranski-Krastanow heteroepitaxial growth on flat substrate [23, 24].

In this Thesis we discuss of an extension of the original Tersoff model to the characterization of the growth on pit-patterned substrate, developed in direct collaboration with *J. Tersoff* himself. Ge/Si system is considered. In particular, a realistic description of the surface dynamics for the adatoms of both components, accounting for their different mobilities and its dependence on the local environment, is introduced into the model derivation. Simulations are then implemented for an initial pit-patterned geometry of the substrate and the evolution is investigated in comparison with the experimental phenomenology. An effect of anomalous smoothing of the substrate profile induced in the initial stages of the growth and recently observed in experiments [25] is analyzed in details and explained on the basis of simulation results. Islands formation is also inspected and their morphological evolution is considered.

Tersoff approach was proved to be effective to capture the main physical aspects related to the intermixing dynamics, crucial for the understanding of many aspects of heteroepitaxy. Some technical limitations however reduce the possibilities to extend it to

complex system geometries, in particular three-dimensional systems. In order to allow for a future study of more general problems, during this Thesis work an original phase-field model for heteroepitaxial growth has been developed [26], in collaboration with *A. Voigt* and his group. Phase-field technique was found to be particularly well suited for the analysis of surface processes [27, 28], offering an efficient way to represent the profile evolution of a free surface upon surface diffusion [5, 29–31], eventually including also strain effects [32, 33]. Multiple component systems are also considered in phase-field models for alloy solidification [34, 35]. An exhaustive model for the heteroepitaxial processes, including both surface dynamics and intermixing effects, is not yet available in literature. The purpose of this part of the Thesis then consists in the definition of a suitable model accounting for such peculiar features of Stranski-Krastanow heteroepitaxial systems. A proof of concepts is provided by example simulations, testing the effects of the various contribution defining the problem.

The modeling of the growth processes leading to the self-assembly of crystals on pillar patterned substrates is much different as the growth in this case is obtained in conditions of high growth rates and relatively low temperature, driving the system well far from equilibrium, in conditions such that the thermodynamic driving forces are frustrated by kinetic effects. In this case, a different approach is needed, properly accounting for the different kinetics at the surface. In particular, a modeling for such conditions can be defined by exploiting the local mechanisms of atomic exchange between the grow flux and the advancing crystal front by means of suitable rate equations [36, 37]. The dynamics on the different facets of crystals is then characterized in terms of an orientation dependent growth rate, mainly determined by the impinging flux. In this Thesis a model including both intrinsic different growth properties and local deposition fluxes is defined and used to interpret the growth of micrometric 3D crystals on a suitable pattern of pillars, obtained in experiments for both Ge/Si [2] and GaAs/Si [38] pillars. Simulation results allow to inspect the key features of the observed growth modality, showing the crucial role of frustrated diffusion and mutual flux shielding between neighboring crystals. A close comparison with the experiments is reported.

This Thesis is organized as follows. In *Ch. 1*, an initial general introduction describing the main concepts of heteroepitaxial growth is reported, focusing in particular on the Stranski-Krastanow growth modality, typical of Ge/Si or InGaAs/GaAs systems, leading to the formation of self-assembled 3D islands. Effects of plastic relaxation and intermixing are also discussed. The role of substrate patterning is then discussed and the effects of different growth techniques are shortly introduced.

Then thermodynamic-based models are discussed in *Ch. 2*,*Ch. 3* and *Ch. 4*.

In *Ch. 2* the general description of a thermodynamic-based dynamics is discussed and transport equations are defined in a general way on the basis of local chemical potentials (*Sect. 2.1*). Then the different contributions to the system free energy (and hence chemical

potentials) are presented. In *Sect. 2.2* surface energy is defined and the effects of anisotropy are discussed. The elastic energy is introduced in *Sect. 2.3*. The general definition of mechanical equilibrium is given in *Sect. 2.3.2* and the Flat-Island approximation for the definition of the surface strain is derived in *Sect. 2.3.3*. Finally, in *Sect. 2.4*, the effects of mixing in a two component system are defined and, in particular, the entropy of mixing is determined.

In *Ch. 3*, Tersoff model is discussed and derived from the general definitions in *Ch. 2*. An extension of the model in literature [24] is discussed. Simulation results are reported for the growth on flat substrate in *Sect. 3.2* and on pit patterned substrates in *Sect. 3.3*. In particular, a detailed analysis of the initial growth stages is considered, leading to anomalous fast-pit filling are investigated in details.

In *Ch. 4* an original phase-filed model is derived for the characterization of thermodynamic-driven evolution for Stranski-Krastanow systems [26]. Firstly, in *Sect. 4.1* the main aspects of the phase-field approach are outlined and a brief description of the Finite Element Methods is reported *Sect. 4.1.1*. Then, in *Sect. 4.2*, the model is defined by deriving the equations for dynamics and free energy with respect to the phase-field description of the system. Applications are then discussed starting from the simple case of single component system (*Sect. 4.3*) and then considering the mixing effect for two component systems (*Sect. 4.4*). Finally the elastic effects are included in *Sect. 4.5*.

A fully-kinetic modeling of growth process is instead discussed in *Ch. 5*, where the growth of micrometric crystal arrays on deeply patterned substrates is studied. In particular, the model is introduced in *Sect. 5.1* and defined for a fully faceted description (*Sect. 5.1.1*) and quasi-stationary conditions (*Sect. 5.1.2*). Then the model is applied for the characterization of the growth of Ge 3D crystals on Si pillars by LEPECVD in *Sect. 5.2* [2] and for the case of MBE growth of GaAs crystals on the same Si patterning in *Sect. 5.3* [38]. In both cases, simulation results are successfully compared with experiments.

Finally, conclusions and final remarks are reported and future perspective are discussed.

1

Outline of crystal growth

Heteroepitaxy consists of the growth of two different crystalline materials A and B such that the growth of material A on the substrate of B preserves the crystalline structure of this latter leading to a single-crystal. Many semiconductors can be grown this way by means of several different growth techniques [39].

In this Chapter a short review of heteroepitaxial growth of semiconductors is reported to offer an overview of the main physical aspects characterizing the systems object of the models presented in this Thesis. In particular, the prototypical Ge/Si system is considered in details, not only because of its technological relevance but also because it is rather simple, compared to other heteroepitaxial systems such as III-V compounds, and because of the large availability of data in literature.

1.1 Growth modalities of heteroepitaxial systems

Three different growth modalities can be distinguished for a generic AB heteroepiaxial system [40], sketched in *Fig. 1.1*:

a) *Frank-van der Merwe*: the growth proceeds layer-by-layer, conformal with the substrate, thus leading to 2D films;

b) *Stranski-Krastanow*: an initial conformal layer, named wetting layer, is formed and then 3D structures, called islands, grow on top of it;

c) *Volmer-Weber*: 3D islands grow from the very beginning as new layers can form only on top of those already existent.

The distinction between layer-by-layer growth a) and islanding c) can be easily explained on a thermodynamic basis, by considering the balance of the energies of the free surfaces of A and B (namely γ_A, γ_B) and that of their interface γ_{AB}. In particular, if $\gamma_A > \gamma_B + \gamma_{AB}$ the substrate surface is energetically unfavored so that species B wets the

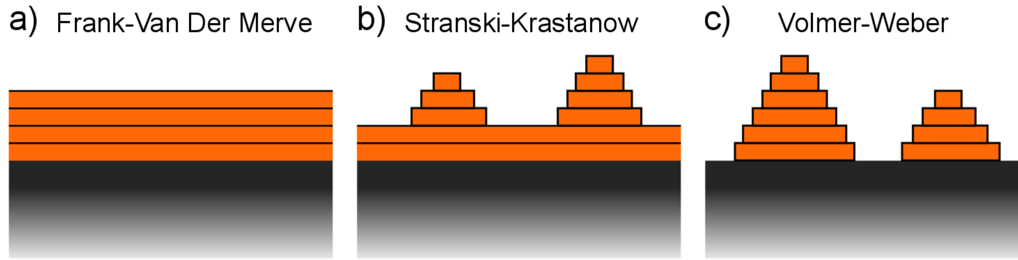

Figure 1.1: Schematic representation of the different growth modality for an heteroepitaxial system.

substrate surface forming a continuous layer as in a). On the opposite case, the surface of B and/or the AB interface are energetically unfavored and hence the growth proceed by forming islands as in c), minimizing the exposure of such surfaces. The explaination of Stranski-Krastanow growth requires to define also a volume contribution to the energy definition, accounting for the elastic energy accumulated during the growth. At the beginning, no volume contribution is present and the species B is found to wet the substrate A according to the condition $\gamma_A > \gamma_B + \gamma_{AB}$. When the thickness of the wetting layer increases the elastic volume energy grows and, at some point, becomes dominant on the surface term thus inducing the island formation to reduce the strain.

The description here considered is based on the assumption of an ideal system at equilibrium. It is evident that the presence of defects, such as dislocations, can play a role during the growth, leading for example to the suppression of island formation in Stranski-Krastanow and favoring the growth of flat films [41]. Kinetic effects, such as diffusion barriers at step edges or Ehrlich-Schwoebel barriers [42], as well as the growth conditions, e.g. temperature, deposition flux, or introduction of surfactants, can also deviate the evolution from the expected thermodynamic behavior.

1.2 Stranski-Krastanow growth: Ge/Si

The general phenomenology of Stranski-Krastanow growth was already introduced in *Sect. 1.1*, where the evolution was identified as a two steps process involving the initial growth of 2D layers followed by 3D islanding. The transition from the two modes is determined by the rise of elastic effects due to the lattice mismatch between the two components. For the generic heteroepitaxial growth of a material A on a B substrate, a misfit is defined as the deformation of the species A forced to the lattice parameter of the B substrate:

$$\varepsilon_0 = \frac{a_{\mathrm{B}} - a_{\mathrm{A}}}{a_{\mathrm{A}}} \tag{1.1}$$

The characterization of realistic Stranski-Krastanow growth is complex and demands for a more detailed analysis. In particular, in the following we discuss the actual behavior of the prototype Ge/Si(001) system as representative of the behavior of other typical Stranski-Krastanow systems (e.g. InGaAs/GaAs).

Si and Ge have the same diamond crystallographic structure but differ in the lattice parameters (*Fig. 1.2* a): a_{Ge}=5.65 Å and a_{Si}=5.43Å. A misfit of $\sim -4\%$ is then present, accounting for the compression of Ge at the smaller lattice parameter of Si. Because of this strained state, elastic energy is accumulated during the growth so that the energetics of the system is determined by the balance between such volumetric contribution and the energy associated to the free surfaces. In particular, ab-initio calculations [43, 44] showed that Ge surface energy γ_{Ge} is lower than Si surface energy γ_{Si} so that, if strain were not present, the growth of flat Ge films would be favored at all stages, according to the Frank-Van der Merwe growth modality (*Sect. 1.1*).

Fig. 1.2 schematically illustrates the evolution of Ge/Si heteropitaxial growth. As $\gamma_{\mathrm{Ge}} < \gamma_{Si}$, the initial stages of the growth are dominated by the tendency of Ge to cover the substrate leading to a flat pseudomorphic *Wetting Layer*. As indicated in *Fig. 1.2* b), atoms in the wetting layer are arranged in order to match exactly the underlying Si lattice and hence they are force in a compressed state, experimenting a biaxial strain in the growth plane equal to the misfit $\varepsilon_{/\!/} = \varepsilon_0$. As the free surface do not imply any constrain on the atomic positions, a partial relaxation of the misfit strain can be obtained by expanding the cells along the direction perpendicular to the growth plane. Ge cells are then distorted in a tetragonal way. As the thickness of the WL increases, elastic energy linearly increases into the growing film up to a point (∼2–3 ML for pure Ge/Si) where it becomes dominant on surface effects and induce a transition from 2D layers to 3D islands [1, 45–47], sketched in *Fig. 1.2* c), allowing a better relaxation of the accumulated strain thanks to the lateral expansion on the island sidewalls that reduce the compression of Ge cells. Such island are typically of nanometric size and are spontaneously formed by self-assembly.

1.2.1 Nanometric islands

The general picture of Stranski-Krastanow growth in real systems is in general complicated by many different aspects. One of them is the anisotropy of the surface energy, allowing for the formation of different island morphologies [1, 46, 47] with well-defined facets, corresponding to minima in the surface energy. An example of the islands obtained for Ge/Si(001) is reported in *Fig. 1.3*. In particular, two different morphologies, typical of the Ge/Si(001) system, can be distinguished. Smaller islands exhibit a pyramidal shape, bounded by shallow {105} facets, very effective to release the strain. Larger islands have a multifaceted shape, mainly characterized by (001), {105}, {113} and {15 3 23}, corresponding to stable orientations for Si and Ge surfaces. The appearance of steeper facets at larger volumes is due to their higher efficiency in relaxing the strain [48, 49]. As evident from *Fig. 1.3*, the typical distribution of islands size observed in the experiments [50, 51] is bimodal, indicating the coexistence of both pyramids and dome-shaped islands, as evident in *Fig. 1.3*.

Actually, a larger variety of island morphologies has been observed for Ge/Si(001),

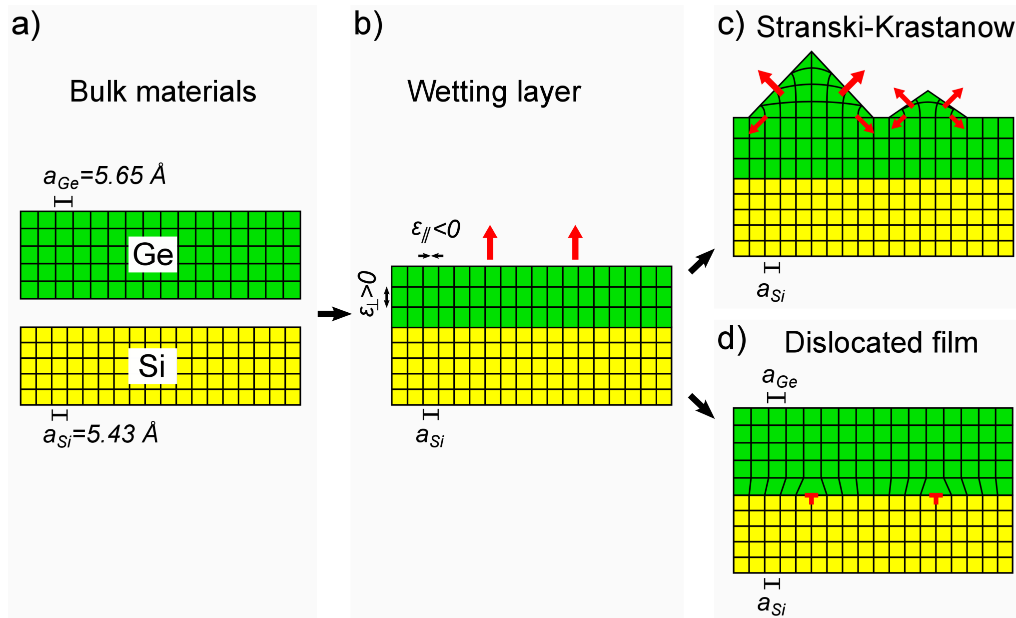

Figure 1.2: Schematic representation of the mechanisms of heteroepitaxial growth of Ge on Si substrate. In a) the two bulk materials are compared showing the existence of a lattice mismatch. In b) the formation of the wetting layer is shown, associated to a tetragonal distortion of Ge cells. In c) the Stranski-Krastanow growth is sketched. The appearance of islands on the substrate allows for elastic relaxation as indicated by the arrows. In d) the out-of-equilibrium growth of Ge dislocated flat films, as consequence of plastic deformation, is reported.

following the general trend of growing higher in the height-to-base aspect-ratio (a.r.) at increasing volume, as more elastic relaxation balance the cost due to the increased extension of the free surfaces. At early growth stages very shallow (a.r.<0.1) pre-pyramids were observed [52]. Then {105} pyramids are formed (a.r.$\sim$0.1) but also elongated {105} huts have been recognized [53]. At higher a.r. ($\sim$ 0.2) domes appear, followed by steeper (a.r.$\sim$0.3) multifaceted geometries, including {111} facets, named barns [54, 55]. The transition from one morphology to the other is determined by the interplay of surface energy cost, favoring shallow geometries, and elastic relaxation, favoring steeper structures.

The energy balance involved in shape transitions of the islands is in general extended also to the underlying wetting layer. As discussed in Ref. [56], in fact, once formed, the wetting layer is not static but its evolution is strongly coupled with the islands energetics and evolution. In particular, at the onset of the pyramid-to-dome transition, a strong thinning of the wetting layer thickness was observed, direct consequence of the enhanced stability of domes, not only with respect to the pyramids, but also with respect to the wetting layer itself. In particular, the wetting layer thickness, that at the onset of dome formation was found to be $\gtrsim$ 4 ML, was observed to decrease up to a stationary value of $\sim$3 ML. The origin for such an effect was found in the decrease of wetting layer surface energy at increasing thicknesses [57].

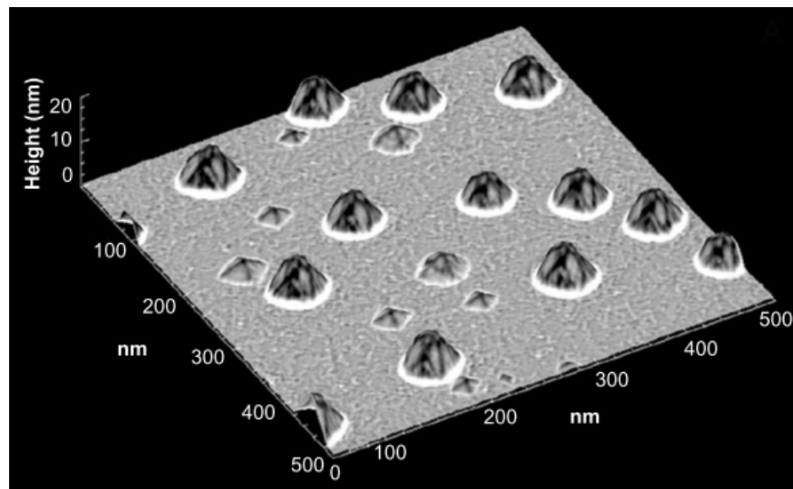

Figure 1.3: AFM image from Ref. [50] showing Ge islands grown on a flat Si(001) substrate. Both small pyramids and larger dome shaped island morphologies are distinguishable.

1.3 Plastic relaxation

So far we assumed that the system was grown in experimental conditions such to follow the equilibrium behavior thus leading to the formation of islands in order to relax the elastic strain accumulated in the wetting layer. This thermodynamic path can be however hindered by growth conditions well far from equilibrium, usually corresponding to high growth fluxes and low temperatures. In such conditions, in fact, the dynamics of the system is too slow compared to the deposition process and hence the wetting layer can grow overcritical with no change in morphology. In such a case, additional strain is accumulated up to a value large enough to determine a plastic permanent deformation in the solid through the introduction of interfacial defects such as misfit dislocations [41], as sketched in *Fig. 1.2* d). Dislocations are linear defects very effective to release the strain so that, as the dislocations are formed, the strain accumulated in the film is released. The driving force for islanding then cease to exist and the system can grow up to form thick flat films [41]. A critical thickness can be identified for the nucleation of dislocations, $\sim$nm for Ge/Si, normally higher than the critical value for island growth. Islanding is then the first process available for strain release and can be suppressed only for non-equilibrium growth conditions.

The formation of dislocations is also observed into the islands when their volume become very large. In such conditions, in fact, the elastic relaxation associated to the 3D morphology becomes less effective than the plastic relaxation provided by dislocations so that their formation and development into the islands becomes favored [54]. Dislocated islands (called superdomes for Ge/Si growth [58]) are usually characterized by much larger volumes because of the stabilizing effect of the dislocation.

Finally, it must be pointed out that the effects of dislocations on devices is detrimental

for both electronic and optical properties, so they are undesired defects that must be properly considered, especially when flat thick films are needed.

1.4 Intermixing

The growth of heteroepitaxial systems is in general influenced by the occurrence of intermixing between the deposited atoms and the substrate ones. This effect is mainly driven by entropic effects [22] and results from the mechanisms of atomic exchange. Such processes are however active only within the first few, 2–3 ML from the surface [60]. Furthermore, bulk diffusion is practically negligible on the time scale of the growth processes, so that intermixing is effective only at the surface. These effects are an essential part of the modeling we are going to discuss in *Ch. 3* [25].

Photoluminescence measurements for Ge/Si heteroepitaxial growth [61] indicated that intermixing occurs from the very beginning of the deposition process, even when the wetting layer is still growing. As islands are formed, stronger intermixing is observed [59], lowering the Ge content inside the islands up to values that, at high growth temperature, can be less than 50%, even when the growth proceed by pure Ge deposition, as shown in *Fig. 1.4*. The main reason for this large flow of Si into the island can be envisioned in the formation of deep trenches [62] right along the island perimeter, where the island is forced in a compressive state pressing the layers below as indicated by the arrows in *Fig. 1.2* c). Such trenches firstly carve the wetting layer and then penetrate into the substrate, thus moving Si toward the surface [24]. The larger grow the islands, the more extended are the trenches and hence the more Si is made available for intermixing.

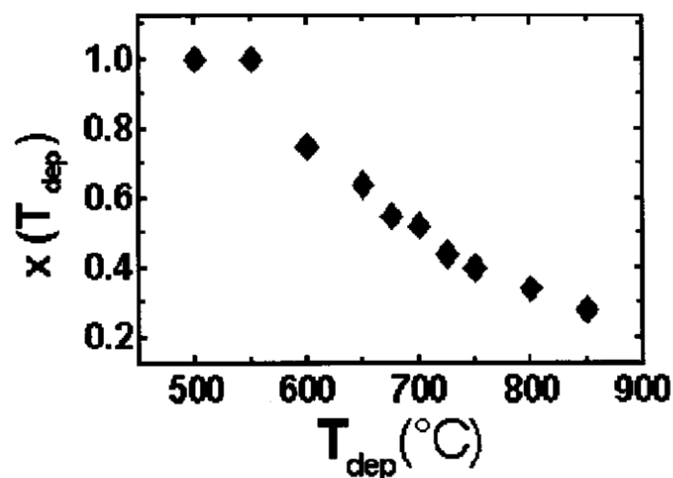

Figure 1.4: Experimental results from Ref. [59], showing the different composition (in Ge fraction x), of the epilayer grown by Ge deposition at different temperature T_{dep}. An average value, including islands, is considered. Notice how the Ge content fall to very low values as the temperature is increased, indicating strong intermixing.

On average, the introduction of Si into the island permits a partial relaxation of the strain as the mismatch between the substrate and a diluted island is smaller. Correspondingly the evolution of the island itself is changed by this relaxation, delaying to larger volumes the transition to steeper island morphologies (e.g. the pyramid-to-dome transition [49]) and also the onset of plastic relaxation [63].

More precisely, as the Si flow is driven only by surface diffusion and originates from the trenches region, a profile of composition is observed into the islands. An exhaustive explanation for this is not yet available. The main driving force for Si redistribution is the entropy of mixing but also elastic effects must be accounted for since the different composition profile may lead to better strain relaxation. In particular, an enrichment in Ge at top of the islands, mainly at the vertex where the strain is lower, has been observed and predicted [64, 65]. However, the magnitude of such effect is rather small (even less than 10% along the island profile). As the entropy of mixing is stronger at high temperature, intermixing effects are expected to increase, thus leading to a reduction of the average Ge content in the islands, as observed in *Fig. 1.4*.

1.5 Growth on patterned substrates

It is more than a decades that the heteroepitaxial growth on patterned substrate is object of deep interest as an effective way to control and eventually pilot the evolution of the system towards the desired results. From a general point of view, the purpose of patterning the substrate consists in the creation of different regions on the surface, behaving as preferential sites where material can accumulate and produce specific structures. The continuous advancement of the nano-lithographic techniques allowed to constantly improve the quality of substrate patterning permitting a proficient application of this approach to very different systems and growth conditions.

The typology of the pattern can be much different according to the specific system considered and to the experimental techniques employed for its realization. In most cases, the pattern consists of modifications of the substrate morphology to create suitable structures, such as pits of different shape and size forming ordered arrays (see *Ch. 3*)[66–68], mesa or stripes regularly distributed one parallel to each other [69, 70], or still excavating some areas of the substrate leaving pillars or ridges of proper geometry (see *Ch. 5*) [2, 38]. Several experimental methods can be used to generate this kind of structures, such as reactive-ion etching [71, 72], nano-imprint [73], electron-beam lithography [74], Focus Ion Beam manipulation [75].

Other possibilities consists in the use of masks, e.g. SiO_2 for Ge/Si growth, leaving windows on the substrate where the deposited material can accumulate and grow (this procedure is called Selective Area Deposition) [76–78]. Ordered arrays of defects, e.g. dislocations [79], can behave as preferential nucleation sites for island growth; similarly buried islands can drive the alignment of other stacked structures [80].

One of the main goals of growing on patterned substrate for Stranski-Krastanow systems consists in the possibility to obtain ordered arrays of islands with the same shape and a narrow size distribution [66, 68]. A pit patterned substrate is particularly efficient for this purpose, driving the nucleation of the islands in specific positions, depending on the pit size: large shallow pits favors the formation of islands at the center of the pit, as consequence of a dominant capillarity effect [66, 71]; narrow FIB patterned pits acts in the opposite direction, leading to nucleation on the region in between because of edge relaxation effects [75]. By controlling the pattern geometry and the growth conditions, it is possible to obtain almost perfect ordering of the islands. Furthermore, as each pit is surrounded by the very same environment, all islands are expected to have the same capture zone and then to grow with rather similar rates [81]. Because of this all islands have rather similar size leading to a narrow size distribution that could not be achieved for the growth on flat substrates. Furthermore, at variance from the flat case, the distribution is mono-modal, i.e. no different shapes are expected as all islands evolve in the very same way. Different morphologies are observed during the growth, with analog shapes of those observed on flat substrate. Pyramids are initially formed for small volumes and then evolve towards higher aspect-ratio as the volume increases forming domes and barns [72]. An example of the island ordering is shown in *Fig. 1.5* where a pit patterned Si substrate (shown in panel a) is used to control the formation of islands after Ge deposition. The result of the growth, shown in panel b), is an ordered array of islands closely resembling one with each other (an enlarged view of one of such islands is shown in panel c).

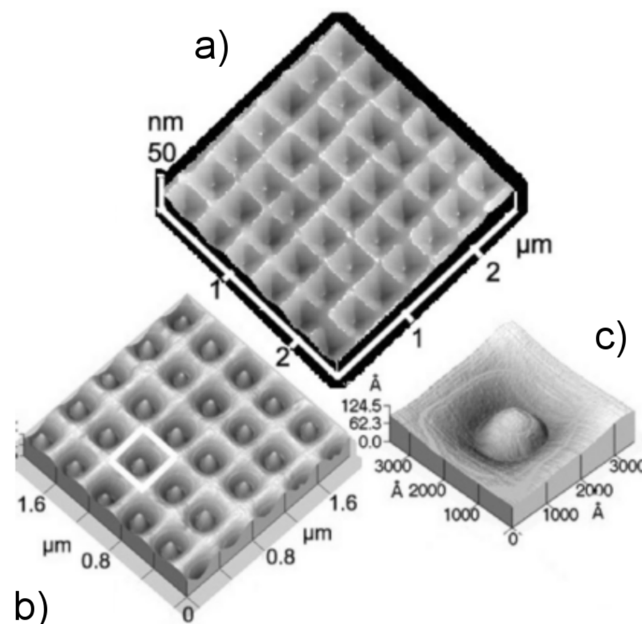

Figure 1.5: AFM characterization of Ge growth over a Si pit-patterned substrate (from Ref. [66]). a) Original Si pattern before Ge deposition. b) Profile after deposition of 4 ML Ge showing island formation into each pit. c) Enlarged view of an island.

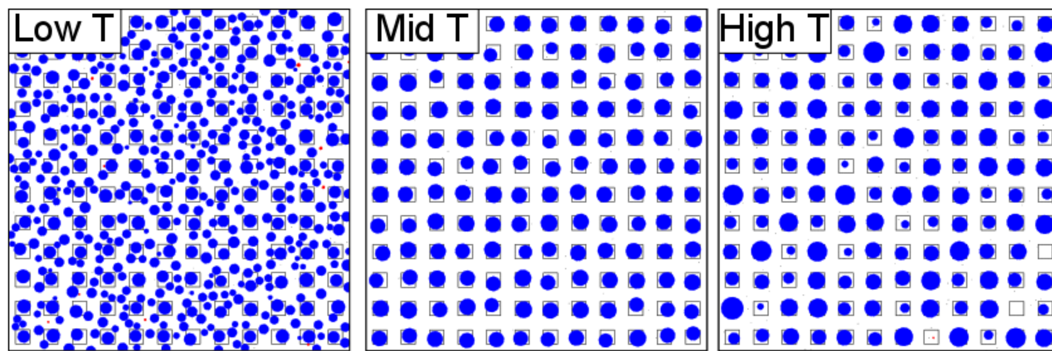

Figure 1.6: Results from "quasi"-Kinetic Monte Carlo simulations presented in Ref. [81], showing the different growth regimes obtained when depositing the same amount of material at different temperatures. In the figure, circles represents the island and their area is proportional to the actual size in 3D.

Of course the effect of the pattern depends on the specific growth conditions and only for certain parameters the hoped-for ordering effect is observed. In Ref. [81], the role of the growth parameter was investigated by means of "quasi"-Kinetic Monte Carlo simulations revealing the existence of an optimal range of growth parameters, depending on both temperature and deposition flux. In particular, as showed in *Fig. 1.6* at low growth temperature islands nucleates indifferently inside and outside of the pits so that no selectivity is obtained. At intermediate temperature the ordering is obtained and islands are very homogeneous in size, realizing the optimal growth. Finally at high temperature, islands nucleate only inside the pits but can interact one with each other undergoing Ostwald ripening and assuming more differentiated dimensions. The physical origin for such behavior was found in the different diffusion length compared to the pattern periodicity, leading to the best results for values close to each other.

Si-Ge intermixing plays an important role also during the growth on patterned substrates [25]. Effects of strain relaxation in the pits can enhance the island stability and delay the formation of dislocations to larger volumes [82, 83].

1.6 Growth techniques

Heteroepitaxial growth can be in general performed by many different techniques, such as Molecular Beam Epitaxy (MBE), Chemical Vapor Deposition (CVD), Metal-Organic Vapor Phase Epitaxy (MOVPE), ... In principle, it can be obtained both from liquid-phase and gaseous-phase. Here we limit our discussion to the latter case as it is the most used for semiconductors.

From a general point of view, the deposition process from the gaseous phase onto a solid substrate can be described as an out-of-equilibrium process where the gas is in a supersaturated state thus transferring material at the surface. The degree of such

supersaturation as well as the pressure in the growth chamber substantially determine the deposition flux.

In particular, if the growth flux is small enough to allow the diffusion processes at the surface, atoms landing on it can in general explore wide areas on the surface and crystallize in the most favorable sites. In this case, the growth is close to the equilibrium as the atom distribution can rearrange according to the thermodynamics. On the other hand if a very high flux is considered, the motion of atoms on the surface is limited to very short distances thus hindering the thermodynamic global rearrangement process. In this case the growth occurs far from equilibrium and is mainly determined by kinetic effects. Since diffusion processes depend on temperature, the flux conditions for this two regimes are relative to the growth temperature. The higher is the growth temperature, the more the system is expected to follow thermodynamics. In order to realize growth conditions dominated by kinetics, low temperature and high growth flux are required.

The experimental techniques available for semiconductors heteroepitaxy fully span all this conditions allowing to growth samples from an atomistic scale up to several µm, with corresponding fluxes typically ranging from fractions of atomic layer to tens of layers per second ($\sim 10^{-2}$–10 ML/s). A general introduction to the different growth techniques can be found in textbooks [39, 84]. In this Thesis all results are obtained by means of MBE and Low-Energy Plasma-Enhanced CVD (LEPECVD) leading to much different growth conditions.

MBE is an ultra-high vacuum technique based on the transfer of atoms onto the growing sample by means of atomic beams. Atoms are emitted from Knudsen evaporation cells in a well collimate beam that impinges on the surface with no deflection or collisions. The atomic transport is substantially ballistic thanks to the ultra-high vacuum thus permitting a precise directionality of the flux. To obtain homogeneous growth conditions on the overall sample, this is typically put on a rotating support and heated to higher temperature in order to activate diffusion processes at the surface. Multiple cells can be employed on the same growth device thus allowing to simultaneously transfer different chemical species to obtain alloyed systems, e.g. SiGe, AlGaAs, ... Each emitter is controlled by a shutter in order to start and stop the growth for the given component. Low fluxes of material are in general available, typically of order of fraction of atomic layer, i.e. $\sim 10^{-2}$–10^{-1}ML/s. The slow income of material combined with heating of the sample usually allows for quasi-equilibrium growth conditions, i.e. atoms can in general diffuse on the sample and reorganize according to thermodynamics. In particular cases (see *Sect. 5.3.1*), high growth rates, up to ∼ML/s, and short diffusion lengths (e.g. for high partial pressure of As in GaAs epitaxy, such to determine almost immediate crystallization of Ga [85]) can be obtained.

LEPECVD [86] consists of a specific implementation of the standare Chemical Vapor Deposition, allowing for low-temperature and high-growth rate for epitaxial growth of Si or Ge. In general, in CVD the deposition process is based on the reaction of chemical

species in the region of the sample. The standard CVD growth of Si and Ge is based on the thermal decomposition of reactive molecules, such as SiH_4 and GeH_4. This process is mainly effective on the surface and is limited by the slow desorption of H atoms. In order to obtain higher growth rates, high temperature is needed, but this is imply an higher thermal budget and reduce the possibility of direct CMOS integration. An alternative way to enhance the growth rate consists of using a plasma (PECVD), as it permits to induce cracking of the molecules directly in the gas phase, producing reactive neutral radicals and ions that, impinging on the surface favor the removal of H and increase the adatom surface mobility, even at low temperature. The bombardment of the surface, if the energy of the ions is too high, may lead to damage effects and poor quality of the grown material. LEPECVD permits to solve this problem by using a low energy plasma such to limit the energy of the ions at appropriate values, such that no damage occurs. This way, rates of $\sim$nm/s ($\sim$10 ML/s) are obtained even at low temperature. Because of this high rates and low temperature, the sample grow in a regime where kinetic effects have a prominent role with respect to thermodynamics.

2

Free energy and driving forces

When considering a system close to thermodynamic equilibrium its evolution in time can be consider a direct consequence of its tendency to realize such equilibrium state. All transport processes are then determined by a thermodynamic driving force directing the system towards the minimization of its free energy.

The general definition of Gibbs free energy G includes both entalphic (H) and entropic (S) contributions:

$$G = H - TS = U + pV - TS \tag{2.1}$$

where T is the temperature. The enthalpic contribution is split into the system internal energy U and the pressure-volume work pV.

For the case of interest of Stranski-Krastanow heteroepitaxial systems, surface energy, elastic energy due to the misfit strain and a contribution due to the intermixing between the chemical species, both enthalpic and entropic are to be considered.

In this chapter the equations for the material flow are derived on the basis of thermodynamic arguments. The different contributions to the system free energy are then analyzed in details.

2.1 Dynamics equation

According to the definition of the free energy G in eq. (2.1), the entropy variation δS for a system in thermal equilibrium depends on the variations in internal energy U, volume V and number of atoms n_i (per unit volume) for each chemical species i:

$$TdS = dU + pdV - \sum_i \mu_i dn_i \tag{2.2}$$

where T is the temperature, p is the pressure and

$$\mu_i = \left.\frac{\delta G}{\delta n_i}\right|_{T,p,n_j} \tag{2.3}$$

is the chemical potential (per atom) for the i-th component.

According to the second law of thermodynamics, all variations in the state of a closed system always imply an increase of the entropy, i.e. $dS > 0$. The measure of the system tendency to restore the equilibrium state upon a given perturbation is defined by the Maxwell derivatives of the entropy functional:

$$\frac{dS}{dU} = \frac{1}{T} \qquad \frac{dS}{dV} = \frac{p}{T} \qquad \frac{dS}{dn_i} = -\frac{\mu_i}{T} \tag{2.4}$$

If a system evolving in time is quite close to the equilibrium conditions, i.e. it can be considered a perturbation of such state, the driving forces leading to the system evolution can be described by the same terms in eq. (2.4), that because of this are also named *thermodynamic potentials*. The thermodynamic driving force leading to the system evolution is then the maximization of the entropy or equivalently the minimization of the free energy G itself.

By considering heteroepitaxial growth by MBE or other low flux and low pressure gas-solid growth techniques, isothermal conditions can be considered thus neglecting any process of heat transfer $dU = 0$. Also the pressure-volume effects are negligible so that the only thermodynamic potentials to be considered are the chemical potentials μ_i. Notice that such conditions permit to consider the system close enough to the equilibrium so that entropy variations are linearly dependent on the chemical potentials. On the contrary, if high growth rates are considered, larger deviations from the equilibrium are expected and the derivation here discussed is no more justified.

2.1.1 Non-conserved dynamics. Attachment/Detachment limited growth

The simplest dynamics possible driving the system to the minimization of free energy simply consists in assuming a redistribution of material directly proportional to the local thermodynamic potentials. Considering only mass transport, for each component i we have:

$$\frac{\partial n_i}{\partial t} = -M_i \frac{\delta G}{\delta n_i} = -M_i \mu_i + \Phi_i, \tag{2.5}$$

where Φ_i an external flux of material and M_i a mobility constant, eventually dependent on temperature. According to eq. (2.5) particles are moved away from regions where $\mu_i > 0$ and accumulates where $\mu_i < 0$, the extent of this process being proportional to the magnitude of μ_i. This results in a reduction of the system free energy since μ_i is by the definition the variation in free energy when adding a particle to the system: where $\mu_i < 0$ the addition of material lowers the energy of the system, while for $\mu_i > 0$ it is by removing

material that the system gains the free energy $-\mu_i$.

It is clear that eq. (2.5) do not imply any conservation of the total mass in the system since the local transfer of material depends only on the local energetics (e.g. in some systems it is possible that all points have $\mu > 0$ and then all of them can loose material). From a physical point of view, this approach can be seen as the limiting case where the motion of material along the surface is infinitely fast and the evolution rates are only determined by the rates of attachment or detachment of material at each location due to the local energetic state. It is also said as evaporation/condensation regime since the interaction with the gas phase can play the same limiting effect.

If the system is closed, from a physical point material conservation must be guarantee, for each component i:

$$\frac{\partial}{\partial t}\int_V n_i(\boldsymbol{x})d\boldsymbol{x} = 0 \tag{2.6}$$

Including this constrain in eq. (2.5) we then obtained a mass conserving evolution equation:

$$\frac{\partial n_i}{\partial t} = -M_i\frac{\delta G}{\delta n_i} + \Phi_i = -M_i\left(\mu_i - \langle\mu_i\rangle\right) + \Phi_i \tag{2.7}$$

where $\langle\mu_i\rangle = \int \mu_i d\boldsymbol{x}/\int d\boldsymbol{x}$ is the average chemical potential coupling all local variations of n_i to ensure the conservation of the overall material. Material redistribution is then given according to the relative stability of each point with respect to the mean: the material is removed from regions where $\mu_i > \langle\mu_i\rangle$ and accumulated where $\mu_i < \langle\mu_i\rangle$.

This process can however occur between points at arbitrary distance so that it is only appropriate to describe systems where diffusion lengths are much larger than the system size.

2.1.2 Conserved dynamics. Diffusion limited growth

According to Onsager linear law [87, 88] the flow $\boldsymbol{J}_i$ of the particle numbers for each i species of the system can be ascribed to local gradients in the thermodynamic potentials:

$$\boldsymbol{J}_i = -\sum_j M_{ij}\nabla\left(\frac{\mu_j}{T}\right) \tag{2.8}$$

where the coefficient M_{ii} is the intrinsic mobility of species i, while M_{ij} is the mobility coefficient for the transfer of species i due to gradients of chemical potential for a different species j. Constant volume and isothermal conditions are assumed in order to exclude particle transport associated to heat transfers or pressure.

If the interactions between atoms of different species can be neglected, each component is expected to diffuse independently of the others, i.e. $M_{ij} = 0$ for $\forall j \neq i$. Eq. (2.8) then reduces to a set of decoupled linear equations:

$$\boldsymbol{J_i} = -M_i\nabla\mu_i \tag{2.9}$$

where ($M_i = M_{ii}/T$). From eq. (2.9) material transfers are defined as consequence of gradients in the corresponding chemical potentials, so that particles move from regions highly unstable to neighbor locations characterized by a lower chemical potential. Since all gradients are defined locally, the extent of material transfer is limited within a proper diffusion length.

Assuming mass conservation, the continuity equation holds

$$\frac{\partial n_i}{\partial t} = -\nabla \cdot \boldsymbol{J_i} + \Phi_i = \nabla \cdot (M_i \nabla \mu_i) + \Phi_i, \tag{2.10}$$

where an external flux Φ_i is included as a source term.

The well known Fick's diffusion equation can be easily derived as a special case of (2.10). Let's consider a closed system with uniform material density n and local solute concentration $c = n_s/n$ with n_s the local number of solute particles. For an ideal binary alloy $\mu = kT \ln c$ (see *Sect. 2.4*) and then, substituting in eq. (2.10)

$$\frac{\partial c}{\partial t} = \nabla \cdot \left(\frac{kTM}{c} \nabla c \right) = D \nabla^2 c \tag{2.11}$$

where the mobility M was assumed proportional to the local composition c: $M = \frac{Dc}{kT}$ and diffusion coefficient D.

2.2 Surface energy

When considering a solid of finite extension, deviations from the bulk properties are expected in correspondence of its free surface. A surface excess free energy density γ [89, 90] must be considered in order to account for the energy cost associated to the formation of the surface with respect to an unlimited bulk system. On the microscopic scale, this energy cost represents the work that must be done to create the surface from the bulk system, i.e. to break the chemical bonds between the atoms of the original bulk system. As γ is defined per unit area of the total surface free energy is given by

$$F_\gamma = \int_S \gamma d\boldsymbol{S} \tag{2.12}$$

where the integral is calculated on the overall free surface S delimiting the solid.

The actual definition of the γ function is rather complex as the energetics of a surface is affected by many different factors. Even for the well studied Si and Ge, the knowledge of γ is only partial [44, 91]. Obviously γ is different for each material and depends on the specific atomic structure of the considered surface. In crystals, different facets corresponds to different arrangement of the atoms and hence to different energy states. γ is then expected to depend on the local orientation of the surface, identified by the normal

direction $\widehat{\boldsymbol{n}}$. Furthermore, γ is expected to change for different surface reconstruction [44] and can be influenced by strain effects [92]. Additional complications finally arise in the case of compounds, such as GaAs [93, 94], according to the distribution of the different atoms, producing facets that can be either neutral or polar. Similarly in the case of alloys surface energy is expected to depend on composition. In the following we will assume that γ is known and consider its only dependence on the surface orientation: $\gamma = \gamma(\widehat{\boldsymbol{n}})$, where $\widehat{\boldsymbol{n}}$ is the outward normal unit vector at the surface.

From the definition of the surface energy in eq. (2.12), an expression of the chemical potential μ_γ can be derived by considering that the addition of an atom to the system is equivalent to a localized variation of the profile, producing a variation of both the area and orientation of the local surface element. For the general case of 3D system [95],

$$\mu_\gamma = \frac{\delta F_\gamma}{\delta n} = V_a \nabla_S \cdot \boldsymbol{\xi} \tag{2.13}$$

where V_a is the atomic volume and $\boldsymbol{\xi}$ is the Cahn-Hoffman vector [96] defined as $\boldsymbol{\xi} = \nabla(r\gamma(\widehat{\boldsymbol{n}}))$ with r the magnitude of the generic position vector $\boldsymbol{r} = r\widehat{\boldsymbol{n}}$ (the subscript S indicates that the derivatives are defined with respect to the surface coordinates).

For a 2D system, where the surface is restricted to a curve C in the plane, eq. (2.13) reduces to the well known Gibbs-Thompson equation:

$$\mu_\gamma = \frac{\delta F_\gamma}{\delta n} = V_a \kappa \left[\gamma + \gamma''(\theta)\right] = V_a \kappa \gamma_s \tag{2.14}$$

κ is the local curvature of the profile, accounting for the variation in its length: $\kappa = \frac{\delta}{\delta n}\int_C d\boldsymbol{l}$. For an explicit curve $z = z(x)$, the line element is simply $d\boldsymbol{l} = dl/cos\theta$ leading to $\kappa = -z''(1+z'^2)^{-3/2}$. The other term in eq.(2.14), $\gamma_s = \gamma + \gamma''(\theta)$ ($\gamma'' = \frac{\partial^2\gamma}{\partial\theta^2}$), is the surface stiffness and accounts for the different stability of facets at different orientation θ (polar angle). The stability of a facet can be inspected by considering the variation in surface energy when changing the facet orientation by a small angle θ. Expanding the energy to second order in θ, with respect to the initial orientation $\theta = 0$ we obtain:

$$\begin{aligned} F_\gamma = \int_C \gamma(\theta) d\boldsymbol{l} \approx \gamma(0)l + \int_C \left.\frac{d\gamma}{d\theta}\right|_{\theta=0} \theta dl + \int_C \left[\gamma(\theta) + \left.\frac{\partial^2\gamma}{\partial\theta^2}\right|_{\theta=0}\right]\theta^2 dl = \\ = F_\gamma(0) + \int_C \gamma_s \theta^2 dl \end{aligned} \tag{2.15}$$

The zeroth-order term is the energy of the unperturbed facet $F_\gamma(0)$ and the first order term vanishes because of symmetry reasons. The variation of the surface energy is then defined by the last term and its direction is given by the sign of γ_s: for $\gamma_s > 0$ the initial facet orientation is stable while for $\gamma_s < 0$ it is unstable as the energy can be reduced by any perturbation leading to a more favorable orientation. In the former case, the crystal can expose the given facet while in the latter the profile will change in order to expose

other more favorable orientations.

For the simplest case of isotropic $\gamma = \gamma_0$, i.e. surface energy independent of the profile orientation, variations of chemical potential along the surface are exclusively determined by the local curvature:

$$\mu_\gamma = V_a \gamma_0 \kappa \tag{2.16}$$

This is evident from eq. (2.14) and is valid also for 3D surfaces, by considering the mean-curvature $\kappa = -1/2\nabla \cdot \widehat{\boldsymbol{n}}$. The dynamics described by using the isotropic chemical potential of eq. (2.16) in eq. (2.5) or (2.10) is the well known mean-curvature flow [3, 5, 97].

2.2.1 Equilibrium crystal shape and Wulff plot

For a finite crystal limited by a surface S, the equilibrium crystal shape (ECS) is defined as the profile for S such to minimize the surface energy, i.e. the integral function in eq. (2.12). For isotropic γ, the minimization of the surface energy simply corresponds to the minimization of the exposed surface area, so the ECS is exactly a sphere (i.e. a circle in 2D). When γ is anisotropic, some orientations are preferred as they correspond to minima in γ, but others can be unfavored (high value of γ) or even unstable (in 2D if $\gamma_s < 0$). The ECS then results from the relative stability of all facets.

A simple geometrical procedure called *Wulff construction* [90, 98], can be used in order to define the ECS for a given function $\gamma = \gamma(\widehat{\boldsymbol{n}})$. To simplify the description of this technique, lets consider the simple 2D case and a commonly used anisotropy function, consisting of a sinusoidal deviation from the constant isotropic value γ_0:

$$\gamma(\theta) = \gamma_0[1 - \alpha \cos(N\theta)] \tag{2.17}$$

where N minima are present at angles $\theta_i = \frac{2\pi}{N} i$ for $i = 0, \dots, N-1$ and α represents the degree of anisotropy, ranging from 0 to 1, accounting for the difference in surface energy between maxima and minima in γ. *Fig. 2.1* sketches the procedure for the Wulff construction for the case of $\gamma_0 = 1$, $\alpha = 0.2$ and $N = 4$. First of all, the polar plot of $\gamma(\theta)$ is traced (red curve). Then at each point on the curve, a straight line is drawn along the direction perpendicular to the vector $(\theta, \gamma(\theta))$, joining the point on the curve to the origin, as indicated in the figure. The ECS is defined by the inner envelope of all these lines, as resulting in *Fig. 2.1* b). Notice that each element of the profile is defined by a small segment on the lines used in the construction. However, not all of such directions contribute to the final shape. All dashed lines in *Fig. 2.1* are external to the ECS region and corresponds to missing orientations in the final profile. More precisely, such directions are the unstable orientations defined by $\gamma_s < 0$ and are localized in the region where γ assume its maximum values. As this directions are left out of the ECS, sharp angles are formed between the closest values of θ such that $\gamma_s = 0$.

The existence and extension of this corners depends on the actual definition of $\gamma(\theta)$,

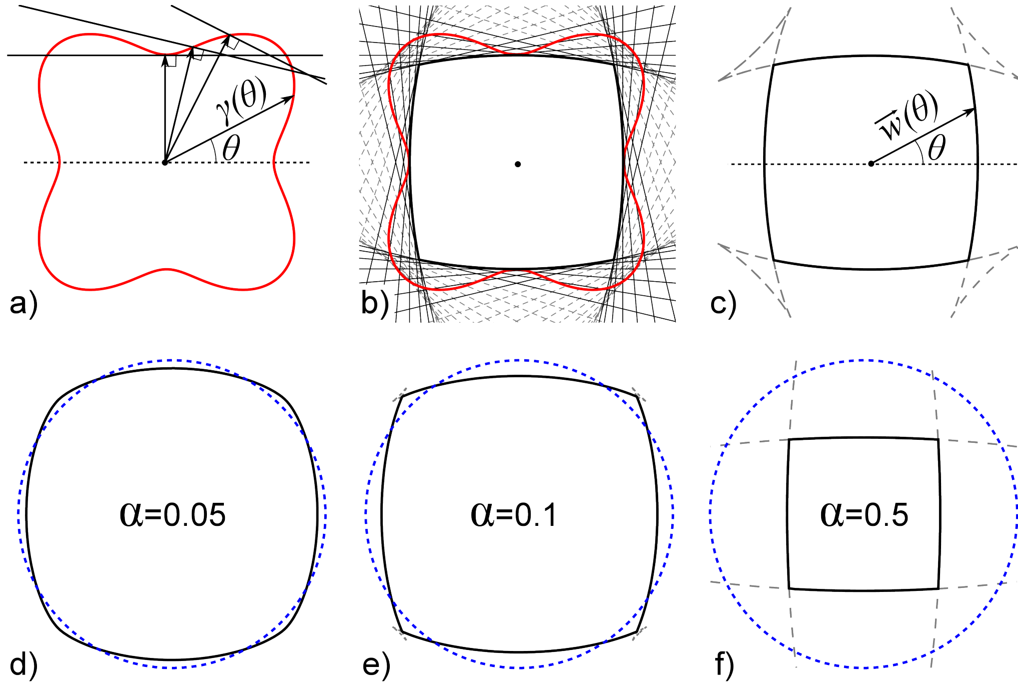

Figure 2.1: a) Schematics of the Wulff construction procedure for a function $\gamma = 1 - 0.2\cos(4\theta)$. b) Equilibrium Crystal Shape obtained from Wulff construction (construction lines corresponding to missing orientations are shown with dashes). c) Parametric solution of the ECS as for the same function in a), on the basis of eq. (2.18). d-e) ECS calculated for different anisotropy degree α. The isotropic circular shape is shown (blue dotted line) for comparison.

for the present case on the parameter α. In particular, a critical value of $\alpha = 1/(n^2 - 1)$ can be defined from the condition of $\gamma_s = 0$. If $\alpha < \alpha_c$ no missing orientations exist as $\gamma_s > 0$ for all angles θ (weak anisotropy); on the contrary, for $\alpha > \alpha_c$ some directions become unstable thus leading to sharp corners (strong anisotropy). In particular, as indicated in *Fig. 2.1* d-e), the larger is α the more faceted looks the profile as the range of unstable directions is more extended. The ECS then changes from the isotropic circular shape ($\alpha = 0$) to a squared shape for ($\alpha \to 1$).

As the equilibrium state is characterized by a constant chemical potential μ_{eq}, in 2D the ECS can be defined analytically by solving in parametric form the Gibbs-Thompson equation (2.14) for $\mu_\gamma = \mu_{\text{eq}}$.

$$x(\theta) = \frac{V_a}{\mu_{\text{eq}}}(\gamma\cos\theta - \gamma'(\theta)\sin\theta), \qquad y(\theta) = \frac{V_a}{\mu_{\text{eq}}}(\gamma\sin\theta + \gamma'(\theta)\cos\theta). \tag{2.18}$$

In *Fig. 2.1* c), the parametric function $w(x(\theta), y(\theta))$ is reported for the same function γ used for the Wulff construction, showing the same ECS with unphysical "ears" (dashed) determined by the missing orientations.

The procedure of the Wulff construction can be straightforwardly extended to 3D systems by considering the plot in spherical coordinates (θ, φ) and replacing the perpendicular lines with planes in order to define a 3D envelope leading to the ECS. Also in this

case, for strong anisotropy, some orientations can be unstable and excluded from the final ECS [99].

2.2.2 Corner regularization

The presence of corners in the ECS, determined by strong anisotropy, is in general an undesired feature when considering the evolution of the surface as it leads to an unstable behavior for all missing orientations. More precisely, the dynamics obtained by using the anisotropic chemical potentials μ_γ (eq. (2.13) or (2.14)) in eq. (2.5) or eq. (2.10) is an ill-posed problem for all missing orientations, leading to numerical instability. In the case of strong anisotropy, an appropriate procedure of profile regularization is needed in order to make the system properly tractable.

A possible solution consists in redefining the functional form of $\gamma(\theta)$ in such a way that the stiffness is always positive but the same ECS is obtained. In particular, this solution, named *Frank's convexification* [29], is obtained in 2D by imposing that the stiffness $\tilde{\gamma}_s$ associated to the regularized energy density $\tilde{\gamma}$ satisfies

$$\tilde{\gamma}_s := \max(0, \gamma_s) \qquad \forall\theta \tag{2.19}$$

The resulting regularized $\tilde{\gamma}$ function admits all possible orientations so that no sharp corner is formed. At the same time the Wulff plot associated to $\tilde{\gamma}$ looks exactly the same of that for the original unstable γ function. This is possible since all missing orientations in the original ECS are restored in the regularized $\tilde{\gamma}$ function as segments of vanishingly small extension in the original corner region.

An alternative solution preserving the original γ function consists in introducing an additional term in γ such to suppress the formation of sharp corners [100]:

$$\tilde{\gamma} = \gamma + \beta\kappa^2, \tag{2.20}$$

where β is a "corner energy" and the curvature term tends to diverge as the surface gets too sharp. This way, an additional term enters in the chemical potential definition, balancing the instability of the excluded facets. The result is that such orientations are no more unstable and can form in the region where the corner was observed leading to a locally rounded profile. The extension of the rounding region can be tuned according to the value of β.

2.3 Elastic energy

Elastic effects in heteroepitaxial systems typically arise because of the lattice mismatch between the components. In the following, we shortly define the main concepts of the linear elasticity theory that will be part of our models. A more exhaustive description is

left to textbooks [101].

Let's consider a solid as a continuous medium. In equilibrium, a generic point in the solid can be individuated with respect to a reference coordinate system by means of the position vector $\boldsymbol{r_0}$. If $\boldsymbol{r}$ is the position of the same point after a deformation of the solid, the displacement vector can be defined as:

$$\boldsymbol{u} = \boldsymbol{r} - \boldsymbol{r_0} \tag{2.21}$$

Displacements result not only because of deformations but also in consequence of rotations. In the limit of infinitesimal displacements, all possible deformations can be defined by the symmetric part of the Jacobian matrix of the displacement field $\boldsymbol{J} = \frac{\partial \boldsymbol{u}}{\partial \boldsymbol{x}}$ thus allowing to define the strain tensor as

$$\boldsymbol{\varepsilon} = \frac{1}{2}\left[\nabla \otimes \boldsymbol{u} + \boldsymbol{u} \otimes \nabla\right] \qquad \Longleftrightarrow \qquad \varepsilon_{ij} = \frac{1}{2}\left(\frac{\partial u_i}{\partial x_j} + \frac{\partial u_j}{\partial x_i}\right) \tag{2.22}$$

$\varepsilon_{ij} = \varepsilon_{ji}$ because of symmetry.

The deformation of the solid is the result, on a microscopic scale, of the displacement of atoms with respect to their equilibrium positions and hence implies the distortion and stretching of inter-atomic bonds. As a consequence, internal forces arise tending to return the system to the original equilibrium state. Such volume forces can be defined as

$$\boldsymbol{F} = \frac{\partial \boldsymbol{\sigma}}{\partial \boldsymbol{x}} \qquad \Longleftrightarrow \qquad F_i = \frac{\partial \sigma_{ij}}{\partial x_j} \tag{2.23}$$

where the second order tensor $\boldsymbol{\sigma}$, symmetric by definition, is the stress tensor. In particular, σ_{ij} represents the force component F_i acting on a unit area perpendicular to the x_j axis.

In classical linear elasticity theory, stress and strain are related by a fourth order tensor $\boldsymbol{C}$, named *stiffness tensor*, leading to the generalized Hooke's Law:

$$\boldsymbol{\sigma} = \boldsymbol{C} : \boldsymbol{\varepsilon} \qquad \Longleftrightarrow \qquad \sigma_{ij} = \sum_{k,l} C_{ijkl}\varepsilon_{kl} \tag{2.24}$$

Tensor $\boldsymbol{C}$ is symmetric by definition and the actual number of its independent components is reduced according to the crystal symmetry. In particular for cubic symmetry, typical of semiconductors such as Si and Ge, $\boldsymbol{C}$ is fully defined by 3 constants only:

$$C_{1111} = C_{2222} = C_{3333} \equiv C_{11} \tag{2.25a}$$

$$C_{1122} = C_{1133} = C_{2233} \equiv C_{12} \tag{2.25b}$$

$$C_{1212} = C_{1313} = C_{2323} \equiv C_{44} \tag{2.25c}$$

Finally, the highest symmetry is obtained for an isotropic material, with no preferential directions. The elastic properties of such a system can be defined from the cubic crystal by

imposing the additional constrain:

$$C_{11} = C_{12} + 2C_{44} \tag{2.26}$$

Therefore, only 2 elastic constants fully characterize the elastic response of an isotropic solid, namely the shear modulus μand the Lamé modulus λ:

$$\lambda \equiv C_{12} \qquad \mu \equiv C_{44} \tag{2.27}$$

Alternatively, the Young modulus $Y = \mu\frac{3\lambda+2\mu}{\lambda+\mu}$ and Poisson Ratio $\nu = \frac{\lambda}{2(\lambda+\mu)}$ are commonly used. In full-index notation the components of the strain tensor $\boldsymbol{C}$ of an isotropic material are defined by

$$C_{ijkl} = \lambda\delta_{ij}\delta_{kl} + \mu(\delta_{ik}\delta_{jl} + \delta_{il}\delta_{jk}) \tag{2.28}$$

The stress-strain relation can then be written as

$$\sigma_{ij} = \lambda\delta_{ij}\sum_k \varepsilon_{kk} + 2\mu\varepsilon_{ij} \tag{2.29}$$

As a deformed state implies a distortion of the microscopic structure of the solid, an elastic energy is associated:

$$F_\varepsilon = \int_V \rho_\varepsilon d\boldsymbol{x} \tag{2.30a}$$

$$\rho_\varepsilon = \frac{1}{2}\boldsymbol{\varepsilon} : \boldsymbol{C} : \boldsymbol{\varepsilon} = \frac{1}{2}\sum_{ijkl} C_{ijkl}\varepsilon_{ij}\varepsilon_{kl} \tag{2.30b}$$

where ρ_ε is the elastic energy density, satisfying $\sigma_{ij} = \frac{\partial\rho_\varepsilon}{\partial\varepsilon_{ij}}$. In the case of isotropic solid, the elastic energy density is obtained substituting eq. (2.28) in (2.30b):

$$\rho_\varepsilon = \mu\sum_i \varepsilon_{ii}^2 + 2\mu\sum_{ij}^{i<j} \varepsilon_{ij}^2 + \frac{1}{2}\lambda\left(\sum_i \varepsilon_{ii}\right)^2 \tag{2.31}$$

For an homogeneous system, the chemical potential due to elastic energy is the variation of eq. (2.30) upon addition of an atom (volume V_a):

$$\mu_\varepsilon = \frac{\delta F_\varepsilon}{\delta n} = V_a\rho_\varepsilon \tag{2.32}$$

2.3.1 Inhomogeneous system

So far, displacements have been defined in an absolute sense, with respect to the equilibrium state. In many interesting cases, however, the reference state for the displacement definition do not correspond to a stress free-state so that the system deformation is more

properly defined as the response of the system to the initial state. For example, if a volume of material is forced to adapt to the different geometry of an host, i.e. a surrounding solid matrix for an inclusion [102] or the substrate for a film grown epitaxially, a permanent deformation state has to be considered. In fact, if it were possible to remove such a region again, it would undergo a deformation in the opposite direction up to restore its zero-stress equilibrium state. This deformation corresponds to the eigenstrain of the reference state. In particular, it is possible to define the eigenstrain $\boldsymbol{\varepsilon}^{\star}$ for a certain region of the system as the strain $\boldsymbol{\varepsilon}$ that the system should assume in order to recover the zero-stress condition. If the stress is defined as

$$\boldsymbol{\sigma} = \boldsymbol{C}\left(\boldsymbol{\varepsilon} - \boldsymbol{\varepsilon}^{\star}\right), \tag{2.33}$$

the eigenstrain is then defined by

$$\boldsymbol{\sigma} = 0 \qquad \Longrightarrow \qquad \boldsymbol{\varepsilon}^{\star} = \boldsymbol{\varepsilon} \tag{2.34}$$

The stress associated to the reference state, with no strain $\boldsymbol{\varepsilon}$, is then determined by the eigenstrain and is called eigenstress:

$$\boldsymbol{\sigma}^{\star} = \boldsymbol{C} : \boldsymbol{\varepsilon}^{\star} \tag{2.35}$$

According to the previous definitions, the actual strain $\boldsymbol{\varepsilon}$ accounts only for the response of the system with respect to the reference geometry while the total strain, properly defined with respect to the absolute equilibrium state, can be determined by $\boldsymbol{\varepsilon} - \boldsymbol{\varepsilon}^{\star}$, as the strain resulting from both the strain response and the eigenstrain. It follows that all previous relations, derived for the total strain can be properly applied also for a system with eigenstrain by simply replacing $\boldsymbol{\varepsilon}$ with $\boldsymbol{\varepsilon} - \boldsymbol{\varepsilon}^{\star}$ in all terms. In particular, the elastic energy density then becomes

$$\rho_{\varepsilon} = \frac{1}{2}(\boldsymbol{\varepsilon} - \boldsymbol{\varepsilon}^{\star}) : \boldsymbol{C} : (\boldsymbol{\varepsilon} - \boldsymbol{\varepsilon}^{\star}) \tag{2.36}$$

The formalism of eigenstrain becomes essential in order to characterize the elastic state of an inhomogeneous system. This is the case, in particular, of heteroepitaxial systems, as the lattice mismatch depends on the alloy composition and hence can vary from a region to the other if the system composition is not uniform, as it usually happens in the growth of films and islands. Consequently a local eigenstrain is determined by the permanent deformed state of the material, forced to the lattice parameter of the growth substrate. In the linear approximation of Vegard Law, the variation of the lattice parameter with the local composition is simply defined by interpolating between the values of the pure components. For a generic alloy A_cB_{1-c}

$$a(c) = ca_A + (1-c)a_B \tag{2.37}$$

With this assumption, the eigenstrain of a region at composition c forced to the lattice parameter of the substrate, at composition c_0, is given by

$$\boldsymbol{\varepsilon}^\star(c) = \varepsilon_0(c_0 - c)\boldsymbol{I} \qquad \Longleftrightarrow \qquad \varepsilon^\star_{ij} = \varepsilon_0(c_0 - c)\delta_{ij} \tag{2.38}$$

where ε_0 is the lattice mismatch of the AB system: $\varepsilon_0 = \frac{a_B - a_A}{a_B}$ and $\boldsymbol{I}$ the identity matrix. An inhomogeneous eigenstrain condition $\varepsilon^\star(\boldsymbol{x})$ is then defined throughout the system because of the composition profile $c = c(\boldsymbol{x})$. The elastic energy density, dependent on the local eigenstrain as in eq. (2.36), will then depend explicitly on the local composition. In particular, for the isotropic case:

$$\begin{aligned}\rho_\varepsilon(c) &= \mu \sum_i \left[\varepsilon_{ii} - \varepsilon^\star(c)\right]^2 + 2\mu \sum_{ij}^{i<j} \varepsilon_{ij}^2 + \frac{1}{2}\lambda \left[\sum_i (\varepsilon_{ii} - \varepsilon^\star(c))\right]^2 = \\ &= \mu \sum_i \left[\varepsilon_{ii} - \varepsilon_0(c_0 - c)\right]^2 + 2\mu \sum_{ij}^{i<j} \varepsilon_{ij}^2 + \frac{1}{2}\lambda \left[\sum_i [\varepsilon_{ii} - \varepsilon_0(c_0 - c)]\right]^2\end{aligned} \tag{2.39}$$

Correspondingly, the local chemical potential for an inhomogeneous system will include, in addition to eq. (2.32), a contribution due to the variation in composition. For the species i:

$$\mu_{\varepsilon,i} = \frac{\delta F_\varepsilon}{\delta n_i} = \frac{\delta F_\varepsilon}{\delta n}\frac{\delta n}{\delta n_i} + \frac{\delta F_\varepsilon}{\delta c}\frac{\delta c_i}{\delta n_i} = V_a \left[\rho_\varepsilon + (1 - c_i)\frac{\delta \rho_\varepsilon}{\delta c_i}\right] \tag{2.40}$$

where the composition is given in atomic fraction $c_i = n_i/n$ (with n_i the density of atoms of species i and $n = \sum_i n_i$).

2.3.2 Mechanical equilibrium

In mechanical equilibrium a system do not exert any net force. If $\boldsymbol{f}$ is the local force distribution in the volume V and $\boldsymbol{P} = \boldsymbol{\sigma} \cdot \widehat{\boldsymbol{n}}$ is the local force along its surface S, the equilibrium is achieved by:

$$\int_V \boldsymbol{f} dV + \int_S \boldsymbol{P} dS = \int_\Omega (\boldsymbol{f} + \nabla \cdot \boldsymbol{\sigma})\, dV = 0 \tag{2.41}$$

where the surface integral has been rewritten by means of Gauss theorem. The equilibrium condition thus locally requires that

$$-\nabla \cdot \boldsymbol{\sigma} = \boldsymbol{f} \tag{2.42}$$

For the case of interest of the growth at the surface of a crystal, we assume that no volume forces are present and that the solid is in the vacuum, i.e. the vapor surrounding the solid do not exert any force on the film. Surface stress is also assumed to be zero. The

elastic problem for the state of equilibrium is then

$$\begin{cases} \nabla \cdot \boldsymbol{\sigma} = 0 & \text{on } V \\ \boldsymbol{\sigma} \cdot \widehat{\boldsymbol{n}} = 0 & \text{on } S_N \\ \boldsymbol{u} = 0 & \text{on } S_D \end{cases} \tag{2.43}$$

where the boundary conditions on $S = S_N \cup S_D$ are distinguished for the free surfaces S_N, where no-flux Neumann boundary conditions apply, and the boundary S_D with the bulk far below the surface, where the material is assumed to be fixed and Dirichlet boundary conditions are set.

For an isotropic system with uniform eigenstrain $\varepsilon^{\star}_{ij} = \varepsilon_0 \delta_{ij}$, e.g. a film subject to a uniform misfit strain ε_0, the equilibrium condition in (2.43) can be simplified according to eq. (2.29), leading to the Navier-Cauchy equation:

$$\mu \nabla^2 \boldsymbol{u} + (\lambda + \mu) \nabla \left[\nabla \cdot \boldsymbol{u} \right] = 0 \tag{2.44}$$

However, in many cases, e.g. a film with a composition profile or a typical Stranski-Krastanow island, both the elastic constants, µand λ, and the eigenstrain $\varepsilon^{\star}$ (eq. (2.38)) can vary from one point to the other, for example according to the local composition. In this case, the equilibrium equation is more complex:

$$\nabla \cdot \left[\mu \left(\nabla \otimes \boldsymbol{u} + \boldsymbol{u} \otimes \nabla \right) \right] + \nabla \left[\lambda \nabla \cdot \boldsymbol{u} \right] = \nabla \left[(2\mu + 3\lambda) \, \varepsilon^{\star} \right] \tag{2.45}$$

Evidently, eq. (2.45) reduces to eq. (2.44) when µ, λ and $\varepsilon^{\star}$ are constant throughout the overall system.

2.3.3 Flat-Island Approximation

Let's consider a flat film of infinite extension in the xy-plane and limited by a free surface along the z direction, subject to the local eigenstrain $\varepsilon^{\star} = \varepsilon_0 (c_0 - c) \delta_{ij}$, as in eq. (2.38). Because of the planar symmetry, the strain tensor is diagonal. Since the film is free to relax only along the z direction, normal to the surface, the only non-zero component of the strain tensor is ε_{zz}. In this simple case, the condition of mechanical equilibrium simply reduces to the boundary condition at the free surface:

$$\sigma_{zz} = (\lambda + 2\mu)(\varepsilon_{zz} - \varepsilon^{\star}) + \lambda(\varepsilon_{xx} + \varepsilon_{yy} - 2\varepsilon^{\star}) = 0 \tag{2.46}$$

where eq. (2.29) was used. The strain component ε_{zz} is then defined by the in-plane deformations:

$$\varepsilon_{zz} = \varepsilon^{\star} - \frac{\lambda}{\lambda + 2\mu}(\varepsilon_{xx} + \varepsilon_{yy} - 2\varepsilon^{\star}) = \frac{2\nu}{1 - \nu}\varepsilon^{\star} \tag{2.47}$$

where no relaxation in the xy-plane was allowed ($\varepsilon_{xx} = 0$ and $\varepsilon_{yy} = 0$).

According to the linear elastic theory [101], if a point force $\boldsymbol{F}$ is applied at a point $\boldsymbol{x}' = (x', y', 0)$ on the film surface, the response of the system, corresponding to the displacement field $\boldsymbol{u}(\boldsymbol{x})$, is given by a simple linear relation:

$$\boldsymbol{u}(\boldsymbol{x}) = \boldsymbol{G}(\boldsymbol{x} - \boldsymbol{x}')\boldsymbol{F}(\boldsymbol{x}') \qquad \Longleftrightarrow \qquad u_i(\boldsymbol{x}) = G_{ij}(\boldsymbol{x} - \boldsymbol{x}')F_j(\boldsymbol{x}'), \tag{2.48}$$

where $\boldsymbol{G}$ is the Green's function for the elastic problem in a semi-infinite domain (see Ref. [101]). If considering a distribution $\boldsymbol{P}(\boldsymbol{x})$ of forces along the surface ($\boldsymbol{P}(\boldsymbol{x}) = \boldsymbol{F}\delta(\boldsymbol{x})$ for a point force), the resulting displacement field $\boldsymbol{u}(\boldsymbol{x})$ is given by the convolution integral:

$$\boldsymbol{u}(\boldsymbol{x}) = (\boldsymbol{G} * \boldsymbol{P})(\boldsymbol{x}) = \int \boldsymbol{G}(\boldsymbol{x} - \boldsymbol{x}')\boldsymbol{P}(\boldsymbol{x}')d\boldsymbol{x}' \tag{2.49}$$

Eq. (2.49) is strictly correct only for a perfectly flat profile. However, it permits to calculate an approximate solution of the elastic problem for generic shallow profiles, i.e. flat-islands, accounting for deviations from the planar system by means of a suitable distribution of surface forces [103, 104]. In particular, it can be demonstrated that the elastic relaxation induced by a small perturbation of the profile along the x direction is equivalent to the response of the flat film to a distribution of surface "stressors" Σ, defined by:

$$\Sigma(x) = \int_{-\infty}^{h(x)} \sigma^f_{xx}(x, z)dz \tag{2.50a}$$

$$\sigma^f_{xx} = -\frac{Y}{1-\nu}\varepsilon^\star = -\frac{Y}{1-\nu}\varepsilon_0\left[c_0 - c(x, z)\right] \tag{2.50b}$$

where the integration is along the column of material above the substrate at each point x and σ^f_{xx} is the xx component of the stress for a tetragonally distorted film, calculated according to eq. (2.29) for $\varepsilon_{xx} = \varepsilon_{yy} = 0$, ε_{zz} as given in eq. (2.47) and eigenstrain defined in eq. (2.38).

Thus following the "flat-island" approximation, displacements occur only along the x direction, i.e. $\boldsymbol{u} = u(x)\widehat{\boldsymbol{x}}$, and $\boldsymbol{P} = P(x)\widehat{\boldsymbol{x}}$. The solution of the elastic problem at the surface ($z = 0$) is then be obtained from eq. (2.49) as:

$$u(x) = \iint G_{xx}(x - x', y', 0)P(x')dx'dy' = \int \tilde{G}(x - x')P(x')dx' \tag{2.51}$$

where $\tilde{G}(x) = \int G_{xx}(x, y, 0)dy$. By setting $P(x) = \frac{d\Sigma}{dx}$, the strain can be calculated from

eq. (2.51) :

$$\varepsilon_{xx}(x) = \frac{d}{dx}\left[\int \tilde{G}(x-x')\frac{d}{dx'}\Sigma(x')dx'\right] =$$
$$= \frac{d}{dx}\left[\tilde{G}(x-x')\sigma_{xx}(x')\right]_{x'\to-\infty}^{x'\to+\infty} - \int \frac{d}{dx}\frac{d}{dx'}\tilde{G}(x-x')\Sigma(x')dx' =$$
$$= \int g(x-x')\Sigma(x')dx' = (g*\Sigma)(x) \tag{2.52}$$

where an integration by parts was performed and the first term of the integration was set to zero since the effect of a "stressor" at infinite distance tends to zero.

The function g is the Green function for the strain response to the "stressor" distribution:

$$g = \frac{d^2\tilde{G}}{dx^2} = \frac{d^2}{dx^2}\int G_{xx}(x,y,0)dy = \frac{2(1+\nu)}{\pi Y}\frac{1}{x^2} \approx \frac{2(1+\nu)}{\pi Y}\frac{1}{x^2+b^2} \tag{2.53}$$

and is approximated by a lorentzian function with cutoff b in order to avoid the divergence at $x \to 0$ for the integral in eq. (2.52). From a technical point of view, the convolution product in eq. (2.52) can be conveniently evaluated in the Fourier as it reduces to the product between the Fourier transforms:

$$\hat{\varepsilon}_{xx}(q) = \hat{g}(q)\hat{\Sigma}_s(q) = \frac{2(1-\nu^2)}{Y}\frac{e^{-b|q|}-1}{b}\hat{\Sigma}_s(q) \tag{2.54}$$

where $q = \frac{2\pi}{L}n$. The strain profile ε_{xx} in the real space can then be obtained by calculating the inverse Fourier Transform. For a discretized representation of the unknown surface profile, as given in the growth simulations, the procedure above can be efficiently performed by means of the Fast Fourier Transform algorithm [105].

The approach here discussed offers an effective shortcut for the estimation of the elastic field for structures with shallow morphology. In Fig. 2.2 a comparison between the "real" strain profile obtained by solving the full elastic problem of eq. (2.43) and the prediction of the flat island approximation for a test case consisting of a nearly flat triangular island (actually a ripple since the y direction is infinite) of Ge on a flat Si substrate. Very good agreement between the curves is achieved. This holds for a generic profile provided that a shallow morphology is considered while increasing the profile steepness, larger deviations are found thus demanding for further complications [104].

Once ε_{xx} is known, according to eq. (2.47), it is possible to define the strain component normal to the surface:

$$\varepsilon_{zz} = \frac{2\nu}{1-\nu}\varepsilon^{\star} - \frac{\nu}{1-\nu}\varepsilon_{xx}(x) = \varepsilon_{zz}^{\text{flat}} - \frac{\nu}{1-\nu}\varepsilon_{xx}(x) \tag{2.55}$$

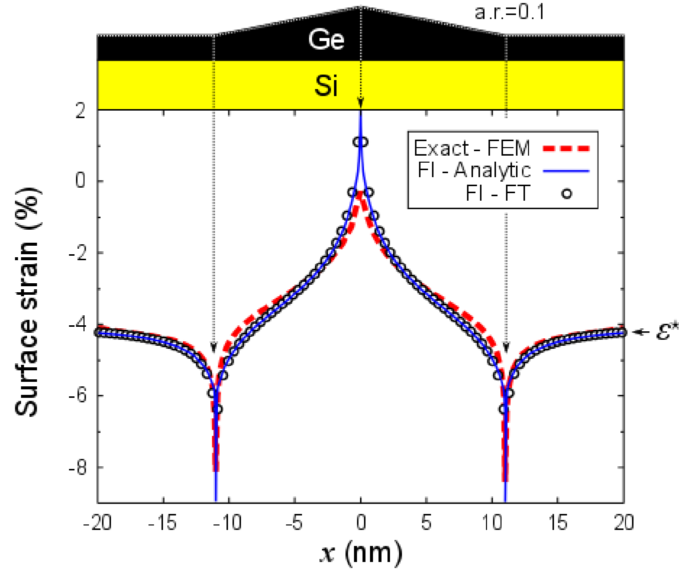

Figure 2.2: Total elastic strain ($\epsilon_{xx} - \epsilon^\star$ component) along the surface profile for a simple Ge island (height vs. base a.r.=0.1) on top of a Si substrate, sketched above (system is infinite in the y direction). In the graph it is shown a comparison between the "real" strain profile calculated solving eq. (2.43) by Finite Element Method (FEM) and the flat-island (FI) approximated solution, calculated both analytically (possible for the very simple geometry considered) and with the Fourier Transform approach discussed in the text.

and hence calculate the local free energy density from eq. (2.40)

$$\rho_\varepsilon(x) = \frac{Y}{2(1+\nu)}\left[(\varepsilon_{xx}(x) - \varepsilon^\star)^2 + \varepsilon^{\star 2} + \frac{1}{(1-\nu)^2}\left[(1+\nu)\varepsilon^\star + \varepsilon_{xx}(x)\right]^2\right] \tag{2.56}$$

2.3.4 Asaro-Tiller-Grinfeld instability

The role of the elastic contribution in the island formation for Stranski-Krastanow system can be inspected by a simple linear stability analysis of the initially flat film [106, 107] Let's consider a small sinusoidal perturbation of the film height h:

$$h(x) = a\cos(qx) \tag{2.57}$$

where a and q are the amplitude and wave vector of the perturbation.

The total stress distribution into the film, as a function of the distance d from the surface, is given by [108]

$$\begin{cases} \sigma_{xx} &= \sigma^\star - \sigma^\star\left(q^2 d - 2q\right)e^{-qd}a\cos(qx) \\ \sigma_{zz} &= -\sigma^\star q^2 d e^{-qd} a\cos(qx) \\ \sigma_{xz} &= -\sigma^\star q\left(1 - qd\right)e^{-qd}a\sin(qx) \end{cases} \tag{2.58}$$

Here the system is considered purely 2D but results are easily extensible for the case of

infinite extension along the y direction just including a fixed stress component $\sigma_{yy} = \sigma^\star$.

The system free energy includes a surface energy contribution, given in eq. (2.12), and the elastic energy due to the misfit strain between the film and the substrate underneath[106]:

$$\rho_\varepsilon \approx \frac{2\sigma^{\star 2}}{Y} qa \cos(qx) \tag{2.59}$$

The local chemical potential is the sum of the two contributions derived from the free energy definitions (eqs. (2.16) and (2.32)):

$$\mu_\gamma = V_a \kappa \gamma + V_a \rho_\varepsilon = V_a \left[\gamma q^2 a \cos(qx) + U_\varepsilon qa \cos(qx) \right] \tag{2.60}$$

where we used the definition $\kappa \approx -\frac{d^2h}{dx^2}$ in a small slope limit and $U_\varepsilon = 2\sigma^{\star 2}/Y$.

In the case of diffusion limited growth, in a small slope limit, the variation of the profile with time directly follow from eq. (2.10):

$$\frac{\partial h}{\partial t} = M \nabla^2 \mu = M \left(-\gamma q^4 + U_\varepsilon q^3 \right) a \cos(qx), \tag{2.61}$$

where M is a constant mobility. The evolution is then given by the variation in the amplitude $a = a(t)$, i.e. $h(t) = a(t) \cos(qx)$, where

$$a(t) = a(0) \exp\left[-M \left(\gamma q^4 - U_\varepsilon q^3 \right) t \right] = a(0) \exp\left[-M \gamma q^3 (q - q_c) t \right], \tag{2.62}$$

with $q_c = U_\varepsilon/\gamma$. The dependence on q of the amplification factor of the perturbation, given by the argument of the exponential term, is shown in Fig. 2.3 for different values of misfit, i.e. different compositions of the film. For values $q > q_c$ the amplitude decays to zero and the flat surface is stable; on the contrary, when $q < q_c$ the perturbation amplitude grows exponentially thus leading to a surface instability. In particular, the fastest growing instability is obtained for $q = 3/4 q_c$.

The same arguments can be applied as well in the case of attachment/detachment limited growth. Substituting eq. (2.60) in eq. (2.5) and integrating with respect to the profile amplitude one obtain

$$a(t) = a(0) \exp\left[-M \gamma q (q - q_c) t \right] \tag{2.63}$$

Again the flat system becomes unstable for values of $q < q_c$ leading to an exponential growth of the profile amplitude. In this case, the fastest growing instability is for $q = 1/2 q_c$. The amplification factor is shown by the dashed line in Fig. 2.3.

For a generic perturbation the very same arguments holds for each Fourier component leading to the coexistence of multiple unstable q modes.

Note that the equations here discussed are valid in the limit of small slopes and hence for the initial triggering of the instability. At later stages, a more appropriate calculation of

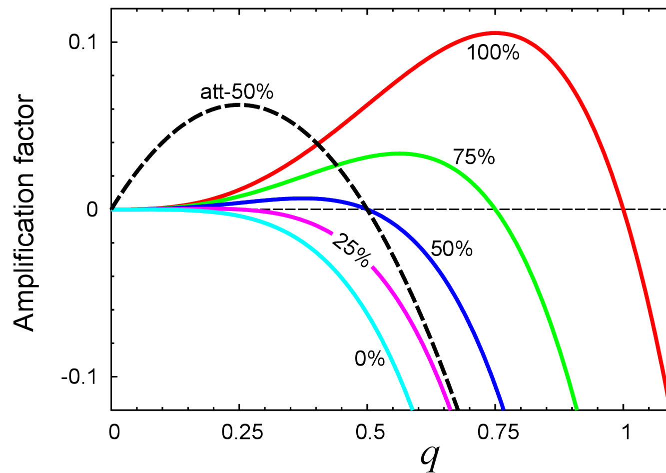

Figure 2.3: Plot of the amplification factor for the perturbation amplitude (argument of the exponential function) as a function of its wave vector q (in U_ε/γ unit). Solid lines are obtained for the case of diffusion limited dynamics and each one refers to a different composition of the film, i.e. a different misfit strain $\sigma^\star = c\sigma_0$ (σ_0 is the stress due to the mismatch of the two components). The dashed line shows the amplification factor calculated for the case of attachment/detachment limited growth and composition 50%.

the elastic contribution should be considered. During the derivation the surface energy was assumed isotropic, otherwise the surface stiffness had to be considered. In such a case the stability condition and the velocity of the perturbation would depend on the surface orientation and hence vary during the growth process [10]. Furthermore, the thickness of the film was assumed infinite to avoid interactions with the substrate and no deposition flux was included to account for the growth. For typical heteroepitaxial systems, it is however known that γ varies with the film thickness h, decreasing during the growth: $\gamma \sim \gamma_\infty [1 + \alpha \exp(-\beta h)]$ (γ_∞ is the value for infinite thickness and α, β are system parameters [10, 45, 109]) . The lowering of γ during the growth leads to an increase of q_c and hence extends the instability to shorter wavelengths, eventually included in the finite size of the system.

Finally, in this discussion a uniform stress $\sigma^\star$ was assumed. In particular, this implies that the composition of the film, determining the local misfit strain, is the same at all points. A more realistic description of the growth should however account for the composition profile from the substrate to the film, eventually changing during the deposition [23, 24, 110, 111]. This effect is included in the model discussed in *Ch. 3* and imply a more complicated behavior of the instability due to the variation of the rates for each q component of the perturbation as the composition varies. In particular, as shown in Fig. 2.3, the larger is the difference in composition between film and substrate (i.e. the misfit strain), the larger is the range of q leading to the instability ($q_c \sim c_{\text{film}} - c_{\text{sub}}$) so that the wavelength of the perturbation shrinks up to values smaller than the cell size.

2.4 Intermixing and entropy

Lets consider an alloy AB as a lattice completely filled with atoms of the two species: $N = N_A + N_B$. The number of distinguishable configurations for the system is simply $W = \frac{N!}{N_A! N_B!}$ so that the mixing entropy is given by

$$S_{\text{mix}} = k \ln W = -k \left[N_A \ln \frac{N_A}{N} + N_B \ln \frac{N_B}{N} \right] \tag{2.64}$$

where k is the Boltzmann constant.

For an inhomogeneous system with local density of atoms $n(\boldsymbol{x}) = n_A(\boldsymbol{x}) + n_B(\boldsymbol{x})$ the mixing entropy becomes a functional

$$S_{\text{mix}}[n_A, n_B] = -k \int \left[n_A \ln \frac{n_A}{n} + n_B \ln \frac{n_B}{n} \right] d\boldsymbol{x} \tag{2.65}$$

or equivalently, by defining the local composition as atomic fraction of species i, i.e. $c_i(\boldsymbol{x}) = n_i/n$:

$$S_{\text{mix}}[n, c] = -k \int n \left[c \ln c + (1-c) \ln (1-c) \right] d\boldsymbol{x} = \int n s(c) d\boldsymbol{x} \tag{2.66a}$$

$$s(c) = -k \sum_i c_i \ln c_i = -k \left[c \ln c + (1-c) \ln (1-c) \right] \tag{2.66b}$$

where $s(c)$ is the entropy density (per atom). Entropy is maximized for composition $c = 0.5$ so that it drives the system in the direction of the maximum mixing, i.e. the maximum disorder.

In addition to the entropic contribution, the free energy of mixing can also include an enthalpy of mixing accounting for the different bonding energies between the different components. Lets consider again the lattice model of an alloy AB and E_{AA} the energy of the A–A bond, E_{BB} for the B–B bond and E_{AB} for the A–B bond. If the coordination number of atoms in the crystal is z, said N_{ij} the number of i–j bonds, the internal energy of the alloy is

$$\begin{aligned} E &= N_{\text{AA}} E_{\text{AA}} + N_{\text{BB}} E_{\text{BB}} + N_{\text{AB}} E_{\text{AB}} = \\ &= \left[z \frac{N_A}{2} - N \frac{p_{\text{AB}}}{2} \right] E_{\text{AA}} + \left[z \frac{N_B}{2} - N \frac{p_{\text{AB}}}{2} \right] E_{\text{BB}} + N p_{\text{AB}} E_{\text{AB}} = \\ &= E_0 + N p_{\text{AB}} \left[E_{\text{AB}} - \frac{E_{\text{AA}} + E_{\text{BB}}}{2} \right] \end{aligned} \tag{2.67}$$

where $E_0 = \frac{z}{2}(N_A E_{\text{AA}} + N_B E_{\text{BB}})$ is the internal energy for the pure components A and B separated. p_{AB} is the fraction of A–B bonds and, for a random distribution of atoms A and B, is given by $p_{AB} = z \frac{N_A}{N} \frac{N_B}{N}$. The enthalpy of mixing is then

$$H_{\text{mix}} = Np_{\text{AB}}\left[E_{\text{AB}} - \frac{E_{\text{AA}} + E_{\text{BB}}}{2}\right] \approx \chi\frac{N_A N_B}{N} \tag{2.68}$$

where we introduced the exchange parameter $\chi = z\left[E_{\text{AB}} - (E_{\text{AA}} + E_{\text{BB}})/2\right]$. Notice that the assumption of random distribution holds for $\chi \to 0$. Alloys such to satisfy this requirement are said to be regular.

When considering an inhomogeneous system, eq. (2.68) accounts for the mixing enthalpy density and hence

$$H_{\text{mix}} = \int np_{\text{AB}}(\boldsymbol{x})\left[E_{\text{AB}} - \frac{E_{\text{AA}} + E_{\text{BB}}}{2}\right]d\boldsymbol{x} \approx \int n\chi c(1-c)d\boldsymbol{x} \tag{2.69}$$

The condition of ideal solution $H_{\text{mix}} = 0$ is then obtained for $\chi = 0$, i.e.

$$E_{AB} = \frac{E_{AA} + E_{BB}}{2} \tag{2.70}$$

For values of $\chi > 0$ bonding between atoms of the same kind are favored thus leading to segregation effects, while for $\chi < 0$ A–B bonds are preferred.

The free energy of mixing can then be calculated by summing the enthalpy and entropic contributions:

$$G_{\text{mix}} = H_{\text{mix}} - TS_{\text{mix}} \approx \int n\left[\chi c(1-c) + kT\left(c\ln c + (1-c)\ln(1-c)\right)\right]d\boldsymbol{x} \tag{2.71}$$

The resulting plot is shown in Fig. 2.4 for different ratio $\frac{\chi}{kT}$. Notice that for large values of χ the free energy has two minima, leading to the separation of two phases at the two corresponding compositions (spinodal decomposition). Local chemical potentials are derived by definition:

$$\mu_{\text{mix},i} = \frac{\delta G_{\text{mix}}}{\delta n_i} = \frac{\delta G_{\text{mix}}}{\delta n}\frac{\delta n}{\delta n_i} + \frac{\delta G_{\text{mix}}}{\delta c_i}\frac{\delta c_i}{\delta n_i} \approx \chi(1-c_i)^2 + kT\ln c_i \tag{2.72}$$

where $\frac{\delta n}{\delta n_i} = 1$ and $\frac{\delta c_i}{\delta n_i} = \frac{1-c_i}{n}$.

Finally, also the surface energy can be affected by the mixing as γ would differ according to the alloy composition at the surface c_s. Let's consider again the lattice model for the AB alloy. The surface energy can be straightforwardly defined by counting bonds at the surface. The result is exactly the same of eq. (2.67) except for the different value of the coordination number at the surface z_s. For a random distribution of the atoms,

$$\gamma(c_s) = \sigma\frac{z_s}{2}\left[c_s E_{AA} + (1-c_s)E_{BB} + \chi c_s(1-c_s)\right] \tag{2.73}$$

where σ is the atomic density per unit area and c_s is given with respect to A. For the case of an ideal alloy ($\chi = 0$), the definition of γ reduces to a linear interpolation between the

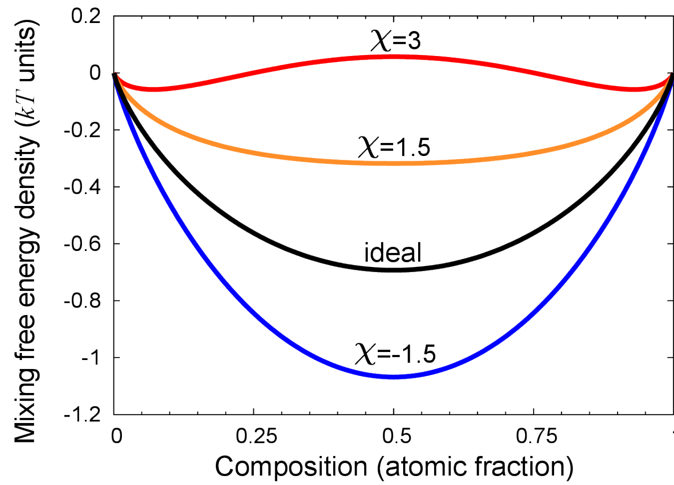

Figure 2.4: Plot of the mixing free energy (per atom) as a function of the local composition c. The curve for ideal alloy is given by the entropic contribution $-TS_{\text{mix}}$ only (eq. (2.66)) while the others includes different values of mixing enthalpy, as given in eq. (2.69) for different values of the exchange energy χ (in kT units).

pure component values:

$$\gamma(c_s) = c_s\gamma_A + (1 - c_s)\gamma_B = \sum_i c_{s,i}\gamma_i, \tag{2.74}$$

with $\gamma_i \propto \sigma \frac{z_S}{2} E_{ii}$ the surface energy for the i-th pure component.

In the following, we will consider the prototype system SiGe as an ideal alloy thus assuming no mixing enthalpy: $G_{\text{mix}} = -TS_{\text{mix}}$. Since the Ge bonding are known to be weaker than Si ones, the definition of ideal alloy is fulfilled by setting $E_{SiGe} = \frac{1}{2}E_{SiSi} + E_{GeGe}$.

3

Tersoff model

In *Ch. 2* the general form of a thermodynamic based model for the characterization of heteroepitaxial growth was discussed. In particular, the transport of material was defined as driven by a local chemical potential, determined from the definition of the system free energy, including surface, elastic and entropic contributions. The model proposed by Tersoff in Ref. [22] and further extended in Ref. [23, 24], is essentially based on the very same assumptions but the overall dynamics of the system evolution is restricted at the surface only, assuming the bulk completely passive during the process. Such an idea proved to capture most of the phenomenology characterizing typical heteroepitaxial systems, offering a consistent treatment for both the profile and composition evolution.

In this chapter we present an extension of the model in literature [24], including a more realistic description of the adatom diffusivity in dependence on the local environment, and apply it to the growth on patterned substrate. The model derivation is carried out in details and simulations are presented for MBE deposition on pit-patterned substrate, up to island formation. An unexpected phenomenon of enhanced pit filling preceding the appearance of islands will also be discussed in details [25]. The main focus in this Thesis is the Ge/Si growth so that specific aspects of the model and results will be referred to such a system. This however do not limit the generality of the approach here discussed so that, by properly changing the parameters, other heteroepitaxial systems could be inspected as well.

The work here discussed is the product of the direct collaboration with Dr. *J. Tersoff* (*IBM, New York - USA*) and, for the experimental data, with the group of Prof. *G. Bauer* at *JKU University, Linz (Austria)*.

3.1 Model definition

Tersoff model is based on the assumption that the whole evolution process is driven only by surface diffusion, so that the overall profile changes are determined by the transport of

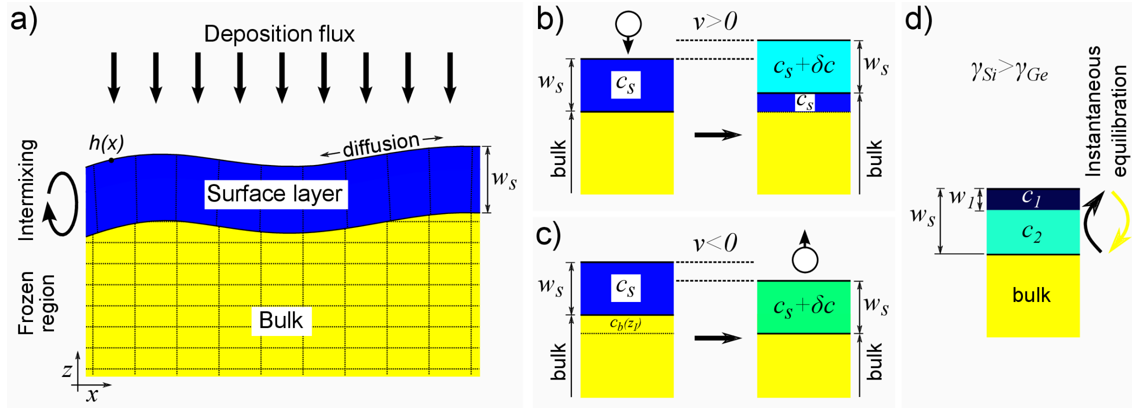

Figure 3.1: a) Schematic representation of the surface profile and bulk region underneath as defined in Tersoff model. The discretization along the x-direction is shown: the bulk is divided in cells each one at a given composition $c_b(x, z)$. b,c) Local variation of the system when adding b) or removing c) an atom (curvature effects are neglected). The variation of composition at the surface layer δc depends on the atomic species considered. d) Schematic representation of the two layer model accounting for surface segregation.

atoms on the surface while leaving immobile all the rest of the solid. In order to account for this, following Ref. [22], the system is split in two regions as schematized in *Fig. 3.1* a):

1. surface region, extending for a finite thickness w_s below the surface profile [18], where all mechanisms of inter-layer atomic exchange are active thus allowing for intermixing [112];

2. bulk region, including all the solid up to a distance w_s from the surface, behaving as a "frozen-in" system, inside which no material transfer is possible since no atomic exchange process is allowed

On more physical grounds, this distinction is aimed to reflect the fact that processes at the surface are much faster than in the bulk where they happen on a much longer time scale, thus producing negligible effects compared to the quick surface phenomenology. The definition of the actual value of w_s can be rather complex as the diffusion dynamics depends on many specific aspects such as temperature, growth flux, surface faceting, ... Calculations in literature [60] permits to restrict the surface region to only few ML. In the following w_s=3 ML is assumed. Simulations performed for different w_s values showed very similar conclusions.

The state of the system is fully characterized by the height profile of the surface, given as a graph, $z = h(x, y)$, and the composition field, distinguished between the local surface composition $c_s(x, y)$ and the bulk composition profile $c_b(\boldsymbol{x})$. Periodic boundary conditions are assumed. In the following, when strictly necessary, a subscript i will be used to identify the chemical species considered, so that the composition $c_i = n_i/n$ accounts for the atomic fraction of the i-th species (n_i is the local density of atoms of i species and $n = \sum_i n_i$). Furthermore, the model derivation will be derived for a generic 3D system but the practical

implementation has been limited to 2D.

Evolution equations accounts for both local changes in the profile height, given as growth velocity $\boldsymbol{v} = v\hat{\boldsymbol{n}}$ along the direction of the local surface normal, and in the composition distribution:

$$\text{Profile:} \qquad v = V_a \sum_i \frac{\partial n_i}{\partial t} \tag{3.1a}$$

$$\text{Surface region:} \qquad V_s \frac{\partial c_{s,i}}{\partial t} = V_a \frac{\partial n_i}{\partial t} - v \begin{cases} c_{s,i} & v \geq 0 \\ c_{b,i}(z_I) & v < 0 \end{cases} \tag{3.1b}$$

$$\text{Bulk region:} \qquad \frac{\partial c_{b,i}}{\partial t} = 0 \tag{3.1c}$$

where z_I is the quota of the surface-bulk interface, $\frac{\partial n_i}{\partial t}$ is the local flux of the i-th component at the surface element at (x, y), including both the material redistribution along the surface, determined by the local chemical potential μ_i, and the deposition flux Φ_i, as given from eq. (2.10) or (2.5), for diffusion or attachment/detachment limited dynamics respectively. More precisely differential quantities must be evaluated along the surface profile, i.e. in (2.10) ∇ operators are replaced by ∇_S. In the following the diffusion case will be considered but all arguments can be easily extended also for the other case. Eq. (3.1a) states that the growth velocity equals the total flux of material [1]. Eq. (3.1b) accounts for the composition variation in the surface element determined by the net flux of the i-th component. This includes both the surface transport term $\frac{\partial n_i}{\partial t}$ and the interaction with the bulk underneath. The latter depends on the direction of motion of the profile (i.e. the sign of v): if $v > 0$ material is left behind from the advancing surface forming an additional region in the bulk at the composition c_s of the growing surface, as sketched in *Fig. 3.1* b); if $v < 0$, part of the bulk immediately below the surface, at composition $c_b(z_I)$, is incorporated into the surface layer, see *Fig. 3.1* c). Finally, eq. (3.1c) excludes all composition variations in the bulk so that it is static as assumed in the model formulation.

Numerical integration of eqs.(3.1) and (2.10), coupled with an update procedure of the bulk composition profile, permits to fully describe the system dynamics once μ_i, Φ_i and M_i are given. An explicit Euler scheme with heuristic control of the time step size was implemented in the simulations.

3.1.1 Free energy definition and local chemical potentials

In order to define the local chemical potentials μ_i, the free energy functional $G = G[z(\boldsymbol{x}), c(\boldsymbol{x})]$ must be defined. By considering surface energy (eq. (2.12)), elastic energy (eq. (2.30)) and

[1] In the approximation of small slopes, the height variation is simply the projectio of v along the z direction, i.e. $\frac{\partial h}{\partial t} = v/\cos\theta$ (θ is the surface inclination). A conversion factor from atomic density to height variation is necessary. The height of the tetragonally distorted Ge/Si film was considered: h_{layer}=1.46Å

mixing entropy (eq. (2.66)), we obtain

$$G = \int_S \gamma d\boldsymbol{S} + \int_V \left(\rho_\varepsilon - \frac{T}{V_a} s \right) d\boldsymbol{x} \tag{3.2}$$

where T is the temperature, γ is the surface energy density, $\rho_\varepsilon = \rho_\varepsilon(\boldsymbol{x})$ is the elastic energy density, and $s = s(c(\boldsymbol{x}))$ is the entropy density from eq. (2.66b) (ideal alloy is assumed). Material density is uniform and equal to $\frac{1}{V_a}$, with V_a the (fixed) atomic volume.

According to the model formulation, eq. (3.2) it is convenient to split the integration domain into the bulk and surface regions of *Fig. 3.1* a):

$$G = G_{\text{surface}} + G_{\text{bulk}} = \left[\int_S \gamma d\boldsymbol{S} + \int V_s(x,y) g(c_s(x,y)) dx dy \right] + \int_{\text{bulk}} g(c_b(\boldsymbol{x})) d\boldsymbol{x} \tag{3.3}$$

where $g = \rho_\varepsilon - T\frac{1}{V_a}s$ is the volumetric free energy density, including elastic and entropic contributions. The integral on the surface region is reduced to the (x, y) coordinates only, since each (infinitesimal) volume element has uniform composition $c_s(x, y)$ (perfect mixing within w_s thickness). Each element is then associated to a volume V_s that, in the limit of small slopes, can be assumed as a circular sector with radius of curvature $1/\kappa$:

$$V_s = w_s \left(1 - \frac{1}{2} \kappa w_s \right) \tag{3.4}$$

The actual definition of energy contributions may be quite difficult due to the lack of accurate data from literature, even for the well studied SiGe system.

In order to properly characterize the system surface energy, anisotropy must be accounted for to obtained the expected faceting. No detailed analysis of the actual $\gamma(\boldsymbol{n})$ function is reported in literature and differences between Si, Ge and SiGe alloys are not clear. In order to avoid arbitrary choice, in 2D we assume $\gamma(\theta)$ to be a simple sinusoidal function with minima roughly corresponding to the stable facets for both Si and Ge [24, 113]:

$$\gamma(\theta) = \gamma_i \left[1 - \alpha \cos(N\theta) \right], \tag{3.5}$$

where γ_i is the isotropic value for the species i, α is a constant representing the degree of anisotropy (here chosen to be $\sim 10^{-3}$) and N is the number of minima for the round angle, corresponding to multiples of $2\pi/N$. For the SiGe system a reasonable choice, for small slope geometries is obtained for N=32, roughly reproducing the usual {105} and {113} facets as the first two minima at 11°and 22°respectively. The very same function is considered for both Si, Ge and SiGe; their difference is only determined by the different isotropic value γ_0 (e.g. γ_{Si}=80 meV/Å and γ_{Ge}=60 meV/Å. Notice that for values of $\alpha > 1/(N^2 - 1)$ strong anisotropy occurs requiring for a proper regularization procedure. Both corner rounding and Frank's convexification procedure were implemented.

In principle, the profile evolution is simultaneous to the atomic displacements leading

to mechanical equilibrium (eq. (2.42)). However, the former process is expected to occur much faster than the latter, as it involves only local rearrangements of the atomic positions. With respect to time scale of transport process described in eqs. (3.1), the system can always be considered in mechanical equilibrium. The elastic energy term entering in the chemical potentials can then by defined by considering the equilibrium strain field. In particular, in the limit of shallow morphologies, the strain at the surface is calculated according to the Flat-Island approximation (*Sect. 2.3.3*), and hence ρ_ε results from eq. (2.56). Notice that $\rho_\varepsilon = \rho_\varepsilon(c)$, as the eigenstrain $\varepsilon^\star$ depends on c. In the following Ge/Si elastic parameters are used: Young modulus Y=103 GPa and the Poisson ratio ν=0.26 [47]. The strain field is solved by means of FFT algorithm according to eq. (2.54), with a cutoff of the order of a few atomic distances $b \sim a_{\mathrm{Si}}$.

Local chemical potentials at the surface $\mu_i(x, y)$ can be calculated as the variation in the free energy G (eq. (3.3)) upon addition of an extra atom of species i at a given point of the surface:

$$\mu_i = \frac{\delta G}{\delta n_i} = V_a \kappa \gamma_s + \frac{\delta G}{\delta V}\frac{\delta V}{\delta n_i} + \frac{\delta G}{\delta c}\frac{\delta c}{\delta n_i} \tag{3.6}$$

The first term is the variation in surface energy due to the profile evolution, as derived in *Sect. 2.2* (γ_s is the surface stiffness), while the other two account for the variation in the volumetric energy density, due to the change in volume (δV) and composition (δc), respectively.

Again, the distinction between surface and bulk region in the model allows to simplify the calculations. As sketched in Fig. 3.1 b), for a flat surface, the volume change is entirely in the bulk region while the surface region only changes in composition:

$$\frac{\delta V}{\delta n_i} = \frac{\delta V_b}{\delta n_i} = V_a \qquad \frac{\delta c_s}{\delta n_i} = \frac{(1 - c_{s,i})V_a}{V_s} \tag{3.7}$$

Relations above are valid also for the limit of shallow profile, neglecting higher order corrections due to the volume variation of the surface region elements, $\delta V_s \approx V_a \kappa w_s$. Substituting into eq. (3.7) and recalling that $\frac{\delta G}{\delta V_b} = g(c_s)$ since the additional bulk is derived from the surface layer, local chemical potentials are finally obtained:

$$\begin{aligned} \mu_i &= V_a \left[\kappa \gamma_s + g(c_{s,i}) + (1 - c_{s,i}) \frac{\delta g}{\delta c_{s,i}} \right] = \\ &= V_a \kappa \gamma_s + kT \ln c_{s,i} + V_a \left[\rho_\varepsilon(c_{s,i}) + (1 - c_{s,i}) \frac{\delta \rho_\varepsilon}{\delta c_{s,i}} \right] \end{aligned} \tag{3.8}$$

3.1.2 Two-layers model for surface segregation

In the simple approach discussed above surface energy was assumed a constant, identical for both species considered. In the opposite case, when substantial differences in surface

energies are expected, surface segregation of the component with lower γ is typically observed. For the prototype SiGe system, $\gamma_{\text{Si}} > \gamma_{\text{Ge}}$ (approximately, 80 and 60 meV/Å^2 respectively [44]), so that Ge segregation occurs during the growth [114].

In order to properly account for this effect, as schematized in *Fig. 3.1* a), the surface layer itself is split in two regions [23, 24], an uppermost layer of thickness w_1, at local composition c_1 determining the surface energy cost, and the sub-surface layer below, $w_s - w_1$ thick, at composition c_2. In the following we identify the topmost layer as the first atomic layer, i.e. w_1=1 ML and still consider w_s=3 ML. Compositions of the two layers are bounded by the average surface composition c_s such that:

$$V_s c_s = V_1 c_1 + V_2 c_2 \tag{3.9}$$

where element volumes V_1 and V_s are given from (3.4) for thicknesses w_1 and w_2 respectively and $V_2 = V_s - V_1$.

In this picture, the surface energy γ is determined by the composition c_1 of the topmost layer only. In the assumption of ideal alloy, $\gamma = \gamma(c_1)$ is defined by a linear interpolation between the values of pure components as derived in eq. (2.74), i.e. $\gamma(c_1) = c_1\gamma_{\text{Si}} + (1 - c_1)\gamma_{\text{Ge}}$. Consequently, the system free energy G can be obtained from eq. (3.3) separating the contributions from the two regions in the surface layer:

$$G = G_{\text{surface}} + G_{\text{bulk}} = \left[\int_S \gamma(c_1)d\boldsymbol{S} + \int \left(V_1 g(c_1) + V_2 g(c_2)\right) dxdy\right] + \int_{\text{bulk}} g(c_b)d\boldsymbol{x} \tag{3.10}$$

By imposing that the two layers are in local equilibrium, a redistribution of Si and Ge between them occurs, in such a way that Ge is accumulated at the top of the surface, minimizing the local free energy. The process is assumed to occur instantaneously, i.e. local atomic exchanges are much faster than any other transport process along the surface (as for intermixing mechanisms for the single-layer model). The average composition c_s do not vary as well as volumes V_1 and V_2 so that, according to eq. (3.9), composition variations should satisfy the constrain $V_1\delta c_1 + V_2\delta c_2 = 0$. By minimizing the free energy G under this constrain, the equilibrium condition is defined as:

$$\frac{1}{V_1}\frac{\delta G}{\delta c_1} = \frac{1}{V_2}\frac{\delta G}{\delta c_2}, \tag{3.11}$$

Taking G from eq. (3.10) we then obtain:

$$\frac{1}{V_1}\frac{\delta \gamma}{\delta c_1} + \frac{\delta g}{\delta c_1} + \frac{\delta g}{\delta c_2} = 0 \tag{3.12}$$

and substituting the explicit values for g for elastically isotropic ideal alloy (eqs. (2.74),

(2.66), (2.40)):

$$\frac{1}{V_1}\Delta\gamma + 2\frac{Y}{1-\nu}V_a\varepsilon^{\star 2}(c_1 - c_2) + kT\left[\ln\frac{c_1}{1-c_1} - \ln\frac{c_2}{1-c_2}\right] = 0, \tag{3.13}$$

where $\Delta\gamma$ is the difference in surface energy for the two components, e.g. $\gamma_{\mathrm{Si}} - \gamma_{\mathrm{Ge}}$, and is the only term in the equation that leads to surface segregation (if $\Delta\gamma = 0$ no segregation occurs, i.e. $c_1 = c_2$). As the average composition c_s is known, the numerical solution of eq. (3.13) together with (3.9) return the equilibrium values for c_1 and c_2.

Eq. (3.13) define the equilibrium composition for a static system. This equilibrium is destined to dynamically change as the system evolve. In order to define the evolution of the system, eqs. (3.1), derived for the single layer model, can be still applied, just correcting eq. (3.1b) by replacing $c_{s,i}$ on the right hand side with $c_{2,i}$ in order to account for the actual composition of the material left in the bulk when the surface advances, now originating from the sub-surface layer. The resolution is coupled with the local equilibrium condition in the surface region from eq. (3.11), so that growth simulations could be done by evolving the average surface composition according to the amended eq. (3.1b) recalculating the equilibrium at each time interval. Actually by coupling eq. (3.1b) with (3.11) it is possible to derive analytically the evolution rates for both c_1 and c_2 directly.

Since G depends on the composition in the two layers (eq. (3.10)), local chemical potentials μ_i are calculated accordingly, by considering variations in both compositions δc_1, δc_2 (subject to the equilibrium constrain), and element volumes $\delta V_1 \sim \kappa w_1$, $\delta V_2 \sim \kappa(w_s - w_1)$. In a first, approximation, by neglecting curvature corrections we fall back to eq. (3.8) provided that c_s is replaced by c_2 and $\gamma_s = \gamma_s(c_1)$.

3.1.3 MBE Deposition Flux

Deposition flux Φ_i is easily defined when considering Molecular Beam Epitaxy (MBE). Atoms emitted from the source form a collimated beam impinging on the sample from a fixed direction. Typically the sample is spinning during the growth in order to homogenize the material accumulation so that, at least for shallow sample morphology, the resulting growth flux is the same of a flux directed along the vertical direction (see *Sect. 5.3.1*). Furthermore, the beam size is in general large enough to assume a uniform flux on the overall sample area. The local growth flux is then given by the projection of the external nominal flux Φ_0 along the normal to the surface:

$$\Phi_i(x) = \Phi_{0,i}\cos\theta(x) \tag{3.14}$$

where $\theta(x)$ is the local inclination of the surface, i.e. the angle formed by the normal with respect to the vertical direction.

3.1.4 Surface mobility

An accurate determination of the actual adatom mobility is not yet available in literature because of its complex dependence on many specific aspects such as the different surface orientation and reconstruction [115] and strain [116, 117]. Furthermore, it was also shown [118] that dimers can substantially contribute to the transfer of material along the surface so that an effective mobility should be defined.

Here we assume the mobility for each component i to be given by two factors, the local diffusion coefficient for that species D_i and local density of adatoms of such kind η_i:

$$M_i = D_i \eta_i \tag{3.15}$$

The former accounts for the rapidity of the transport process when considering an adatom of species i on the surface, the latter indicates the number density of such adatoms that are available to be transferred.

Our simple model is intended only to qualitatively capture the essential aspects of the real, complex diffusion mechanisms [119, 120]. By considering all macroscopic transfers of material direct consequence of the elementary events of atomic diffusion, the classic theory for random-walks can be used to define the diffusion coefficient D_i for atoms of i species by an Arrhenius law

$$D_i = D_0 \exp\left(-\frac{B_i}{kT}\right), \tag{3.16}$$

where B_i is the activation energy barrier for the atomistic hopping process and D_0 can be expressed as a function of the hopping frequency r_0 (i.e. the vibrational frequency $\sim 10^{12} - 10^{13}\mathrm{s}^{-1}$ [114]) and the site distance a: $D_0 = \frac{1}{2} r_0 a^2$. Actual values of D_0 are in general not known. In the following we assume the hopping between in-plane nearest-neighbors sites of the Si structure ($a \simeq$3.8Å) and set $D_0 \simeq 5 \cdot 10^{-3}\mathrm{cm}^2/\mathrm{s}$. In principle D_0 should differ for Si and Ge [114] but for the sake of simplicity we neglect this effect (furthermore it would surely be less relevant than the exponential dependency of the energy barrier).

In a simple bond-breaking picture of atomic diffusion, each adatom can move only after breaking the bonds that hold it at its site on the surface and hence, the activation barrier B_i is roughly determined by such bonding energy. Accordingly, different values D_i are expected for atoms of different species: strongly bonded atoms move much slowly than those forming weak bonds, i.e. Ge adatoms move faster than Si ones because of their weaker interaction with the surface [22]. For the very same reasons, a dependency of the activation barrier on the local surface composition $B_i = B_i(c)$ is expected, due to the different strength of bonds formed between adatoms and the local environment of the surface on top of which they move (composition dependent diffusivity was observed in bulk materials [121]). In the two layers model, in particular, this requires to include an explicit dependency of this energy barrier (and consequently of the diffusion coefficient)

on the composition c_1 of the topmost layer. By a linear approximation, it is possible to define:

$$B_i(c_1) \propto \sum_j c_{1,j} E_{i,j}, \tag{3.17}$$

where $E_{i,j}$ is the bonding energy between an atom of species i and one of species j. The proportionality coefficient should account for the different number of bonds established at the hopping site.

In the absence of a literature determination of activation energies for diffusion, in our simulations we set $E_{\text{Si-Si}}$=1.4 eV and $E_{\text{Ge-Ge}}$=1.0 eV and, in the assumption of ideal alloy (see *Sect. 2.4*), $E_{\text{Si-Ge}} = 1/2\,(E_{\text{Si-Si}} + E_{\text{Ge-Ge}})$=1.2 eV. A similar choice was already made in previous Kinetic Monte Carlo simulations [114]. However, the specific barrier values here chosen should be only regarded as an attempt to yield a tentative, average macroscopic description of the complex atomic-scale processes underlying to the system evolution [119].

The definition of the adatom density η_i requires to consider the adatom distribution on the surface and can be quite a complicated stuff. In the assumption that the adatoms are in equilibrium with the surface, the adatom density for a given species i can be considered directly proportional to the local composition of c_i of the surface. This is a commonly used approximation leading to the simple Fick's diffusion.

It is however reasonable to consider that adatoms distribution may vary according to its local stability, i.e. on the local chemical potential μ_i. Wherever the surface is more stable, the cost to remove adatoms is higher (i.e. lower value of μ_i) and hence a smaller amounts of adatoms can be generated, while at unstable locations, where μ_i is larger, more adatoms are formed in order to favor an energy reduction by redistributing the material along the surface. The density of adatoms η_i can then be related to the equilibrium generation of atoms, following an Arrhenius relation:

$$f_i \sim \exp\left(-\frac{E_0 - \mu_i}{kT}\right) \tag{3.18}$$

where E_0 is the energy barrier to produce an adatom from a pure flat surface (that is for μ_i=0). Even if in principle E_0 should be different for each component, here we neglect this possibility (this can be considered already included in the diffusion barrier definition in eq. (3.17)). It is easy to see that the entropic part of μ_i determines a direct proportionality between adatom density and surface composition, i.e. $\eta \propto c_s$ for the single layer model ($\mu_i \sim kT \ln c_{s,i}$) while, for the two-layers case, $\eta \propto c_2$. The other contributions in the exponential term then accounts for the local surface and elastic energy (some corrections related to the local curvature κ are also included). With typical parameters it was verified that deviations from c_2 are usually smaller than 1%.

3.2 Growth simulations on flat substrates

In literature several models for Stranski-Krastanow growth on flat substrate are proposed [8–10, 18, 23, 24, 110, 111, 122, 123]. One of the main advantages of Tersoff model is the possibility to consider the dynamics of the composition as well as the profile evolution, so that its role in the raise and propagation of the surface instability (*Sect. 2.3.4*) can be directly accounted for during the process.

Before considering a full simulation for the island growth it is interesting to analyze the evolution of the composition profile in connection with the effect of surface segregation in the absence of any elastic contribution.

Deposition of Ge on the flat Si substrate leads to a gradual increase of the surface Ge content while Si rich material is left in the bulk below. According to eq. (3.11), at each instant of the growth a local redistribution of Si and Ge occurs between the two partitions of the surface layer, leading to the accumulation of Ge in the uppermost layer due to its lower surface energy. The equilibrium mainly depends on the balance between surface energy and entropy of mixing, the former favors the accumulation of Ge in the topmost layer while the latter tends to make homogeneous the whole surface region. Temperature determines the ratio between such terms: the higher is temperature, the stronger is the mixing tendency. Composition profiles obtained at different growth stages

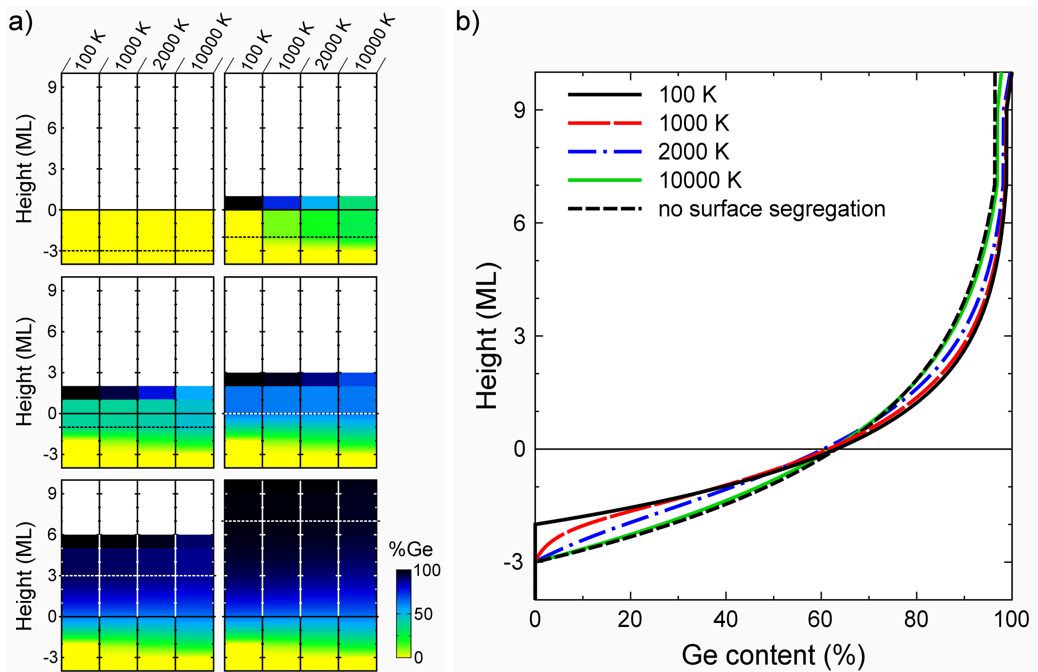

Figure 3.2: Composition profiles after deposition of Ge on a flat Si substrate (w_s=3 ML and w_1=1 ML). a) Growth sequence for different number of ML Ge deposited at four temperature 100, 1000, 2000 and 10000 K. A dashed line is used to indicate the interface between the surface and bulk region. b) Comparison between the composition profiles after deposition of 10 ML Ge. The curve obtained for the single layer model with no surface segregation is also shown.

and for different growth temperature are shown in *Fig. 3.2*. As evident in panel a), at the lowest temperature considered (100 K) the segregation of Ge is almost perfect so the first layer of the surface is filled with pure Ge (c_1=100% Ge) immediately after 1 ML Ge is deposited. Correspondingly, the composition c_2 of the underlying layer remains 100% Si up to that point and then the additional Ge mixes and is gradually buried into the bulk, up to get pure Ge in the whole surface layer (asymptotic limit). By increasing the temperature, the tendency to intermixing is enhanced and hence more Si is retained into the topmost layer while a larger part of the Ge deposited is directly accumulated in the region below. In the limit of very high temperature (10000 K), the difference in surface energy between Si and Ge becomes almost ineffective and the intermixing involve the whole w_s thickness of the surface region, as if there were no segregation at all, i.e. $c_1 = c_2$. This is confirmed by comparing the profile with that predicted by the single layer model as showed in *Fig. 3.2* b). The bulk region below the initial surface layer (i.e. height $< -w_s$=-3 ML) is not modified at all.

The overall behavior of composition profiles essentially describes an exponential increase of Ge content moving from the bulk to the surface up to saturation at pure Ge. This is clearly the behavior predicted in (3.1b) for the single layer model [18] when assuming $\frac{\partial n_{\rm Si}}{\partial t} = 0$ and $v = \dfrac{\partial n_{\rm Ge}}{\partial t} = \Phi$ so that

$$w \frac{\partial c}{\partial t} = -c\Phi \quad \longrightarrow \quad c(t) = 1 - \exp\left(-\frac{\Phi t}{w_s}\right) \tag{3.19}$$

where c accounts for the surface Ge content. Since Φt is the thickness of Ge deposited, the composition decays exponentially with the distance from the surface up to the bulk value, for a depth determined only by the thickness w_s of the surface layer.

Deviations of the profiles from the proper exponential curve are determined by the effects of surface segregation and mainly affect the first deposited layers. By looking to the curves in *Fig. 3.2* b) it is evident that the profiles tend to perfectly follow an exponential for both temperature limits and only in the intermediate range some discrepancy is found. This is easily explained according to the previous discussion. At high growth temperature segregation is negligible and mixing occurs on the overall surface region. At low temperature, Ge is initially accumulated only in the topmost layer so that no Ge is buried in the bulk for a thickness corresponding to w_1, but when this is completed, all the rest of Ge deposited mixes in the subsurface only so that the following evolution is the same described by the single layer model with respect to the subsurface region only. This is well confirmed in *Fig. 3.2* b) by noting that the exponentials for the two limiting cases are not simply shifted by w_1 but at low temperature the decay is on shorter length scale as it is determined only by $w_s - w_1$.

The simple growth considered so far is however not observed for the typical heteroepitaxial systems as there is always some misfit strain leading to Stranski-Krastonow islands

(dislocated flat films can also be grown but at low temperature or high flux that could hinder the intermixing). As discussed in *Sect. 2.3.4*, a strained flat film is unstable with respect to profile perturbations so that as few layers of Ge are deposited a morphological instability raise and leads to the island formation [23, 24]. As discussed in Ref. [23], the formation of islands occurs after a certain amount of Ge is deposited, i.e. there exists a critical thickness beyond which the profile gets unstable and islands appear.

In *Fig. 3.3* the raise of the instability is shown for deposition of Ge/Si substrate. Up to about 2.5 ML the profile remains nearly flat but then a perturbation arise and leads to the island growth. A certain degree of surface anisotropy, as given from eq. (3.5), is accounted for so that the first islands, observed at 2.7 ML, tend to form {105}-like facets (11°). The further addition of Ge induce at 2.8 ML the transition of the largest island (at the center) to steeper {113} facets (22°). At the same time trenches are excavated on the borders of the central island, where compressive strain is accumulated, and Si rich material is extracted from the layers grown in the first stages and, lately, from the Si substrate, and incorporated into the surface layer. Surface diffusion driven by the mixing contribute tends to redistribute the Si recovered from the bulk all along the profile thus opposing to the enrichment in Ge caused by the deposition flux.

The observed behavior can be considered as a complex case of the ATG instability discussed in *Sect. 2.3.4*. As indicated in *Fig. 2.3* the instability depends on the film composition, the larger is Ge content, the shorter is the wavelength of the fastest growing perturbation. During Ge deposition then a gradual shortening of the instability wavelength is expected while the surface becomes rich in Ge. Initially, with almost pure Si, the perturbation length scale is very long (exceeding the size of the simulation cell) and slow so that the profile remains flat and grows according to *Fig. 3.2*. As the content of Ge increases, shorter wavelengths become unstable and finally the perturbation grows strong enough to produce a visible corrugation in the profile. However, the state of the system is continuously changing since additional Ge is provided by the deposition flux while Si rich material is incorporated from the bulk region and correspondingly, the actual distribution of unstable wavelengths dynamically changes according to the balance between the two processes.

Notice that a perfectly flat substrate cannot develop any instability never mind the accumulation of strain. An initial perturbation is required in order to trigger the evolution and this can be achieved by considering a small dimple on the initial profile. An alternative solution, used in the simulation in *Fig. 3.3* consists in assuming an initial non-uniform strain distribution, independent of the morphology and composition so that a perfectly flat pure Si profile can be used. From a physical point of view, this is equivalent to consider an initial stressor (e.g. a small Ge island) buried into the bulk, such to produce differences in the local strain triggering the development of the instability when additional strain is accumulated.

Finally, it is essential to keep in mind that simulations rely on the assumption of

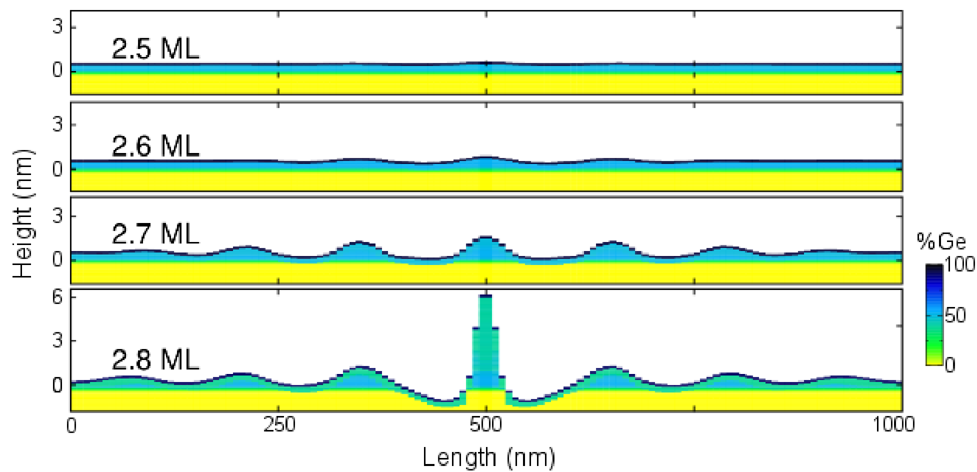

Figure 3.3: Simulation profiles obtained after Ge deposition on a flat Si substrate. Only the stages where the island growth occurs are shown. Anisotropic surface energy is considered so that islands tend to form {105} and {113} facets (with inclination 11°and 22°).

shallow profiles, especially for the calculation of the strain field at the surface, based on the Flat-Island approximation. As islands grow higher in aspect-ratio, the elastic term is poorly evaluated and simulations lose of significance.

3.3 Growth simulations on pit-patterned substrates

3.3.1 Smoothing of single component pit

The problem of profile evolution for one component systems has been vastly investigated in literature since the seminal work by *W. W. Mullins* in Refs. [3, 97] (see for example [4, 124]). The analysis of this case, much simpler than the heteroepitaxial growth process, offers a direct insight on the role played by the surface energy contributions when considering non-planar geometries. Furthermore, this analysis permits to define the natural evolution of the pattern itself, independently on the growth process, offering useful indications on the initial profile stability and geometry.

For non-planar one component systems, the evolution is entirely due to the surface energy minimization (*Sect. 2.2*), driving the system to minimize the exposed surface and, in case of anisotropic γ, to form facets corresponding to the preferential orientations of minimum energy.

The evolution of a sinusoidal profile for isotropic γ is shown in *Fig. 3.4* a). Simulation parameters are those of Si as if a pit patterned Si substrate were considered. As indicated by the profile sequence, the surface morphology tends to flatten in order to expose the minimum surface possible. All profiles preserve the original sinusoidal geometry while the amplitude shrinks to zero. A regular slow down of the process is evident as the amplitude gets smaller. The observed behavior is easily explained analytically. Given a shallow

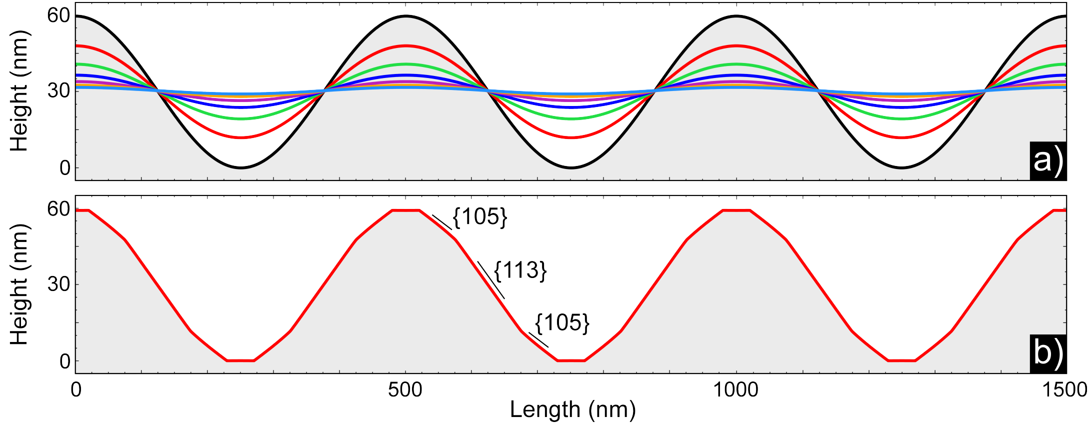

Figure 3.4: Smoothing of a sinusoidal surface profile mimicking a pit patterned Si substrate (T =720°C, $B = B_{Si}$=1.4 eV). In a) isotropic $\gamma = \gamma_0$ =80 meV/Å^2 is considered and profiles are reported at regular time intervals (every 2500 s). In b) anisotropic $\gamma = \gamma_0 \left[1 - 0.1 \cos\left(32\theta\right)\right]$ is assumed (Frank's convexification [29] was used for regularization, see *Sect. 2.2.1*). Initial and intermediate profiles are not shown as they would be barely distinguishable from the final faceted geometry.

profile $h(x) = a\cos\left(qx\right)$ and isotropic energy density γ, the local chemical potential is simply

$$\mu = \kappa\gamma = \gamma q^2 a \cos\left(qx\right) \tag{3.20}$$

where we used the small slope approximation $\kappa = -\frac{d^2h}{dx^2}$. Diffusion equation then implies

$$\frac{\partial h}{\partial t} = M\nabla^2\mu = -M\gamma q^4 a \cos\left(qx\right). \tag{3.21}$$

with M the material mobility. The profile evolution is then solved by a decay of the cosine amplitude $h(t) = a(t)cos(qx)$, where

$$a(t) = a(0)\exp\left(-M\gamma q^4\right) \tag{3.22}$$

As expected the decay rate is larger for high mobility M or surface energy γ and strongly depends on the structure periodicity q. The variation of the pit amplitude indicated by the sequence of profiles in *Fig. 3.4* a), sampled at regular time intervals, follows the expected exponential decay.

Surface anisotropy can strongly change the flattening tendency, eventually leading to a non-planar fully faceted profile if some orientations are much favored by low γ values. This is what happens in *Fig. 3.4* b) where the profile obtained when annealing the sinusoidal profile in a) for a strongly anisotropic γ (defined as in eq. (3.5) to mime {105} and {113} stable facets of Si (at 11°and 22°, respectively) is reported.

3.3.2 Ge/Si growth on pit patterned substrate: anomalous pit filling and island growth

As discussed in *Sect. 1.2* when the heteroepitaxial growth is performed on a pit patterned substrate, for suitable conditions, islands are formed into the pits and their shape gets steeper as the growth proceeds.

Recent experimental observations for Ge/Si MBE growth [25, 125], revealed that the pit itself plays an active role in the system evolution undergoing a substantial change in shape after deposition of few Ge ML, preceding the appearance of islands. The magnitude of this effect can be appreciated from *Fig. 3.5*, where an AFM analysis of the pit morphology is shown for the initial Si pits (a-c) and for their state after deposition of 3.5 ML Ge (d-e) at 720°C for a growth rate of 0.03 Å/s. From the analysis of the surface orientation map (SOM) in c) it is possible to see that the initial Si pits exhibit a multifaceted profile, with {001}, {11n}, {113} and {15 3 23} facets [72] that, after Ge deposition, transform into a much shallower pyramidal shape with {105} facets, as showed by the SOM in f). This corresponds to a substantial variation of the facet steepness, from ∼22°of {113} to ∼11°for {105}, so that the evolution is not a simple facet rearrangement [71], but consists of a massive flow of material from the upper surface into the pit. The extent of the net smoothing is made clear in *Fig. 3.5* g) where AFM linescans, measured before and after the deposition of 3.5 ML of Ge, are compared.

The volume of material accumulated into the pits is much larger than the small quantity of Ge deposited (enough to cover the surface with a thickness of about 0.5 nm only) so that most of it must be Si. Etching experiments confirmed that content in Ge is only ∼10%. This is however unexpected since the initial pit pattern is stable at the usual growth conditions and should not be modified. Si pits are in fact excavated by a procedure of Reactive Ion Etching (RIE) followed by deposition of additional Si at high temperature forming a buffer layer several tens of nanometers thick that permits a regularization of the etched profile leading to a well defined pit shape exposing the typical stable facets of Si observed in the SOM in *Fig. 3.5* c). Since the pure Si pits are not expected to evolve it must be the small amount of Ge deposited to activate the Si motion.

Given the simplicity of our model and the complexity of real Ge/Si(001) surfaces, we cannot expect quantitative agreement with experiment, and we have focused on qualitative aspects of the behavior. First of all, we want to inspect the origin of the anomalous smoothing observed in the experiments, so that we first consider the simplest conditions, excluding the effects of misfit strain and surface anisotropy, thus limiting the analysis to the initial growth stages.

The sinusoidal profile showed in *Fig. 3.6* a), mimicking the experimental pit geometry, is considered as initial profile. Growth simulations are then performed at the experimental growth flux and temperature. The predicted profile after deposition of 3.5 ML Ge, showed in *Fig. 3.6* b), shows a significant smoothing of the pit, characterized by the accumulation

of material at composition ∼20% Ge, revealing a dominant flow of Si. The magnitude of the smoothing process can be better appreciated by looking to *Fig. 3.6* c), reporting the decay of the pit amplitude Δh, i.e. the height difference between the maximum and minimum along the profile, for both the Ge/Si growth simulation and the natural evolution of the initial Si pits with no deposition (equivalent to Si/Si growth except for a shift in the profile due to the flux). Clearly, upon Ge deposition, despite the diffusing material results 80% Si, the smoothing is nearly an order of magnitude faster than for pure Si (initial Si profile is almost stable). Simulations then captures the anomalous pit filling effect discussed above [25].

One of the key assumption that was introduced in the model here discussed is the variation of adatom mobility according to the local surface composition, according to eqs. (3.16) and (3.17). This is a crucial contribution to obtain the smoothing effect, determining a lowering of the diffusion barrier of Si as the surface gets rich in Ge. In contrast, the simpler assumption of constant diffusion coefficients, accounting only for $D_{Ge} > D_{Si}$, do not produce any anomalous effect of pit filling but the smoothing occurs at a rate only slightly different from that of pure Si, as confirmed by simulation results showed in the dashed line in *Fig. 3.6* c). The evolution is then found to be kinetically limited by the slowest species Si in agreement with the observations in Ref. [22].

The magnitude of the anomalous pit filling relies on the substantial Ge enrichment of the surface layer thanks to surface segregation. This is made evident by looking to the dotted line in *Fig. 3.6* c), reporting the profile decay predicted for the very same conditions of the full simulation (including the dependence of diffusivity on local surface composition) except for the exclusion of surface segregation. Still a substantial smoothing occurs, but much less than in the full calculation, because of the lower Ge content at the surface, as indicated in *Fig. 3.6* d).

The physical origin of the anomalous smoothing is then mainly determined by the

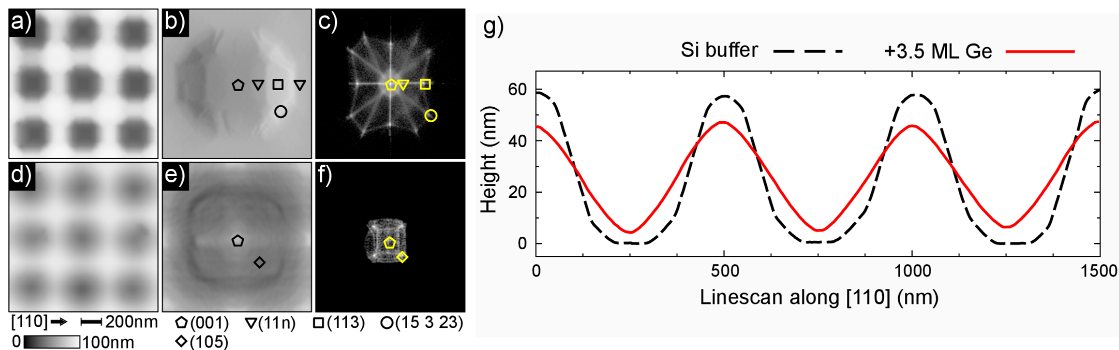

Figure 3.5: AFM images of the substrate Si pits after 50 nm buffer growth (a-c) and after subsequent deposition of 3.5 ML of Ge (d-e) at 720°C and flux of 0.03 Å/s. In a,d) the pit array is shown, while in b,d) an enlarged view of single pits is reported. In e,f) surface orientation maps are reported indicating which facets are present. g) AFM linescans through the pit centers along [110] direction, for the pits before and after deposition. Vertical offset between curves is arbitrary.

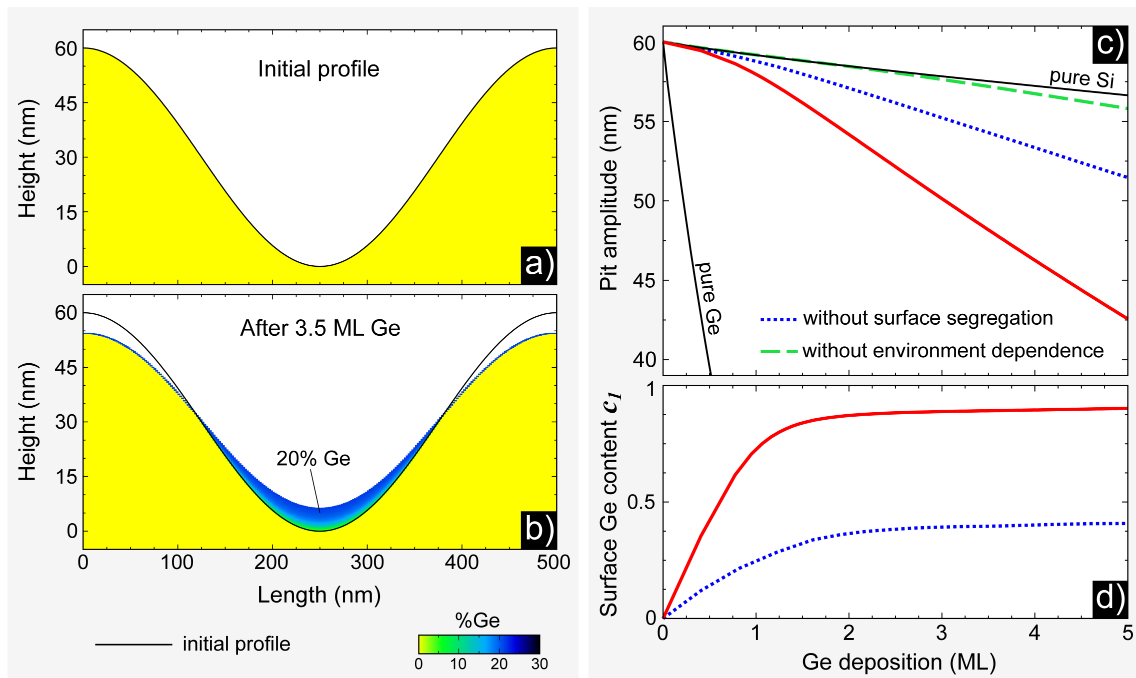

Figure 3.6: a) Initial profile mimicking the Si pits of experiments in *Fig. 3.5*. b) Simulation profile and composition map obtained after deposition of 3.5 ML of Ge at 720°C and flux 0.03 Å/s (the topmost atomic layer, at ∼85% Ge, is omitted). c) Decay of the pit amplitude during Ge deposition. The solid red curve is the full calculation. The dashed curve show the behavior obtained when assuming no dependence of the energy barriers from local composition, while the dotted curve show the effect of omitting Ge surface segregation. The smoothing curve of pure Si and pure Ge pits is shown for reference. d) Evolution of the composition of the topmost atomic layer c_1 during growth for both the cases including or omitting surface segregation as in a). The average composition along the profile is considered (variations across the surface are within 1%).

dependence of the Si diffusivity on the surface composition, but the effect is strongly enhanced by surface segregation. A clear understanding of this synergy can be found by closely comparing Figs. 3.6 c) and d). The very first initial stages, where the surface is almost pure Si, are characterized by a slow evolution, comparable to annealing pure Si. However, the initial deposition of Ge induce a rapid accumulation at the topmost surface layer indicated in Fig. 3.6 d) that determines an increase smoothing rate, i.e. the slope in Fig. 3.6 c). When less than 2 ML of Ge are deposited, the surface composition is ∼85% and the evolution follows a quasi-steady state with a relatively constant decay rate.

This behavior strongly depends on the growth temperature, mainly responsible for the Si and Ge mobility. By decreasing the temperature, for example at 550°C as showed in panel a), both Si and Ge motion is almost suppressed and Ge grows nearly conformal all along the surface, in agreement with some low temperature experiments [125]. On the contrary, at higher temperature, e.g. 850°C as in panel b), a large amount of material can move into the pit and the composition drops to ∼15% thus indicating that most of the material transfer is due to the motion of Si. However, at such high temperature, the mobility of pure Si increased too so that initial pits are no more stable and undergo a significant

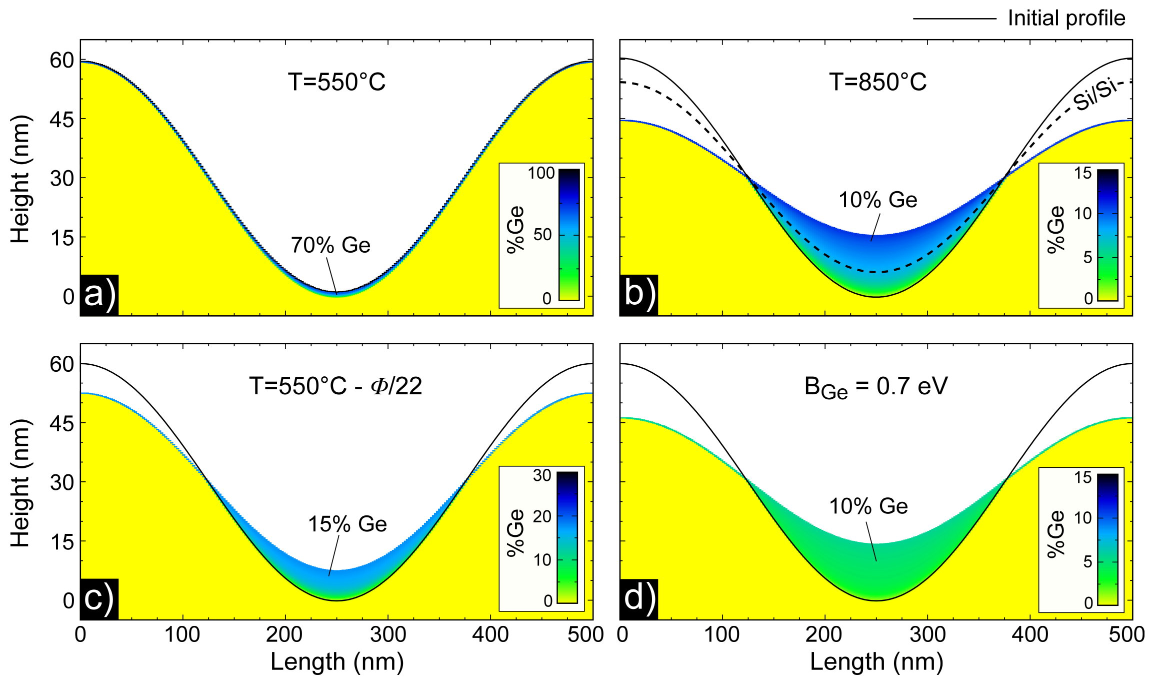

Figure 3.7: Simulation profile and composition map for deposition of 3.5 ML Ge for different parameters with respect to the case in *Fig. 3.6*. Growth temperature is varied to 550°C in a) and 850°C in b). In c), a flux reduction of a factor 22 is considered for the case at 550°C. In d) a lower activation barrier for Ge diffusion B_{Ge} = 0.7 eV. The solid line show the initial profile before growth. The evolution of the Si pits when depositing Si is not distinguishable from the initial profile except for the case b) where it is indicated by a dashed line. The topmost layer ~80% Ge is omitted in b-d).

smoothing by themselves, indicated by the dashed curve in *Fig. 3.7* b), where deposition of Si is considered at the same conditions of Ge growth. However, the smoothing obtained upon Ge deposition is much larger than that observed for pure Si so that an enhancement of Si mobility is definitely determined by the small quantity of Ge deposited, but the relative variation is smaller.

As showed in *Fig. 3.7* c), the effect of temperature can be balanced by a suitable variation of the growth flux. In particular, when reducing the growth temperature from the 720°C of *Fig. 3.6* to the 550°C of *Fig. 3.6* a), the average diffusivity is expected to decrease by a factor ~22 leading to a slower evolution. If the flux is reduced by the same factor, as done in the simulation of *Fig. 3.7* c), a longer time is required to perform the same deposition of 3.5 ML Ge and this allows for a larger smoothing, even larger than at 720°C, as the difference in activation energies is larger relative to kT.

The magnitude of the effect of pit filling can be dramatically enhanced by assuming a lower barrier for Ge diffusion. This is shown in Fig.3.7 d), where B_{Ge} is reduced of 30% (all other parameters are as in Fig. 3.6).

In this case, the same 3.5 ML Ge deposition of *Fig. 3.6* b) leads to a much greater smoothing and the material filling the pit results only around 10% Ge, thus indicating a

more pronounced enhancement of Si mobility. The extent of the smoothing looks even in better agreement with the experiments reported in *Fig. 3.5*. However, a detailed comprehension of the diffusion properties of both species is far from being well understood so that it is not possible to assess what are the most reasonable parameters. Anyway, *Fig. 3.7* d) highlight the possibility to have even stronger anomalous pit-filling effect, in other systems with larger differences in surface bond strength.

So far we limited our description to the initial stages of the growth, neglecting the strain effects typical of most heteroepitaxial systems, in order to highlight the physical origin of the anomalous pit filling. For later stages, involving a larger Ge accumulation, such an approximation is no more justified as evidenced in *Fig. 3.8* where the prosecution of the growth simulation of *Fig. 3.6* to higher Ge coverage is considered for both the case without elastic terms (panel a) and including such contributions in the free energy definition (panel b). In the former case, the system is mainly driven by surface energy and then the anomalous smoothing continues up to the complete flattening of the profile, as in a). In the latter case, Ge deposition determines a continuous accumulation of elastic energy that at some point prevails on the surface energy cost, leading to the formation of islands. At the earliest stages of the growth, e.g. at 2 ML Ge, profiles do not differ very much for the two cases, so that we conclude that the initial anomalous smoothing is not significantly dependent on strain. As Ge coverage increases, elastic effects become dominant and, as shown in *Fig. 3.8* b), leads the pit bottom toward flattening and finally an island forms at the center of the pit [47]. The evolution is driven by the search for a better strain release, so that the island, once formed, tends to grow in aspect ratio when increasing volume [72, 126, 127].

The mechanism is analogous to what discussed in *Sect. 3.2* for the growth on flat substrate, but here the arise of the instability [17] is guaranteed by the smoothing process itself, forming a Ge rich region at the bottom of the pit that can trigger the island formation in a similar way of a buried stressor.

The general trend here discussed and, in particular the anomalous smoothing, also

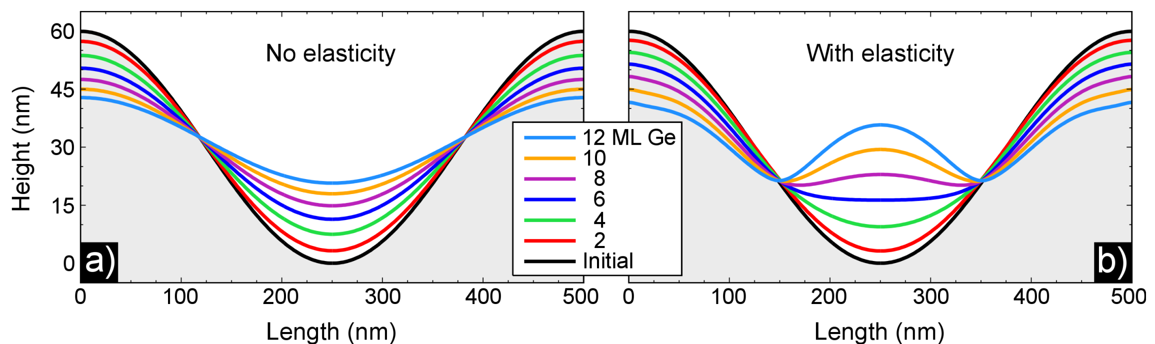

Figure 3.8: Evolution of the pit profile of *Fig. 3.6* for later stages of Ge deposition comparing the cases a) without misfit strain and b) including misfit. The gray area is the initial cosine pit profile.

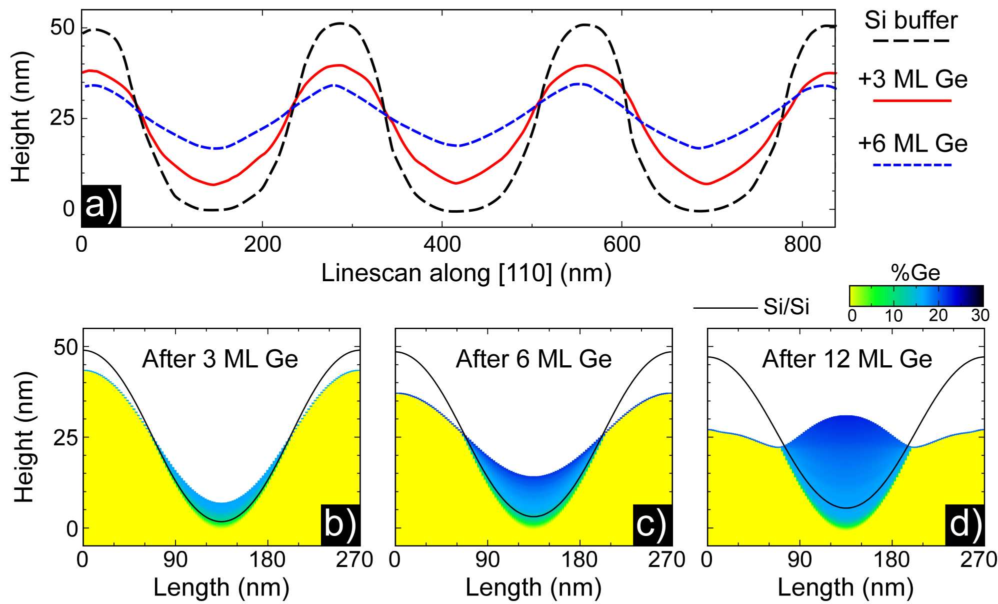

Figure 3.9: a) AFM linescan through the pit centers along [110] direction for a pattern of periodicity 270 nm for the initial Si pits and for deposition of Ge at 640°C and growth flux 0.05 Å/s. b-d) Simulation profiles and composition maps for Ge deposition on the same pattern at different growth stages (topmost layer is omitted). Initial pits are given by sinusoidal profile with 50 nm high as in experiments. For comparison, the solid line shows the profile evolution when depositing Si.

depends on the initial geometry. In particular, strong anomalous smoothing was observed experimentally also for a pattern with pitch 270 nm and pit depth 50 nm, grown at 640°C and growth flux 0.05 Å/s, as showed by the AFM linescans in *Fig. 3.9* a). Simulations adapted to the same conditions, qualitatively reproduce the experimental observations as illustrated in *Fig. 3.9* b,c). Again as few layers of Ge are deposited, a large transfer of Si is activated, leading to a composition of ∼20%. Such an effect do not occur when considering pure Si (solid line) so that again it consists of the anomalous pit filling effect. The formation of an island, at later stages, is finally expected as shown in d).

The last physical aspect that must be included in the growth model in order to have a more realistic description of Ge/Si, and other typical heteroepitaxial systems, is the faceting of the profile due to anisotropic surface energy. As discussed, in *Sect. 3.1*, a reasonable description of the anisotropy is obtained by assuming the same γ function given in eq. (3.5), that permits to reproduce {105} and {113}-like facets, corresponding to angles of 11°and 22°, respectively (here $\alpha \approx 10^-3$).

Firstly we prepare the faceted profile of the initial Si pits by performing an annealing of the very same sinusoidal profile of *Fig. 3.6* a). The resulting profile, showed in *Fig. 3.10* a), exhibit a multifaceted geometry, with both {105} and {113} facets, that closely resemble the experimental pit geometry after buffer growth, as in *Fig. 3.5*. Deposition of additional Si, as for the growth of the buffer layer, is also considered in *Fig. 3.10* a). The profile undergo a very limited smoothing and simply shifts vertically according to the growth flux. With this respect, the effect of annealing is equivalent to the growth of a buffer layer.

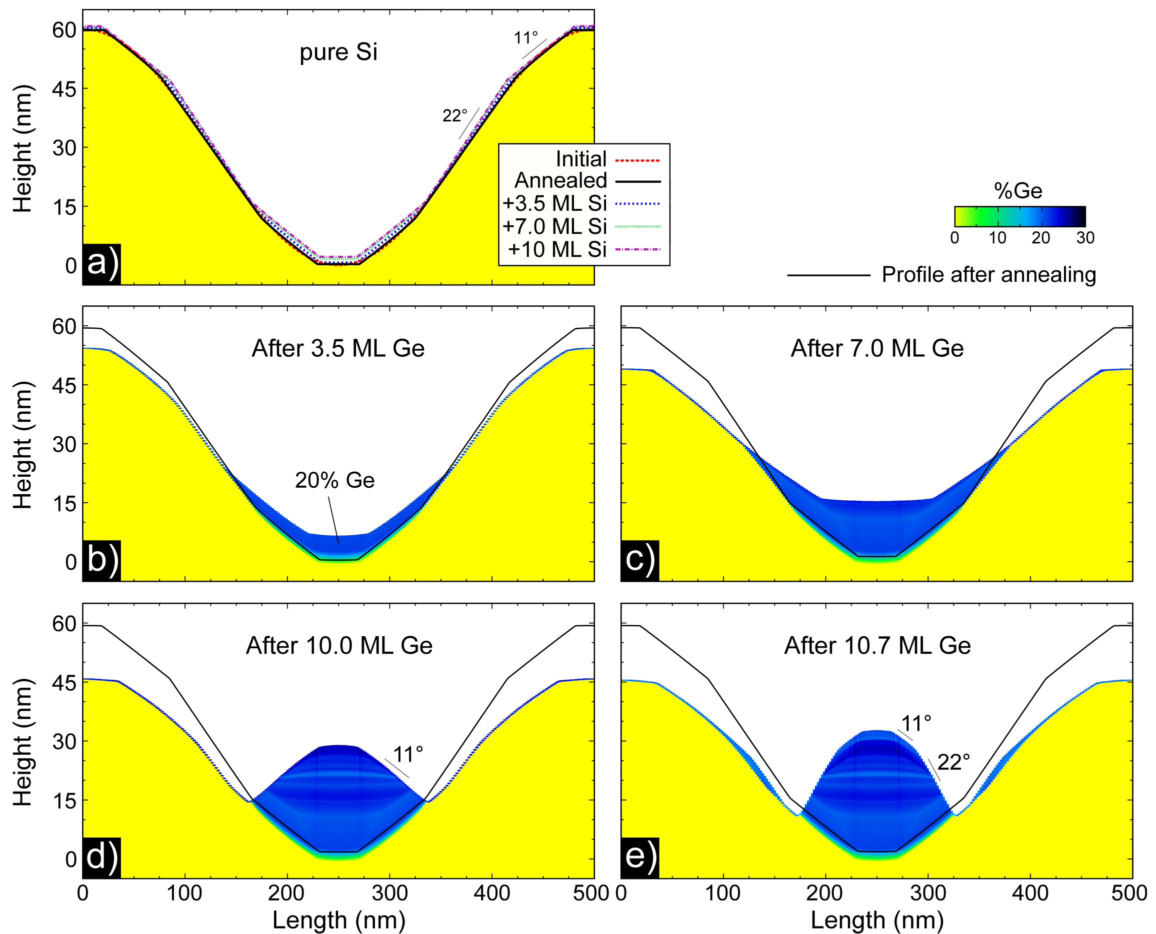

Figure 3.10: Profile evolution including crystal anisotropy. a) Evolution of a Si pit upon annealing and Si deposition. The initial sinusoidal profile is the same for the isotropic case in *Fig. 3.6*. Annealing at 720°C for 5 s gives a faceted profile that remains almost unaffected by further deposition of Si, showed for comparison with Ge deposition. b-e) Profile and composition maps at different stages of Ge deposition at 720°C (the topmost layer ∼85% rich in Ge is not shown). The reference line shows the initial pit profile obtained by annealing.

Ge is then deposited on top of the Si pits obtained after annealing. The profile evolution at different growth stages is reported in Fig. 3.10 b-d). As for the isotropic case, a substantial smoothing is again observed. The profile evolution preserve the preferential facet orientations, leading to a pyramidal pit morphology (c), bounded by only (001) and {105} facets, similar to that in experiments (Fig. 3.5). Lately, the elastic instability raises and an island grows inside the pit. Initially it consists of pyramid with {105} sidewalls (d) and subsequently a shape transition occurs leading to a dome-like geometry (e), characterized by additional {113} lateral facets. The observed trend is again in agreement with the general phenomenology observed in experiment [1, 72]. The main discrepancy is in the prediction of the island composition that in the simulations is found to be close to the 20% Ge, characterizing the region of pit filling, in contrast with recent experiments [128] showing a larger Ge content in the islands.

4

Phase-Field model

The simple Tersoff model described in *Ch. 3* proved to be effective in reproducing the main aspects of heteroepitaxial growth in the thermodynamics regime. The simplicity of the approach there proposed is surely a merit but also a point of weakness when trying to extend it to more complex situations. For example, the abrupt transition from the evolving surface region and the immobile bulk is a crude description of the actual decay of the atomic exchange probability with the distance from the surface, that could eventually depend on the growth temperature and deposition flux. Only shallow profiles are treatable. In particular, the elastic problem is based on the Flat-Island approximation, and hence lose of significance if steep morphologies are to be considered. Long time scale dynamics is completely neglected as no residual bulk diffusion is allowed, even if it can be eventually activated by defects, e.g. vacations, in some regime. Furthermore, improvements are needed also from a technical point of view. The profile in Tersoff model is given as a graph and discretized in both space and time with no optimized criteria. A table is used to store all the data concerning the composition profile in the bulk with a large consume of memory. Finally, also the extension to 3D systems, despite considered in the model formulation, is not easy to implement in practice as a much more articulated representation of the system geometry would be required to make it computationally tractable. A description by Finite Element Method (FEM), through the definition of a suitable meshing of the profile, would represent a substantial technical improvement but a lot of work should be however done in order to properly define the tracking of the surface region.

In order to overtake these limitations a redefinition of the model in a more consistent mathematical framework is needed. To this purpose, during this Thesis work, a Phase-Field model has been developed in collaboration with Prof. *A. Voigt* and his research group at the *Technische Universität Dresden (Germany)*, where most of the work here discussed was done. The advantage of this approach consists in representing the evolution of the whole system by means of an appropriate set of partial differential equations (PDE), allowing for

a simple and effective description of the profile geometry and motion. PDEs are efficiently solved by using the Finite Element Method (FEM). To the this purpose, the model has been implemented in the AMDiS [1] (Adaptive Multi-Dimensional Solver) FEM software, developed by the group of Prof. *A. Voigt* [129]. The model is derived in such a way to properly include all the main aspects characterizing the heteroepitaxial systems, i.e. the predominance of surface diffusion, the different mobility of components, the mechanism of growth by deposition and the proper energetics including surface, elastic and intermixing contributions [26].

The scope here will be mainly focused on the formulation of the model itself and simulation results will be shown to offer a proof of concepts, so that in general arbitrary parameters will are considered with no attempt to match physical systems except from a qualitative phenomenological point of view. Only 2D systems will be considered but the model formulation do not depend on the space dimension and could be straightforwardly applied to more appealing 3D problems, but the computational costs are dramatically incresed demanding for optimization (in particular, parallelization) that are beyond the present objective. The goal of this part of the Thesis is not the application of the model but its definition in a flexible enough framework, whose potential applications will be explored in a future work.

4.1 Phase-field approach

From a general point of view the description of systems containing multiple phases separated by interfaces or free surfaces can be a rather complicated task. Firstly because in many cases the interfaces themselves are not well defined as well as the corresponding phenomenology. Secondly, because their dynamics is in general very complex, as they can merge together, separate in distinct regions, form and disappear into homogeneous phases and in general move with arbitrary complex geometry. Mathematically speaking, partial differential equations (PDE) are in general used to characterize the state or evolution of this kind of systems but specific boundary conditions must be defined at each interface in order to account for the passage from one phase to the other. As the interface can change in time, free boundary problems must be considered to account for the proper system evolution but, in general, this require complex procedures to track the interface motion and control its topology.

Phase-field models [27] permit to overtake this limitations by replacing all boundary conditions with an additional partial differential equation for the evolution of an auxiliary continuum field, the phase-field φ, accounting for the distribution of the different phases and corresponding interfaces. The problem is then solved by integrating a set of partial differential equations for the whole system, thus avoiding the necessity to explicitly

[1] `http://www.amdis-fem.org`

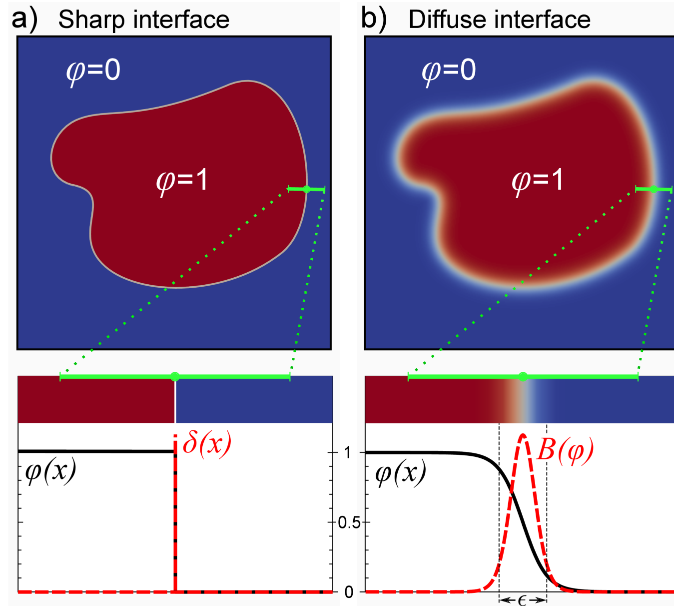

Figure 4.1: Representation of a system with two phases separated by a generic interface according to a) sharp interface and b) phase-field diffuse interface description. In a), phases are distinguished by $\varphi = \Theta$ and the interface is localized by a Dirac-δ. In b), the phase-field function φ from eq. (4.1) is considered and the interface, extending within a region of width $\sim \epsilon$, is individuated by $B(\varphi)$ (eq. (4.2)).

consider the boundary conditions at the interface between the phases.

The phase-field function plays the role of a descriptor of the system geometry but it usually has a physical meaning of order parameter distinguishing the different phases with respect to some property (e.g. order-disorder, magnetic-non magnetic, ...). The function φ is set in such a way to assume constant values into the bulk of each phase and vary smoothly between different bulk values across a thin boundary layer at their interfaces. A suitable choice for the phase-field function is:

$$\varphi(\boldsymbol{x}) = \frac{1}{2}\left[1 + \tanh\left(\frac{3}{\epsilon}|\boldsymbol{x} - \boldsymbol{x}_{0.5}|\right)\right], \tag{4.1}$$

where the interface is located at $\boldsymbol{x}_{0.5}$ and its width is given by ϵ. φ vary between 0 and 1 and is equal to 0.5 at the interface. Interfaces in the whole domain are then traced by the isoline φ=0.5. The region where the interface extends can be identified by means of a "surface delta function", given by:

$$B(\varphi) = 18\varphi^2(1-\varphi)^2 \tag{4.2}$$

In *Fig. 4.1* a comparison of the system representation according to the standard sharp interface approach (a) and the phase-field diffuse interface description (b) is showed for an arbitrary interface profile between two phases, identified respectively by φ=0 and φ=1. Clearly, in the sharp interface limit, the change from one phase to the other is abrupt so

that the function φ is an Heaviside function depending on the distance from the interface: $\varphi(x) = \Theta(x)$ for the interface at x=0. Correspondingly, the interface is localized by a Dirac-δ function. In the phase-field approach (b), the transition between the two phases is smooth as φ is given from eq. (4.1) and the surface "delta" function $B(\varphi)$ defines the interface region. φ contains all the information about the system geometry, for example, at each point along the interface the normal direction is simply the direction of $\nabla\varphi$.

As the phase-field model just represents an effective reformulation of the original PDEs, its construction must be made in such a way to guarantee the convergence of the dynamics to that defined for the sharp interface system in the limit of an infinitesimal interface width $\epsilon \to 0$ (sharp interface limit).

In the last decades, phase-field models have been successfully applied to many problems in material science, such as solidification dynamics [35, 130, 131], crystal growth [32, 132, 133], defects [134] and even used to study atomic scale processes [135, 136].

4.1.1 Finite element method

Finite Element Method (FEM) is a numerical technique allowing to find approximate solutions to PDEs over complex domains. In the following an overview of the principle of FEM is reported with no aim to be exhaustive. Much more details can be found in literature [137, 138].

The general idea of FEM consists in defining the "weak form" of the problem PDEs and then discretize them on a finite set of base functions defined on a mesh approximating the domain in the best representative way. To follow this procedure, let's consider a prototype second order PDE on a d-dimensional space:

$$-\nabla \cdot (\boldsymbol{A}\nabla u) + \boldsymbol{b} \cdot \nabla u + cu = f \qquad \text{on } \Omega \tag{4.3a}$$

$$u = g \qquad \text{on } \Gamma_D \tag{4.3b}$$

$$\boldsymbol{A}\nabla u \cdot \widehat{\boldsymbol{n}} = h \qquad \text{on } \Gamma_N \tag{4.3c}$$

where Ω is a domain in $\mathbb{R}^d$ over which the problem is defined, the solution u as well as c, f, g and h are real valued functions depending both on space and time, A is a $d \times d$ matrix and b a d-dimensional vector. Functions can eventually depend on the problem solution u itself leading to non-linearity that must be properly accounted for (e.g. by linearization in time). Boundary conditions along the domain border $\partial\Omega$ are distinguished in Dirichlet boundary conditions on $\Gamma_D \subset \partial\Omega$ with value $g : \Gamma_D \to \mathbb{R}$ and Neumann boundary conditions on $\Gamma_N = \partial\Omega \backslash \Gamma_D$, with $\widehat{\boldsymbol{n}}$ the outward unit surface normal to $\partial\Omega$.

Given the Hilbert space X restricted to those functions ϕ which satisfy the given Dirichlet boundary conditions $X := \{H^1(\Omega) : \phi = g \text{ on } \Gamma_D\}$, the weak formulation of the

problem in eqs. (4.3) consists of finding a function $u \in X$ such that

$$-\int_{\Omega} \nabla \cdot (\boldsymbol{A} \nabla u) \phi d\boldsymbol{x} + \int_{\Omega} \boldsymbol{b} \cdot \nabla u \phi d\boldsymbol{x} + \int_{\Omega} c u \phi d\boldsymbol{x} = \int_{\Omega} f \phi d\boldsymbol{x} \qquad \forall \phi \in X(\Omega) \tag{4.4}$$

The condition for the existence and uniqueness of the solution u are given by the Lax-Milgram theorem [137]. Integrating by parts the first integral can be rewritten as

$$-\int_{\Omega} \nabla \cdot (\boldsymbol{A} \nabla u) \phi d\boldsymbol{x} = \int_{\Omega} \boldsymbol{A} \nabla u \cdot \nabla \phi d\boldsymbol{x} - \int_{\partial\Omega} \boldsymbol{A} \nabla u \cdot \widehat{\boldsymbol{n}} \phi d\boldsymbol{x} \tag{4.5}$$

The boundary integral, derived by application of the divergence theorem, is zero except at the Neumann boundary Γ_N where eq. (4.3c). In the following we will not explicitly account for Neumann conditions as the derivation on such boundaries is straightforwardly restored by adding the h function in the integral on the right and side. Other boundary conditions, in particular periodic boundary conditions, can be also included.

In order to define the problem given in eq. (4.4) on a discrete space, let's consider $X_h \subset X$ the space defined by a finite set of N functions $\phi_i \in X$ forming the basis set $\Phi = \{\phi_1, \ldots, \phi_N\}$. The definition "weak-form" problem on the discretized space, named *Galerkin problem*, then consists of finding the approximation $u_h \in X_h$ of the actual solution u, such that

$$\int_{\Omega} \boldsymbol{A} \nabla u_h \cdot \nabla \phi_i d\boldsymbol{x} + \int_{\Omega} \boldsymbol{b} \cdot \nabla u_h \phi_i d\boldsymbol{x} + \int_{\Omega} c u_h \phi_i d\boldsymbol{x} = \int_{\Omega} f \phi_i d\boldsymbol{x} \qquad \forall \phi_i \in \Phi \backslash \Phi_{\Gamma_D} \tag{4.6}$$

where $\Phi_{\Gamma_D} \subset \Phi$ is the set of basis function located at the Dirichlet boundary.

As Φ is a basis for X_h The discrete solution u_h can be defined by a linear combination of basis functions:

$$u_h(\boldsymbol{x}) = \sum_{j=1}^{N} U_j \phi_j(\boldsymbol{x}) \tag{4.7}$$

with $\boldsymbol{U} = \{U_j\}_{j=1,\ldots,N} \in \mathbb{R}^N$. The same can be done for the discrete Dirichlet boundary function g_h with coefficients $\boldsymbol{G} = \{G_j\}_{j=1,\ldots,N} \in \mathbb{R}^N$. Substituting eq. (4.7) in (4.6) we obtain:

$$\sum_{j=1}^{N} U_j \left[\int_{\Omega} (\boldsymbol{A} \nabla \phi_j \cdot \nabla \phi_i) d\boldsymbol{x} + \int_{\Omega} \boldsymbol{b} \cdot \nabla \phi_j \phi_i d\boldsymbol{x} + \int_{\Omega} c \phi_j \phi_i d\boldsymbol{x} \right] = \int_{\Omega} f \phi_i d\boldsymbol{x} \qquad \forall i \in I_{\Omega} \tag{4.8a}$$

$$U_i = G_i \qquad \forall i \in I_D \tag{4.8b}$$

I_D is the set of indexes i of the basis function located on the Dirichlet boundary and I_{Ω} is set including all the others. The set of the N discrete equations here defined can be rewritten in matrix form as $\boldsymbol{MU} = \boldsymbol{F}$ and thus defines a linear system of equations that can be solved by standard numerical techniques. The result of this procedure is then the

vector $\boldsymbol{U}$ containing all the coefficients of the linear combination of the basis functions defining the approximated solution u_h to the problem as given in eq. (4.7).

The analysis here proposed for a scalar second order PDE problem apply also for a generic system of vector valued second order PDEs, leading to a more complex linear system formed by all the equations (4.8) defined for each vector component and each PDE. Higher-order PDE problems can also be solved, as they can often be reformulated as systems of second-order PDEs. [2]

Time dependent problems, where the solution u and all other functions can depend on the time variable t, can be solved as well, provided that an initial solution $u_0(x) = u(x, 0)$ is defined. Time derivatives must be discretized in time with some appropriate method (explicit-Euler scheme, Runge-Kutta method, semi-implicit scheme, . . .) [105]. Heuristic procedures can be used to dynamically define the best time step for the integration (time adaptivity).

It remains then to define the actual basis set $\Phi = \{\phi_i\}_{i=1,...,N}$ for the solution of the set of equations (4.8). In the FEM strategy [138] the actual domain is approximated by a mesh built by filling the space with basic unit elements named *simplex* (segments in 1D, triangles in 2D and tetrahedra in 3D). Local basis functions can be defined on each simplex defining a *Finite Element*. The global basis functions $\Phi = \{\phi_i\}_{i=1,...,N}$ for all Finite Elements on the mesh can be defined by means of a mapping of the local basis function with respect to a reference element. The set of all Finite Elements together with the global basis functions and the mapping from local to global basis constitutes the *Finite Element space*.

Every basis function is located at given coordinates in the element, named *nodes* of an element. A suitable choice, consists of considering lagrangian basis functions such to be equal to 1 at the node where they are located and 0 at any other node. Basis functions can be constructed by first or by higher-degree polynomials. In the case of linear Lagrange elements, the number of nodes is the same of the number $d + 1$ of vertexes defining the simplices. On the contrary, if the basis functions are of higher-degree, more nodes are defined on each simplex along the edges or in the middle of the element.

From a technical point of view the definition of an optimized mesh is crucial to obtain accuracy and numerical stability of the solution at the lowest computational cost [139]. Space adaptivity consists in the implicit definition of the mesh based on a local refinement procedure. For the phase-field case, in particular, the φ field describing the profile identifies the interface profile by its isoline at φ=0.5, where the finer grid is required while regions farther from it can be properly defined by a coarsen grid. The procedure is shown in Fig. 4.2 for a 2D mesh. A macro element is defined and its elements (triangles in 2D) are iteratively bisected according to their position with respect to the profile. In particular, at each iteration only those triangles closer to the profile are further subdivided thus

[2] For example, the fourth order equation $\nabla^2(\nabla^2 u) = f$ is equivalent to the system $\begin{cases} \nabla^2 u = w \\ \nabla^2 w = f \end{cases}$.

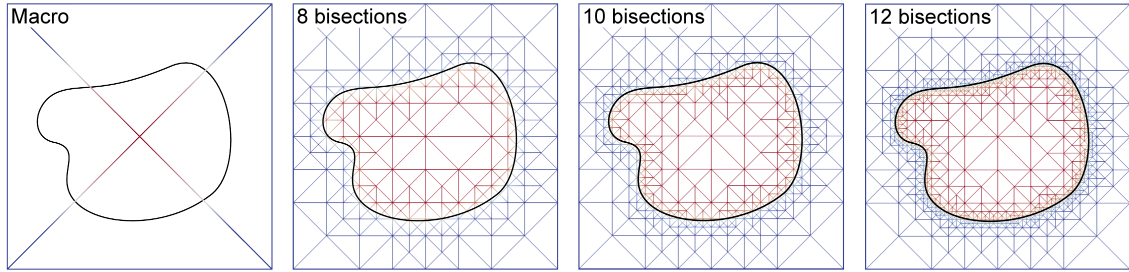

Figure 4.2: Schematic representation of space adaptivity in the definition of the implicit mesh for a phase-field profile as in *Fig. 4.1*. The initial macro element and its refinement by iteration of triangle bisection for different number of iterations is shown.

increasing the point density in the surrounding area. The more iterations are performed the better is the correspondence with the actual profile, as illustrated in *Fig. 4.2*. For time dependent problems, optimized procedures are required to identify the elements that must be refined or coarsened according to the motion of the φ field. The Finite Element toolbox AMDiS used in this work provides a flexible and powerful environment for an high-level definition of the PDE problems and allows for both space and time adaptivity.

4.2 Model definition

The thermodynamic description of the system dynamics discussed in *Ch. 2* entirely define the model from a physical point of view. We then want to transfer these description into a phase-field framework such to coherently account for the same phenomenology in diffused-interface picture. The phase-field model we are going to present is then expected to converge to the description of *Ch. 2* in the sharp interface limit.

According to the general concept of phase-field models, the evolution must be defined on the overall domain, even in the vacuum region around the solid. At variance from Tersoff model presented in *Ch. 3*, no a priori differentiation of the system regions is defined, all equations are supposed to be solved on the whole domain, including the solid bulk, the surface region and even the vacuum. Different regions (or phases) are not explicitly identified in the model but their localization is defined by means of the phase-field function φ and eventually of the different local parameters of the system, defining both local energetics and kinetics properties. φ is defined as in eq. (4.1), such to assume value 1 in the bulk and 0 in the vacuum, and smoothly vary close to the surface profile, whose location is exactly at $\varphi = 0.5$. Physically speaking, we identify the phase-field function with the material density n, opportunely normalized with respect to the bulk value n_b. For a multi-component system,

$$n_b\varphi(\boldsymbol{x}) = n(\boldsymbol{x}) = \sum_i n_i(\boldsymbol{x}) \tag{4.9}$$

where i identify the chemical species considered, whose density is n_i. A smooth decay of the material density is then assumed at the interface, following the behavior of φ.

The local material composition is defined as the atomic fraction of the i component and is then given by

$$c_i(\boldsymbol{x}) = \frac{n_i(\boldsymbol{x})}{n(\boldsymbol{x})} = \frac{n_i(\boldsymbol{x})}{n_b\varphi(\boldsymbol{x})} \tag{4.10}$$

Obviously $\sum_i c_i = 1$. In the following we will drop the index i whenever possible, implicitly referring to one component. Furthermore we assume $n_b = 1$ as it is only a numerical factor.

The state of the system is fully defined by the fields φ and c. Their evolution in time results from the local fluxes of the single components $\frac{\partial n_i}{\partial t}$:

$$\frac{\partial \varphi}{\partial t} = \frac{\partial n}{\partial t} = \sum_i \frac{\partial n_i}{\partial t} \tag{4.11a}$$

$$\varphi\frac{\partial c_i}{\partial t} = \frac{\partial n_i}{\partial t} - c_i\frac{\partial n}{\partial t} \tag{4.11b}$$

Locally, the flux of each component $\frac{\partial n_i}{\partial t}$ can be defined according to eq. (2.5) or (2.10), respectively for attachment/detachment or diffusion limited kinetics. In the following we will focus only on the latter case as it is more physically relevant; the very same arguments can however be straightforwardly applied also in the former case. Eqs. (4.11) and (2.10) are locally defined for each point $\boldsymbol{x}$ of the overall system domain, in the vacuum as well as in the solid, so that all points of the system are described by the same dynamics. The different behavior then arise only from the dependence of the fluxes on the phase-field variable (and composition). Eqs. (2.10) and (2.9) are then rewritten explicitly as:

$$\frac{\partial n_i}{\partial t}(\varphi, c) = -\nabla \cdot \boldsymbol{J}_i(\varphi, c) + \Phi_i(\varphi) \tag{4.12a}$$

$$\boldsymbol{J}_i(\varphi, c) = -M_i(\varphi, c)\nabla\mu_i(\varphi, c) \tag{4.12b}$$

where the deposition flux Φ_i is assumed to be independent of the local composition. The definition of μ_i, Φ_i and M_i as functions of the two system variables φ and c complete the model description.

4.2.1 Free energy definition and local chemical potentials

The system energetics includes all the contributions discussed in *Ch. 2*, i.e. surface and elastic energy and entropy of mixing. The starting point is the definition of the free energy functional with respect to the system variables: $G = G[\varphi, c]$.

Generally speaking, the system free energy can be defined in the form of a Ginzburg-Landau energy functional [27, 130, 140], separating the contributions in the bulk phases from gradient energy contributions accounting for the interface energy between different

phases:

$$G[\varphi, c] = \int_{\Omega} \left[g(\varphi, c) + \gamma \frac{\epsilon}{2} |\nabla \varphi|^2 + \frac{\beta}{2} |\nabla c|^2 \right] d\boldsymbol{x} \tag{4.13}$$

where g is the bulk free energy density, the $|\nabla\varphi|^2$ term accounts for the energy cost for the formation of a free surface, with γ the surface energy energy density and ϵ the interface width (see eq. (4.1)), and the $|\nabla c|^2$ term defines the energy cost related to the separation of phases at different composition, with β a proper interface energy density. In the assumption of ideal alloy, with no phase segregation, the last term can be neglected, i.e. $\beta = 0$. The integral is defined on the overall system domain Ω.

The bulk free energy includes elastic energy, given in eq. (2.30), and mixing entropy, defined in (2.66) (mixing enthalpy is zero for ideal alloy). Furthermore a double well potential $B(\varphi) = 18\varphi^2(1-\varphi)^2$, with minima at 0 and 1, must be included to stabilize the bulk and vacuum phase so that φ deviates from such values only at the interface. The bulk free energy density g is then

$$g(\varphi, c) = \rho_\varepsilon(\varphi, c) - T\varphi s(c) + \frac{\gamma}{\epsilon} B(\varphi) \tag{4.14}$$

where $\rho_\varepsilon = \rho_\varepsilon(\varphi, c)$ is the elastic energy density depending on the local system state (φ, c), T is the temperature and $s(c) = -k\left[c \ln c + (1-c)\ln(1-c)\right]$ is the mixing entropy density (k is the Boltzmann's constant). The factor γ/ϵ sets the height of the energy barrier between the bulk states at $\phi = 0$ and $\phi = 1$.

For a single component system, the free energy G (eqs. (4.13) and (4.14)) reduces to the surface energy only:

$$F_\gamma[\varphi] = \int_{\Omega} \gamma \left[\frac{1}{\epsilon} B(\varphi) + \frac{\epsilon}{2} |\nabla\varphi|^2 \right] d\boldsymbol{x} \tag{4.15}$$

Notice that the integration is on the entire domain Ω, even if the calculation is for a surface contribution. The correct restriction of the contribution at the surface only is due to the functional form of $B(\varphi)$ and $\nabla\varphi$, both assuming non-zero values only where φ is changing in the immediate proximity of the interface. If $\gamma = 1$ the integration gives the area of the surface identified by $\varphi = 0.5$. γ is then the proper surface energy density, eventually dependent on the local orientation and composition of the surface: $\gamma = \gamma(\widehat{\boldsymbol{n}}, c)$ [31, 130]. Eq. (4.15) is the phase-field equivalent of eq. (2.12) so that eq. (4.13) properly includes all physical contributions.

Once G is given, chemical potentials μ_i are obtained by definition:

$$\mu_i = \frac{\delta G}{\delta n_i} = \frac{\delta G}{\delta \varphi} + \frac{1-c_i}{\varphi} \frac{\delta G}{\delta c_i} \tag{4.16}$$

where $\frac{\partial \varphi}{\partial n_i} = 1$ and $\frac{\partial c_i}{\partial n_i} = \frac{1-c_i}{\varphi}$.

4.2.2 MBE deposition flux

The flux term Φ_i for the i-th component represents a local source term in the evolution equation (4.12a), at all points $\boldsymbol{x}$ of the system domain. Physically speaking, the only external flux for the model system is the deposition flux accounting for the transfer of material at the surface during the growth.

A generic vector flux field $\boldsymbol{\Phi}_i(\boldsymbol{x})$, defined on the overall domain, can be restricted at the surface region by means of the surface delta function $B(\varphi)$. The resulting vector field can be considered the phase-field equivalent of the growth flux on the profile. The local material transfer $\Phi_i(\boldsymbol{x})$ is then given by the projection of the restricted field along the direction of the local surface normal $\widehat{\boldsymbol{n}}(\boldsymbol{x}) = \frac{\nabla\varphi}{|\nabla\varphi|}$:

$$\Phi_i = B(\varphi)\boldsymbol{\Phi}_i \cdot \widehat{\boldsymbol{n}} = B(\varphi)\boldsymbol{\Phi}_i \cdot \frac{\nabla\varphi}{|\nabla\varphi|}. \tag{4.17}$$

The field $\boldsymbol{\Phi}_i$ is defined in such a way that its restriction at the surface, i.e. at φ=0.5, equals the prescribed deposition flux. In the simple case of MBE deposition, the flux impinging along the surface is uniform and aligned along the source-sample direction, i.e. the vertical direction $\widehat{\boldsymbol{z}}$. A uniform flux field is best suited for this conditions: $\boldsymbol{\Phi}_i = -\Phi_{0,i}\widehat{\boldsymbol{z}}$.

Notice that $B(\varphi)$ keeps track of the surface motion during the growth process so that the restriction of the flux field is always localized along the profile.

4.2.3 Local mobility: surface vs. bulk dynamics

The definition of the local mobility with respect to the variables φ and c permits to characterize the kinetics of the transport of atoms at each point $\boldsymbol{x}$ of the system. As in Tersoff model (see eq. (3.15)), the mobility constant M_i can considered to depend both on the intrinsic properties of the atomic motion, accounted by a diffusion coefficient D_i, and on the abundance of such mobile species $n_i = c_i n$:

$$M_i = D_i n_i = D_i c_i \varphi \tag{4.18}$$

By means of this definition the all dynamics is completely restricted in the region of the solid as $M_i \approx 0$ in the vacuum region, where $\varphi \approx 0$.

Further details on the system kinetics can be included in the definition of the diffusion coefficient that is itself defined as a local quantity $D_i = D_i(\varphi, c)$. In particular, as argued in the definition of Tersoff model (*Sect. 3.1*), it is well known that the atomic motion of atoms at surface is much faster than in the bulk. In order to account for this important aspect, a distinction between a surface diffusion coefficient $D_{s,i}$ and the residual bulk diffusion value D_b should be considered in the definition of D_i:

$$D_i(\varphi) = D_{s,i} f(\varphi) + D_b \tag{4.19}$$

where the function f is defined in such a way to localize the surface region. Actually, the motion in the bulk can be quite complex, involving defects (e.g. vacancies) or simultaneous exchange mechanisms, but, for the sake of simplicity, here we assume just a constant, small, value of D_b.

A simple choice for f can be the $B(\varphi)$ function itself:

$$D_i = D_{s,i}B(\varphi) + D_b \tag{4.20}$$

This way, the surface contribution is effective only in the close proximity of the surface profile, at $\varphi = 0.5$, within the interface width ϵ, as indicated in *Fig. 4.3* a). More precisely, the mobility function is asymmetrical and decays faster on the vacuum side. At larger distances, only bulk diffusion is effective $M_b = D_b\varphi$ so that mobility fall to the bulk diffusion value D_b in the solid and to 0 in the vacuum. In *Fig. 4.3* b) the map of the mobility field for a sinusoidal surface profile profile is reported, indicating the localization of the surface diffusion in the close proximity of the profile.

The special case $D_b = 0$ is the phase-field description of pure surface diffusion [5, 28].

A more realistic approach should eventually account for the gradual reduction of the efficiency of atomic exchanges when moving below the surface. Such an effect can be included as:

$$D_i(\boldsymbol{x}) = D_{s,i}\exp\left(-\frac{d(\boldsymbol{x})}{w}\right) + D_b, \tag{4.21}$$

where w is the decay length of the surface diffusivity and $d(\boldsymbol{x}) = |\boldsymbol{x} - \boldsymbol{x}(\varphi = 0.5)|$ is the distance of the point x from the surface profile. Results discussed in the following are based on the simpler eq. (4.20) but similar results were found also with (4.21).

As addressed by the index i, different diffusion coefficients are expected for different chemical species (e.g. $D_{\mathrm{Ge}} > D_{\mathrm{Si}}$) and eventually they can also depend on the local environment, so that $D_i = D_i(\varphi, c)$, as argued in *Sect. 3.1.4*.

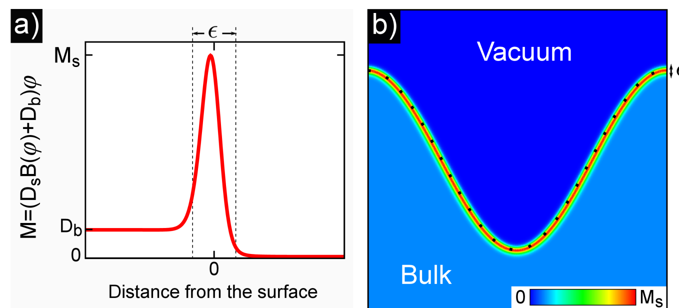

Figure 4.3: Mobility function defined according to eqs. (4.18) and (4.20) for the case $D_s \gg D_b$. a) Plot of the mobility as a function of the distance from the surface. In the vacuum region $M = 0$ while in the bulk $M = D_b$. In the proximity of the surface, the mobility is enhanced up to a maximum value M_s. b) Map of the mobility field on the overall domain, for a sinusoidal surface profile (dotted).

4.3 Single component system: mean curvature flow

For a single component system the only energetic contribution is represented by the surface energy given in eq. (4.15). As only one species is present, the chemical potential coincide with the variation of the free energy with respect to the phase-field variable φ itself:

$$\mu_\gamma = \frac{\delta F_\gamma}{\delta \varphi} = \epsilon \nabla \cdot (\gamma \nabla \varphi) - \nabla \cdot (\mathcal{S} \nabla_{\widehat{\boldsymbol{n}}} \gamma) + \frac{\gamma}{\epsilon} B'(\varphi) \tag{4.22}$$

where $\mathcal{S} = \frac{1}{\epsilon} B(\varphi) + \frac{\epsilon}{2} |\nabla \varphi|^2$, $B'(\varphi) = \frac{\partial B}{\partial \varphi}$ and the operator $\nabla_{\widehat{\boldsymbol{n}}}$ indicates that the gradient is to be evaluated with respect to the components of the surface normal vector $\widehat{\boldsymbol{n}} = \frac{\nabla \varphi}{|\varphi|}$.

By restricting the system dynamics to surface diffusion by means of the mobility function $M = DB(\varphi)$, and substituting into eqs.(4.12) and then in (4.11), a second-order PDE system is defined:

$$\frac{\partial \varphi}{\partial t} = D \nabla \cdot B(\varphi) \nabla \mu_\gamma + \Phi \tag{4.23a}$$

$$\mu_\gamma = \epsilon \nabla \cdot (\gamma \nabla \varphi) - \nabla \cdot (\mathcal{S} \nabla_{\widehat{\boldsymbol{n}}} \gamma) + \frac{\gamma}{\epsilon} B'(\varphi), \tag{4.23b}$$

where a growth flux Φ is included. Notice that the actual problem is fourth order in φ.

The time derivative is discretized as $\frac{\partial \varphi}{\partial t} = \frac{\varphi^{m+1} - \varphi^m}{\tau^m}$, where τ^m is the time step and the evolution is from time t^m to $t^{m+1} = t^m + \tau^m$ and the weak-form of eqs. (4.23) is defined, in a semi-implicit scheme, in order to make them solvable numerically in AMDiS:

$$\int_\Omega \frac{\varphi^{m+1} - \varphi^m}{\tau^m} \phi d\boldsymbol{x} = -D \int_\Omega B(\varphi^m) \nabla \mu_\gamma^{m+1} \cdot \nabla \phi d\boldsymbol{x} + \int_\Omega \Phi \phi d\boldsymbol{x} \tag{4.24a}$$

$$\begin{aligned} \int_\Omega \mu_\gamma^{m+1} \phi d\boldsymbol{x} = &- \int_\Omega \varepsilon \gamma(\widehat{\boldsymbol{n}}^m) \nabla \varphi^{m+1} \cdot \nabla \phi d\boldsymbol{x} + \int_\Omega \mathcal{S}^m \nabla_{\widehat{\boldsymbol{n}}} \gamma(\widehat{\boldsymbol{n}}^m) \cdot \nabla \phi d\boldsymbol{x} + \\ &+ \int_\Omega \frac{1}{\epsilon} \gamma(\widehat{\boldsymbol{n}}^m) B''(\varphi^m) \varphi^{m+1} \phi d\boldsymbol{x} + \int_\Omega \frac{1}{\epsilon} \gamma(\widehat{\boldsymbol{n}}^m) \left[B'(\varphi^m) - B''(\varphi^m) \varphi^m \right] \phi d\boldsymbol{x} \end{aligned} \tag{4.24b}$$

where ϕ is the test function and $B''(\varphi) = \frac{\partial^2 B}{\partial \varphi^2}$. In the discretization the $B'(\varphi)$ function has been linearized in time in order to permit to evaluate its contribution semi-implicitly: $B'(\varphi^{m+1}) = B'(\varphi^m) + \frac{\partial B'}{\partial \varphi}|_{\varphi^m} (\varphi^{m+1} - \varphi^m)$.

By considering an isotropic system with a constant γ, independent of the surface orientation, the system evolution is simply defined by

$$\frac{\partial \varphi}{\partial t} = D \nabla \cdot [B(\varphi) \nabla \varphi] + \Phi \tag{4.25a}$$

$$\mu_\gamma = \gamma \left[\nabla^2 \varphi + \frac{1}{\epsilon} B'(\varphi) \right] \tag{4.25b}$$

This problem is the well known *Cahn-Hilliard* equation for mean-curvature flow in phase-

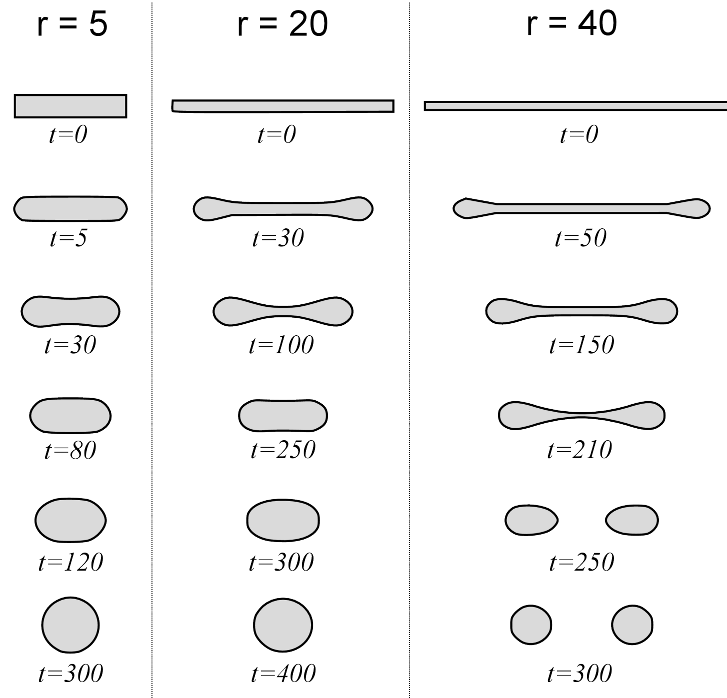

Figure 4.4: Phase-field simulations of the evolution by mean-curvature flow (eq. (4.25)) for an initial rectangular shape, for three different values of the ratio r between its dimensions. Time scale is in $D\gamma$ units. Profiles are defined by the isoline φ=0.5 and the outer region φ <0.5 is cut away.

field [5], converging to to the sharp interface limit $v = D\gamma\nabla_S^2\kappa$, with v the normal velocity and κ the local curvature (as considered in *Sect. 3.3.1*).

In *Fig. 4.4* an example of the evolution by mean-curvature flow is reported for a rectangular bar. Different ratio r between the two dimensions of the initial rectangular shape are considered. At the beginning, the bar evolution is dominated by the smoothing at vertexes, where curvature is maximum, and the two extremes of the bar tend gradually to round. As these regions grow larger, the middle of the bar, that initially is flat and do not evolve, gets curved and tends to narrow leading to a necking. At this point, if the two rounded regions are close enough, i.e. if the initial size r is not too large, the domain remains connected and they coalesce in the middle region leading a single circular shape corresponding to the absolute minimum of surface energy, as the exposed surface is the smallest possible for the profile area considered. On the contrary, if the rounded regions are too large as for the largest value of $r = 40$ here considered, a pinch-off is observed and the initial profiles separates in two distinct region, not connected one with each, leading in the end to two circles corresponding to a relative minimum for the surface energy, at higher energy compared with the single circle observed in the other cases as the exposed surface is larger. This latter behavior shows that the system evolution, even if driven by the thermodynamic tendency to free energy minimization, can lead to morphologies that do not correspond to the thermodynamic limit. Furthermore, it is important to address that

the evolution here considered, involving a self-intersecting profile at pinch-off is naturally described in the the phase-field approach, at variance from sharp-interface model that would require specific and complicated procedure to handle these events.

When considering crystalline structures, the existence of preferential facet orientations should be accounted for, thus implying surface anisotropy $\gamma = \gamma(\widehat{\boldsymbol{n}})$. All terms in eq. (4.23) must be considered [5, 31, 32, 130]. As discussed in *Sect. 2.2.1*, the numerical stability of the anisotropic problem depends on the strength of the anisotropy as given by the functional form of $\gamma(\widehat{\boldsymbol{n}})$. In the case of strong anisotropy, the eqs. (4.23) are ill-posed for unstable orientations and hence a regularization term is needed [5, 29]. This can be done by means of *Willmore* regularization, that consists of a phase-field equivalent of the corner rounding term $F \propto \kappa^2$ introduced in *Sect. 2.2.1* [100]. In particular, an additional contribution is included in the surface free energy definition:

$$F_W = F_\gamma + \frac{\alpha^2}{2\epsilon}\int_\Omega \left[-\epsilon\Delta\varphi + \frac{1}{\epsilon}B'(\varphi)\right]^2 d\boldsymbol{x} \tag{4.26}$$

where α is an isotropic “corner energy”. Calculating the variational derivative with respect to φ we then obtain a correction to the chemical potential μ_γ:

$$\mu_W = \mu_\gamma + \alpha^2\left(-\Delta\omega + \frac{1}{\epsilon^2}B''(\varphi)\omega\right) \tag{4.27a}$$

$$\omega = -\epsilon\Delta\varphi + \frac{1}{\epsilon}B'(\varphi) \tag{4.27b}$$

The result is a sixth-order problem in φ that is rendered in a system of three PDEs.

An example of profile evolution including strong anisotropic surface energy is shown in *Fig. 4.5* b) for the more complex problem with two components.

4.4 Two components system: mixing entropy

Let's consider a two component system, more precisely an ideal (unstrained) alloy. In this case, the total free energy includes both surface energy, given in eq. (4.15), and entropy of mixing dependent on the local composition, defined by a density $s(c) = -k\sum_i c_i \ln c_i$ (eq. (4.14)).

In the assumption that γ do not depend on the local composition, the surface energy contribution to the chemical potential (μ_γ) is the same for all chemical species and is given by eq. (4.22). Local chemical potential μ_i than differs from one species to the other just because of the entropic term:

$$\mu_i = \mu_\gamma + kT\ln c_i \tag{4.28}$$

According to the definition in eq. (4.12b), the current flow for each component is

determined by the gradients of both system variables:

$$\boldsymbol{J}_i = -D_i c_i \varphi \nabla \mu_\gamma - kTD_i \varphi \nabla c_i \tag{4.29}$$

$\nabla\varphi$ accounts for the transport related to the motion of the profile while ∇c_i define the redistribution of each component according to Fick's law. The evolution equations are derived after substitution of eq. (4.29) into (4.12a):

$$\frac{\partial \varphi}{\partial t} = \nabla \cdot (D(c)\varphi \nabla \mu_\gamma) + kT\nabla \cdot (\delta_D \varphi \nabla c) + \Phi \tag{4.30a}$$

$$\varphi \frac{\partial c}{\partial t} = \nabla \cdot (D_1 c \varphi \nabla \mu_\gamma) + kT\nabla \cdot (D_1 \varphi \nabla c) + \Phi_1 - c\frac{\partial \varphi}{\partial t} \;{}^{3}, \tag{4.30b}$$

where we consider the composition with respect to the first component $c = c_1$. $D(c) = \sum_i D_i c_i$ is the net diffusivity for the two components and $\delta_D = D_1 - D_2$. $\Phi = \sum_i \Phi_i$. Eqs. (4.30) together with the chemical potential μ_γ defined in eq. (4.22) fully describe the system dynamics forming a set of three PDEs, fourth order in φ and second order in c.

Time discretization is obtained setting $\frac{\partial \varphi}{\partial t} = \frac{\varphi^{m+1}-\varphi^m}{\tau^m}$ and $\frac{\partial c}{\partial t} = \frac{c^{m+1}-c^m}{\tau^m}$, where τ^m is the time step and the evolution is from time t^m to $t^{m+1} = t^m + \tau^m$. The weak formulation of eqs. (4.30), in a semi-implicit scheme for time integration, is given by

$$\int_\Omega \frac{\varphi^{m+1}-\varphi^m}{\tau^m}\phi d\boldsymbol{x} = -\int_\Omega D(c^m)\nabla \mu_\gamma^{m+1}\cdot \nabla \phi d\boldsymbol{x} - kT\int_\Omega \delta_D \varphi^m \nabla c^{m+1}\cdot \nabla\phi d\boldsymbol{x} + \int_\Omega \Phi \phi d\boldsymbol{x} \tag{4.31a}$$

$$\begin{aligned}\int_\Omega \varphi^m \frac{c^{m+1}-c^m}{\tau^m}\phi d\boldsymbol{x} = &-\int_\Omega D_1 c^m \varphi^m \nabla \mu_\gamma^{m+1} \nabla \phi d\boldsymbol{x} - kT\int_\Omega D_1 \varphi^m \nabla c^{m+1}\nabla \phi d\boldsymbol{x} + \\ &+\int_\Omega \Phi_1 \phi d\boldsymbol{x} - \int_\Omega c^m \frac{\varphi^{m+1}-\varphi^m}{\tau^m}\phi d\boldsymbol{x}\end{aligned} \tag{4.31b}$$

The last equation for μ_γ is the same of (4.24b).

Let's consider first the simple case of equal diffusion coefficients, $D_1 = D_2 = D$ ($\delta_D = 0$). In this case the eq. (4.30) reduces to:

$$\frac{\partial \varphi}{\partial t} = \nabla \cdot (D\varphi \nabla \mu_\gamma) + \Phi \tag{4.32a}$$

$$\varphi \frac{\partial c}{\partial t} = D\varphi \nabla c \cdot \nabla \mu_\gamma + kT\nabla \cdot (D\varphi \nabla c) + \Phi_1, \tag{4.32b}$$

The evolution equation (4.32a) for the surface profile φ is analog to the *Cahn-Hilliard* equation given in eq. (4.25) (for isotropic γ). The same chemical potential μ_γ drives the evolution, while the mobility is different since in our model it is proportional to φ, i.e. to the material density. This is due to the assumption that transport currents evolves according to the fluxes of the components ($M_i \propto n_i$). This leads to an asymmetry in the

[3] For reasons of numerical stability a term $d\nabla^2 c$ for $d \to 0$ (i.e. $\sim 10^{-6}$) is included.

phases, as fluxes outside of the bulk are suppressed by φ=0. As a consequence, separated domains of material do not coarsen, but voids in the bulk phase do.

The evolution of the concentration field c given from eq. (4.32b) is easily interpreted as a diffusion equation on a domain evolving in time according to the φ field [28, 141]. In particular, assuming φ within a stationary state, that is $\nabla\mu_\gamma = 0$, eq. (4.32b) reduces to the usual Fick diffusion equation $\frac{\partial c}{\partial t} \sim \nabla^2 c$ with an external flux Φ_1. The term $D\varphi\nabla c \cdot \nabla\mu_\gamma$ in eq. (4.32b) can then be identified as responsible for the material transfer related to the evolution of the profile.

In *Fig. 4.5* the coupled evolution of surface and composition profiles is shown for a substrate of component 1 subject to deposition of component 2. In the last snapshot (at time=3) the exact amount of material required to fill the pit is deposited. Only surface diffusion is considered $M \sim B(\varphi)\varphi$ ($D_b = 0$) so that the deposited material can mix only within the interface region of width $\sim \epsilon$. In *Fig. 4.5* a) isotropic γ is considered and the profile is found to evolve smoothly toward complete flattening (see *Fig. 3.4* for comparison). During the process, the composition at the surface gradually tends to the pure component 2 deposited. Since the process occurs simultaneously to the profile smoothing, portions of the raised regions of the substrate are eroded and the corresponding material of species 1 is transferred into the bottom region where it mixes with the deposited

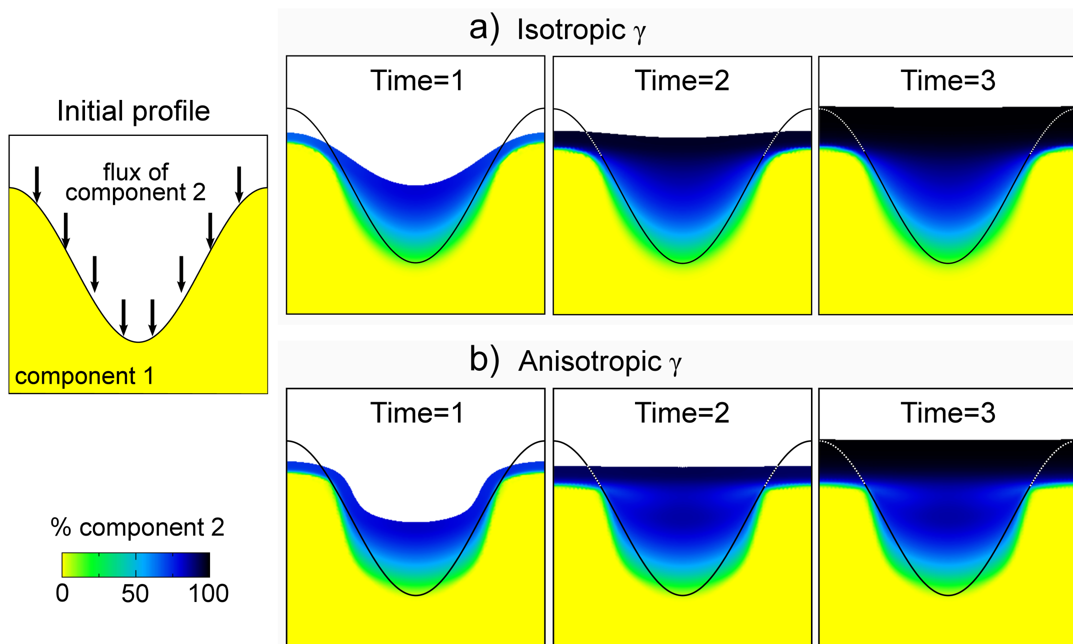

Figure 4.5: Phase-field simulation of the evolution of a substrate of component 1 with sinusoidal surface profile during growth with an external flux of component 2. Pure surface diffusion is assumed with $D_1 = D_2$. Strain effects are not included. Simulations are performed for both isotropic surface energy γ=1 a) and strong anisotropy, $\gamma = 1 - 0.1\cos(4\theta)$ b). Only the crystal region ($\varphi < 0.5$) is shown and the solid line indicates the initial profile as reference. All parameters are given in arbitrary units.

component 2. Since no bulk diffusion is allowed, the composition profile resulting from this mechanism is frozen-in when the surface grows far. Notice, that this is a purely kinetic effect since thermodynamics would drive the system to homogeneous composition. This behavior would be restored by admitting some bulk diffusion.

In *Fig. 4.5* b), anisotropic surface energy is considered. In particular, in the present 2D case, $\gamma = \gamma(\theta)$, where $\theta = -\arctan\left(\frac{\nabla\varphi_y}{\nabla\varphi_x}\right)$ is the local orientation of the surface. More specifically, a function $\gamma = 1 - 0.1\cos(4\theta)$ is used, favoring the formation of 90°angles. For such a function, strong anisotropy holds and hence Willmore regularization was included according to eqs. (4.27a). Profiles in *Fig. 4.5* b) show a qualitative behavior similar to the isotropic case except for the profile morphology that looks more squared as the surface tends to align along the stable horizontal and vertical directions.

According to eq. (4.32b), in the absence of external fluxes, an homogeneous system at uniform composition c is not expected to undergo any evolution in its composition profile just behaving as a single component system, according to eq. (4.32a). This is direct consequence of the assumption of equal mobility for both components since this imply that all transport processes throughout the system imply the motion of material at the very same composition c. On the contrary, if diffusion coefficients are different, composition variations can occur even for an homogeneous system [22]. This happens because the flux of the fastest species is not compensated by the flux of the slowest one thus producing a change in composition dominated by the transfer of the first one, properly accounted for by (4.30). Furthermore material transport can arise from this unbalance as given by the term $\nabla \cdot [\delta_D \nabla c]$ in eq. (4.30a).

In *Fig. 4.6* the evolution of a sinusoidal profile of a 50-50 alloy is shown when considering a difference of a factor ten in the surface diffusion coefficients of the two components ($D_{2,s} = 10D_{1,s}$), as given in eq. (4.18). During the smoothing of the profile, the fastest species tends to accumulate in the pit bottom while the slowest one is left behind. This is very effective in the initial stages and gradually decreases as the process continue since the a larger amount of the slowest species remains at the surface while the fastest is buried in the bulk. Notice that the origin of the observed composition separation is fully kinetic. Simulations in Fig. 4.6 also include bulk diffusion, however assumed to be slower than surface diffusion D_b=$10^{-2}D_{s,2}$. The effect is limited during the profile evolution as the process is dominated by the fastest dynamics at the surface. A smearing of the composition gradients is observed so that the separation of components is mitigated. The role of bulk diffusion becomes more evident on a longer time scale, after complete flattening of the profile, driving the system toward the equilibrium homogeneous state for the whole bulk.

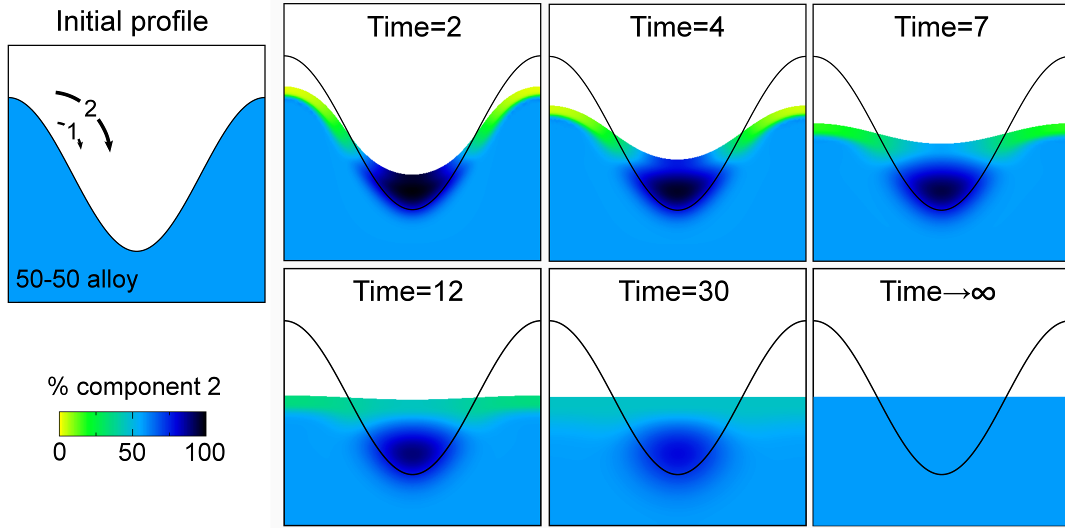

Figure 4.6: Evolution of the profile in Fig.4.1 for a 50-50 alloy in the absence of external flux, when accounting for different surface diffusion constants between the two components $D_{2,s} = 10D_{1,s}$, as in eq. (4.18)). Slow diffusion in the bulk is also included by setting $D_b = 10^{-2}D_{1,s}$. The solid line reports the initial profile as reference.

4.5 Elasticity via Phase-Field

4.5.1 Static mechanical equilibrium

In the context of phase-field method, the solution of the elastic problem given by eq. (2.41) can be straightforwardly solved by defining the dependence of the elastic parameters on the phase-field function itself, on the overall system domain [32].

In the assumption of isotropic media we define $\mu = \mu(\varphi)$, $\lambda = \lambda(\varphi)$ and $\epsilon^\star = \epsilon^\star(\varphi)$ such that in the bulk of each phase p they converge to the intrinsic properties $(\mu, \lambda, \epsilon^\star) \rightarrow (\mu_p, \lambda_p, \epsilon^\star_p)$ while at the interfaces they change smoothly from those of one phase to the other. For the case of our interest, of a solid phase in vacuum, a smooth modulation function $f(\varphi)$ tending to 1 in the solid and 0 in the vacuum ensure a treatable variation of the elastic properties moving from the bulk to the vacuum, assimilated to a second phase with unable to sustain any stress, i.e. μ, λ=0. The phase-field function itself (eq. (4.1)) can be considered as modulation function f, so that:

$$\mu(\varphi, c) = \varphi\mu(c)^4 \qquad \lambda(\varphi, c) = \varphi\lambda(c) \qquad \epsilon^\star(\varphi, c) = \varphi\epsilon^\star(c) \tag{4.33}$$

The elastic state of the system can then be defined by considering the equilibrium condition in eq. (2.45) for the overall domain:

$$\nabla \cdot [\mu(\varphi, c)\,(\nabla \otimes \boldsymbol{u} + \boldsymbol{u} \otimes \nabla)] + \nabla\,[\lambda(\varphi, c)\nabla \cdot \boldsymbol{u}] = \nabla\,[(2\mu(\varphi, c) + 3\lambda(\varphi, c))\,\varepsilon^\star(\varphi, c)] \tag{4.34}$$

[4] For numerical reasons a non-zero value is always required for μ. A small tolerance (μ_v ~10^{-6}) is added: $\mu = \varphi\mu(c) + \mu_v$.

The displacement field $\boldsymbol{u}(\boldsymbol{x})$, solution of eq. (4.34), permits to determine strain, stress and elastic energy through eqs. (2.22), (2.23) and (2.31), with the same parameters defined above. In *Fig. 4.7* an example of the calculation of the displacement field and strain components is reported for the simple geometry illustrated in a). Results are in good agreement with FEM calculations based on the standard solution of eq. (2.45) with no flux boundary condition along the profile.

4.5.2 Elasticity in a solid defined by phase-field

The solution of the phase-field equation (4.34) for the mechanical equilibrium then permits to exactly define the elastic state of a system defined by the variables φ and c in static conditions. When considering a system evolving in time, in principle, the equilibrium equation should be solved simultaneously to the evolution equations for φ and c, but this is clearly a substantial complication of the problem. As already argued in *Sect. 3.1.1*, it is a good approximation to consider the equilibration process instantaneous so that the system evolution, described in eqs. (4.11), can be solved with respect to the equilibrium strain state at each time [32]. More specifically, the elastic energy contribution ρ_ε, entering in the chemical potential definition (eq. (4.16)), can be calculated for the strain $\boldsymbol{\varepsilon}_{\text{eq}}$, solution of the elastic static problem in eq. (4.34) for the given system state defined by φ and c:

$$\rho(\varphi, c) = \rho(\varphi, c; \boldsymbol{\varepsilon}_{\text{eq}}(\varphi, c)) \tag{4.35}$$

Fig. 4.8 reports an example of such coupled evolution. In particular, in a) a strained film of unlimited thickness is shown to evolve toward the formation of islands as the

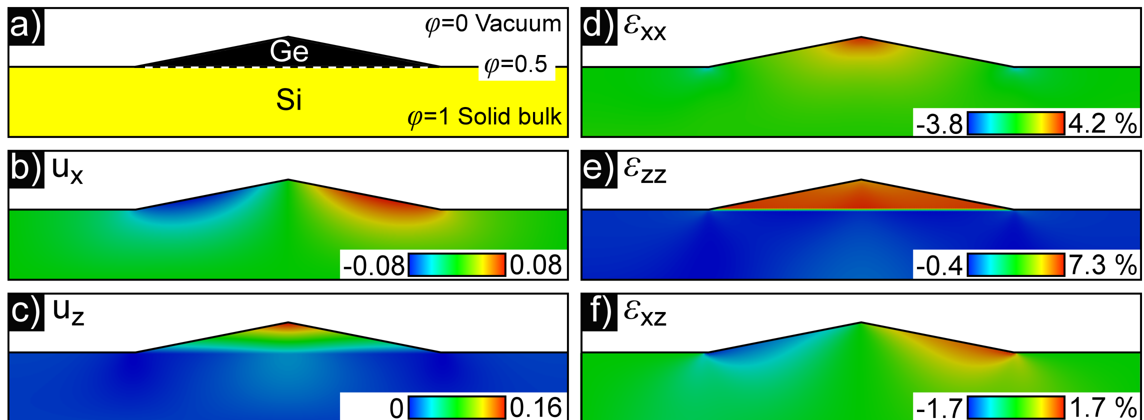

Figure 4.7: Solution of the elastic problem by means of the phase-field description as given in eq. (4.34), for the profile shown in a) of a Ge island on Si substrate (infinite in the direction perpendicular to the paper plane); the overall system domain including the vacuum phase is given by the box. b-c) displacement field map for the x and z components respectively. d-f) strain maps for the three independent components ε_{xx}, ε_{zz} and ε_{xz} respectively are shown. Notice that strain values are determined from displacements and hence do not include the eigenstrain (~-4% inside the island). Profiles are cut at the surface isoline $\varphi = 0.5$

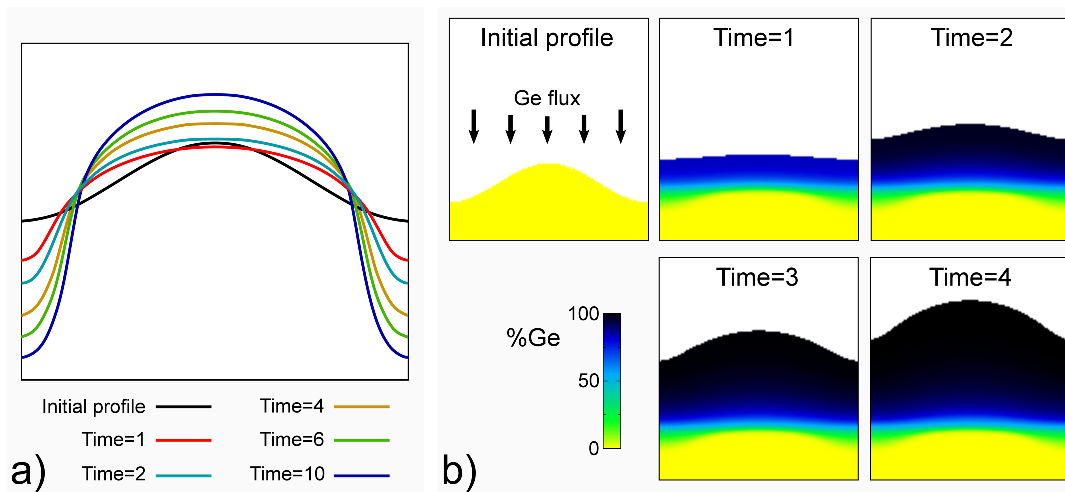

Figure 4.8: a) Surface profile evolution at different times for a strained film of unlimited thickness, with an initial sinusoidal profile. b) Simulation of profile and composition evolution during heteroepitaxial growth of a SiGe-like alloy, by deposition of Ge onto a Si substrate, with initial sinusoidal profile as in a). Island formation is observed to reduce the strain accumulation. Parameters are set arbitrarily as well as system size and time units. In particular the diffusion coefficient is the same for both components and set $\propto B(\varphi)$. Bulk diffusion is neglected.

process allows to release strain with respect to the a flat geometry. An initial sinusoidal profile is assumed in order to trigger the unstable behavior. The first stages of the growth are conceptually equivalent to the raise of ATG instability, discussed in *Sect. 2.3.4*, but the profile evolution deviates from a proper sinusoid as the exact elastic field is calculated during the simulation. In particular, the profile evolution is determined by the tradeoff between surface energy, opposing to the increase of aspect-ratio and elastic energy, favoring the pile-up of material to release more strain. The result is the rounded geometry observed, digging deeper and deeper trenches on the borders of the island.

When considering heteroepitaxial growth, e.g. Ge deposition on Si, the morphological evolution depends on the strain accumulation during the deposition process. This conditions are reproduced in *Fig. 4.8* b) where an initial substrate of pure Si is subjected to a Ge flux. At the beginning, the dominating term is surface energy, favoring the flattening of the initial profile. The small amount of Ge deposited in these first stages intermixes with the substrate Si atoms while the surface gets rich in Ge. Correspondingly, strain is accumulated and, after an appropriate deposition thickness, the flat profile becomes unstable and tends to form islands in a similar way as observed in a).

5

Modeling of self-assembly of micrometric crystal arrays on deeply patterned substrates

The growth of thick films for heteroepitaxial systems is highly desirable for devices such as detectors, power transistors, multiple-junction solar cells, ... [142]. This apparently simple task is not easy to achieve since the direct growth of one species on top of the other usually leads to poor quality devices incompatible with the strict technological requirements for applications. Two main problems reduce the material quality. The first one is the generation of misfit dislocations at the interface, formed to release the misfit strain ($\sim$4% for Ge/Si or GaAs/Si) by means of plastic relaxation, propagating up to the surface with detrimental effects on the device performance. The second is the bowing of the film and the formation of cracks during the process of cooling down from the growth temperature, caused by the thermal strain due to the different expansion coefficients of the coupled materials ($\sim$130% for Ge/Si or GaAs/Si). Despite the number of different methods proposed in literature, such as growth of graded layers [142], selective area deposition [143], thermal treatments [59, 144], ..., a definitive solution to these problems is still the subject of investigation.

By a joint collaboration between the group of Prof. *L. Miglio* (*University of Milano-Bicocca*), where the work of this Thesis was done, that of Prof. *H. von Känel* (*ETH Zürich*), that of Dr. *G. Isella* (*Politecnico di Milano*) and that of Prof. *S. Sanguinetti* (*University of Milano-Bicocca*), we recently demonstrated [2, 38] that a suitable pattern of pillars can be optimal to grow high quality heteroepitaxial crystals of micrometer size, not affected by the troubles discussed above (similar systems can also be found in Refs. [78, 145, 146]). The initial pattern of pillars is prepared by deep micromachining of the (Si) substrate by reactive ion etching and then the other component (Ge, GaAs, ...) is deposited for

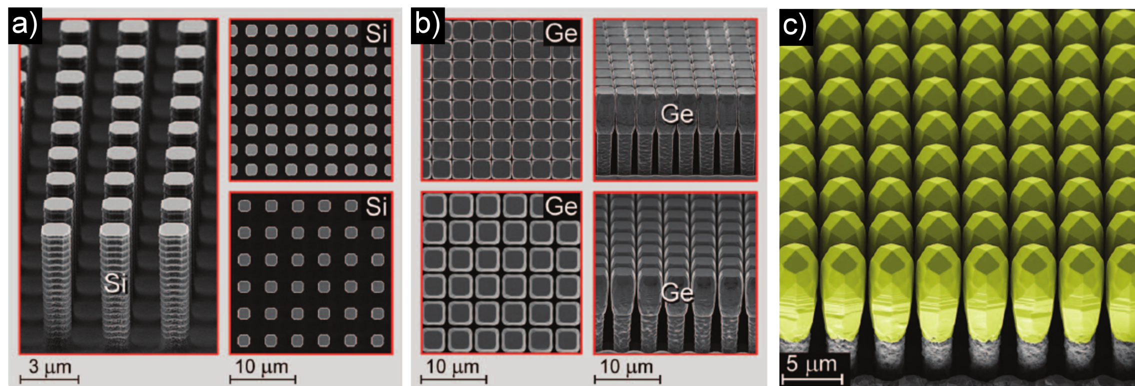

Figure 5.1: SEM micrograph of a Si pillar patterned substrate a) and of the array of Ge crystals grown on top of such substrate after 8 µm Ge deposition b). A perspective view of the crystal array is shown in c) where Ge is marked in yellow. The growth was performed in a LEPECVD reactor at 560°C. Pictures are taken from Ref. [2].

large thicknesses. The result, as shown for example in Fig. 5.1, is a space-filling array of 3D crystals, each one growing up to height of tens of µm while remaining a distinct unit by lateral self-alignment. This permits to obtain an almost full-tessellation of the space producing a film-like structure with units large some µm and separated by ∼50 nm. This way a proper base for a device is realized avoiding the problems of thermal strain that occur for a continuous film. Furthermore, at the top of the crystals a dislocation free region is obtained thanks to mechanisms of aspect-ratio trapping [147, 148], very effective because of the high height-to-base aspect ratio of the structure, and expulsion by dislocation bending [149] due to the multifaceted geometry of the growth front during the deposition.

The interest on these structures is not only for technological purpose. This peculiar growth modality can be properly considered as an extension to the third dimension of the usual heteroepitaxy of planar structures, thus opening a new insight on the fundamental processes of heteroepitaxy. More complexity has to be consider due to the additional degrees of freedom introduced when considering a fully 3D structure. The coexistence of facets with very different inclinations, exposed to different flux conditions and interacting one with each other by means of material exchanges, leads to growth modes still far from being properly understood. Pillared structures, with their fully 3D multifaceted geometry, are a striking example of such a kind of systems, so that an investigation of their growth offers the possibility to inspect new interesting aspects of 3D heteroepitaxy.

In this chapter a simple model of the mechanisms leading to this novel growth modality is presented. Simulation results are then reported for both the growth of Ge/Si and GaAs/Si pillars and closely compared with experimental observations.

5.1 Growth kinetics

From a general point of view, the growth of crystals on Si pillars is carried out in conditions of high deposition rate and relatively low temperatures, i.e. far from equilibrium.. In such conditions, the growth dynamics can be considered as substantially determined by the amount of material provided by the gaseous phase and the local efficiency to incorporate it into the crystal. The redistribution of adatoms at the surface can then be viewed as their search for a crystallization site. The continuous income of material frustrates the possibility of adatoms to follow any thermodynamic driving force towards the energy minimization so that kinetic effects dominate.

A growth model can be derived by considering the elementary processes involved in the growth [36, 37, 143, 150–153]. On the microscopic scale, the growth process can be described by considering the accumulation and redistribution of adatoms all along the surface of the crystal.

When the system is in equilibrium, the local density of adatoms $N_{\text{eq}}(\boldsymbol{x})$ is constant, resulting from the balance between generation and incorporation of the adatoms at the crystal surface. At given temperature, the former process occurs at an intrinsic rate R_g determined by the local properties of the surface (chemical species, orientation, ...) while the latter occurs at a rate R_c still dependent on the nature of the surface and also on the local adatom density. The equilibrium condition then implies

$$R_g = R_c = \frac{N_{\text{eq}}}{\tau_c}, \tag{5.1}$$

where τ_c is the crystallization time, i.e. the average lifetime of an adatom before being incorporated into the crystal.

During the growth, this equilibrium is broken by the deposition flux, increasing the local adatom density to $N_{\text{tot}}(\boldsymbol{x}) = N(\boldsymbol{x}) + N_{\text{eq}}(\boldsymbol{x})$. The excess value $N(\boldsymbol{x})$ leads to an unbalanced contribution in the incorporation rate and is then responsible for the crystallization of the deposited material. The crystal growth rate, given as the normal velocity of the growth front $\boldsymbol{v} = v\hat{\boldsymbol{n}}$, is then

$$v(\boldsymbol{x}) = R_c - R_g = \frac{N(\boldsymbol{x})}{\tau_c}. \tag{5.2}$$

More properly, v is the instantaneous growth rate since the excess adatom density N generally varies with time.

In order to define the value of N during the growth, the dynamics of the adatoms on the surface has to be considered. Generally speaking, each adatom on the surface, before being incorporated into the crystal, can diffuse along the profile or evaporate back to the gaseous phase. The evolution in time of the local adatom density N can then be described by means of a rate equation accounting for all these mechanisms:

$$\frac{\partial N}{\partial t} = \Phi - v - R_d + \nabla_S \cdot [D\nabla_S N] = \\ = \Phi - \frac{N}{\tau_c} - \frac{N}{\tau_d} + \nabla_S \cdot [D\nabla_S N]. \tag{5.3}$$

where all quantities are local, depending on the point $\boldsymbol{x}$ of the surface. Φ is the deposition flux in $\boldsymbol{x}$ and hence corresponds to a source term in the adatom balance while v and R_d are sink terms accounting for the transfer of adatoms towards the crystal or gaseous phase respectively. The local rate for evaporation $R_d(\boldsymbol{x}) = N(\boldsymbol{x})/\tau_d$ is proportional to the excess adatom density and depends on the system properties by means of the adatom average lifetime τ_d before desorption. The last term accounts for adatom diffusion according to Fick's law (the S in the operators means that all derivatives are calculated along the profile coordinates).

A full description of the growth process is then obtained by coupling eqs. (5.3) and (5.2):

$$\frac{\partial N}{\partial t} = \Phi - \frac{N}{\tau} + \nabla_S \cdot [D\nabla_S N] \tag{5.4a}$$

$$v = \frac{N}{\tau_c} \tag{5.4b}$$

where τ is the net adatom lifetime: $\tau^{-1} = \tau_c^{-1} + \tau_d^{-1}$. Note that here we are not including any thermodynamic driving force for the motion of adatoms and all contributions are determined only by the excess term, since $\partial N_{\text{eq}}/\partial t = 0$ by definition (at constant temperature).

The growth is then driven by the interplay between two factors: the external deposition flux, generating the out-of-equilibrium adatom distribution, and the adatom interaction with the surface dependent on the local properties of the system.

The net flux Φ at a given point $\boldsymbol{x}$ of the surface can be described in a spherical coordinate system, with θ and φ the polar and azimuthal angle respectively, by integrating the flux contributions from each direction $\widehat{\boldsymbol{r}}(\theta, \varphi)$, projected along the local surface normal $\widehat{\boldsymbol{n}}_S(\boldsymbol{x})$:

$$\Phi(\boldsymbol{x}) = \int_W \phi(\theta, \varphi, \boldsymbol{x}) \widehat{\boldsymbol{r}}(\theta, \varphi) \cdot \widehat{\boldsymbol{n}}_S(\boldsymbol{x}) dW. \tag{5.5}$$

$\phi(\theta, \varphi, \boldsymbol{x})$ is the angular distribution of the flux with respect to the $\boldsymbol{x}$ position, reproducing the material distribution in the growth chamber and hence it depends on the growth technique employed. The integration domain W defines all the available directions (θ, ϕ) from which the flux can be collected at the given point $\boldsymbol{x}$, i.e. the opening window between the surface and the gas source. This clearly differs from one point to the other so that $W = W(\boldsymbol{x})$. First of all, each point is exposed only to the material coming from the half of space external to the solid and therefore the net flux Φ is expected to depend

on the local surface orientation (except for spherically isotropic flux). This is schematized in Fig. 5.2 a) for the case of flux coming only from the upper hemisphere (i.e. the case of the LEPECVD reactor discussed in *Sect. 5.2*). Moreover, effects of mutual shielding of neighbouring crystals further reduce the actual amount of material that can reach a given point $\boldsymbol{x}$ of the surface. By assuming that, close to the sample, the transport of gas particles is ballistic, i.e. neglecting collisions between the gaseous reactants and bouncing effects at the surface, the effect of shielding directly results from the geometric shadowing due to the other regions along the profile, reducing the available window through which the material can penetrate to the point $\boldsymbol{x}$, as sketched in Fig. 5.2 b). This effect of mutual shadowing is highly non-local depending on the whole profile geometry and changes as the growth proceed. For the sake of simplicity, the shadowing effect in the simulations discussed in the following is calculated by assuming an infinite extension of pillars along the y direction. This is strictly correct for ridge structures and can be considered a good approximation for cross-sections in the center of pillars, since facets are quite large and corrections to the shadowing should mainly affect oblique angles that have a marginal contribution to the flux.

The characterization of the material redistribution due to the local properties is much more complicated to be defined since most of the system parameters are unknown and may in general depend on the specific growth conditions, in particular temperature and flux. τ_d, τ_c and D should depend on the local properties of the surface, such as the facet orientation and surface reconstruction, that determine the surface energetics (i.e. the adatom bonding energy) and geometry (i.e. sites distribution and density). The diffusion length for an adatom can be defined as the average distance that an adatom can cover on the surface before desorption to the gas phase or incorporation in the crystal. In the former case, the diffusion length can be defined by $L_d \sim \sqrt{D\tau_d}$. In the latter case, two mechanisms are possible. Single adatoms can be incorporated at steps or other favorable

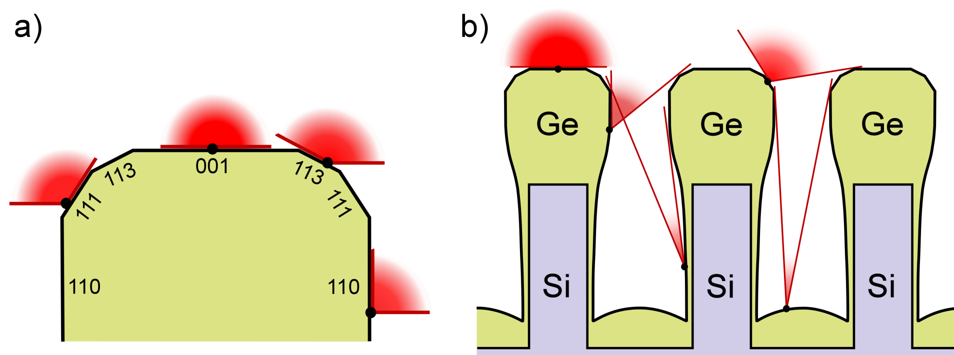

Figure 5.2: Schematic representation of the effect of the profile morphology for an isotropic flux from the upper hemisphere. a) Limitations in the flux impinging on different facets depending on their orientation. b) Reduction of the effective flux impinging at each point of the surface profile when accounting for the effect of mutual shielding.

sites on the surface, according to the intrinsic incorporation life time τ_c, thus moving for a distance $L_c \sim \; sqrtD\tau_c$. Otherwise, adatoms can crystallize at the surface when they meet with each other. The probability for such phenomenon is proportional to the adatom density on the surface so that the average life time for an adatom before meeting with another is $\propto 1/\Phi$ leading to a diffusion length $L_\Phi \sim \sqrt{D/\Phi}$. The resulting diffusion length is the smallest among them and is in general different from a point to the other since all involved quantities are local. Further assumptions are needed to reduce the number of unknown parameters.

5.1.1 Fully faceted description

The model so far described is in general meant for a smooth continuous profile while crystals are bounded by facets with well defined orientations. In *Sect. 2.2.1* the formation of a faceted profile was discussed on the basis of thermodynamics as a minimization of the surface energy for anisotropic surface energy density $\gamma(\widehat{\boldsymbol{n}})$. It is evident that also for the present conditions dominated by kinetics, the facets exposed by the crystal must be stable but their evolution during the growth can be completely different from the equilibrium crystal shape. In particular, given $v(\widehat{\boldsymbol{n}})$ the growth velocity of a facet oriented with normal $\widehat{\boldsymbol{n}}$, the kinetic crystal shape (KCS) results as the steady-state shape such to minimize the growth rate over a convex surface or maximize it over a concave surface [89, 154, 155]. In other words, the KCS is dominated by the slowest growing facets in convex regions and by the fastest ones in concave regions. Wulff construction can be used to determine the KCS in the very same way described in *Sect. 2.2.1* by simply replacing γ with v (kinetic wulff plot). Depending on the functional form of $v(\widehat{\boldsymbol{n}})$ some orientations can be excluded from the KCS. For typical crystals, $v(\widehat{\boldsymbol{n}})$ has very sharp minima and shallow maxima so that convex profiles are expected to exhibit well defined facets while a more rounded geometry is expected for concave regions.

As observed in the growth experiments, crystals grown on Si pillars have a convex geometry characterized by an almost perfect faceting from the very first stages of the growth. According to the previous argumentation, the facets found in the experiments should then correspond to minima of the $v(\widehat{\boldsymbol{n}})$ for the considered material while intermediate directions, excluded from the crystal shape, should be associated to higher growth rates.

In the assumption that the interface region between neighboring facets never give raise to orientations different from the two already existing, the kinetic evolution of the profile can be obtained by simply considering the intersections between the planes representing the motion of each facet as given by a simple translation on a distance proportional to the corresponding growth rate. The procedure, named Borgstrom construction [155], is illustrated in Fig. 5.3 a,b) for a convex region and in c,d) for a concave one. Depending on the ratio between their growth rates, neighboring facets can coexist during the growth, as showed in a,c) or, on the contrary, one facet can grow at the expenses of the other as in b,d).

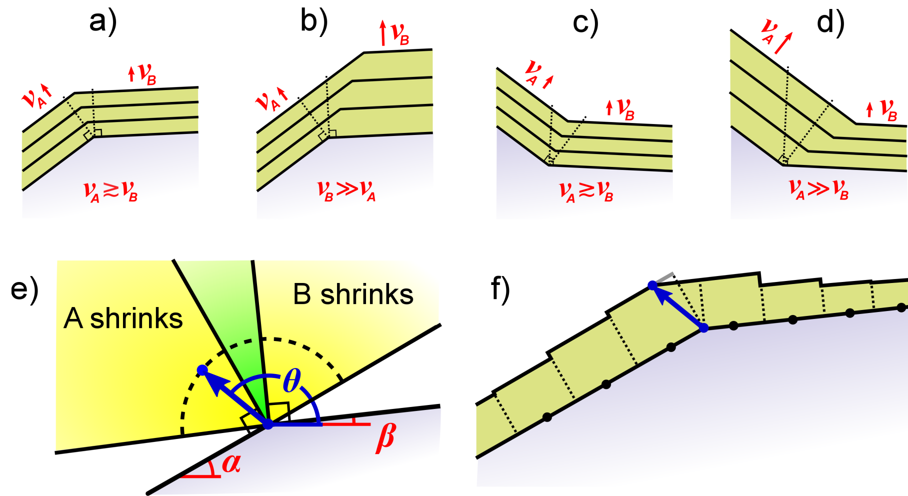

Figure 5.3: In a-d) examples of the Borgstrom construction for the profile evolution of two facets A and B moving at different velocities v_A and v_B are considered for both convex (a,b) and concave (c,d) arrangements. When growth rates for the two facets are similar they can both expand (a) or shrink (b), while for a large difference in growth velocity (b,d), the slower growing facet consumes the faster one. In e) a map of the different growth regimes for a convex profile is showed in dependence of the angle θ formed by the direction along which the boundary is moving. f) Schematics of the evolution of the discretized profile with line segments to account for non uniform conditions along the facet. Each segment moves independently along its normal, according to the local growth velocity v, leading to a stepped profile. The edge between the facets A and B is regularized according to the Borgstrom construction.

Profiles obtained in this way are equivalent to those predicted from the Wulff plot when the growth rates for intermediate directions are linearly interpolated between those of the two facets, but the approach is much simpler. Since the pillars geometry is characterized by the exposure of the same facets during the whole evolution, Borgstrom construction is appropriated to describe their growth.

As evident from *Fig. 5.3*, the relative motion of two neighboring facet can be characterized by considering the direction along which their intersection moves from one profile to the next one, as it is directly determined by the ratio of their growth velocities, from simple geometrical arguments. For a convex 2D shape, given two facets A and B forming angles α and β with respect to a reference direction (i.e. the (001) plane), the angle θ along which their intersection moves during the growth is given by

$$\tan\theta = \tan\alpha + \frac{\tan\beta - \tan\alpha}{1 - \frac{\cos\alpha}{\cos\beta}\frac{v_B}{v_A}} \tag{5.6}$$

As sketched in Fig. 5.3 e), for $\alpha > \beta$, the possible values of θ are limited by the facets themselves in the range $\theta \in [\alpha, \beta+\pi]$. The condition of coexistence of both facets, shown in panel a), is realized for values $\theta \in [\beta+\pi/2, \alpha+\pi/2]$ (green region in panel e) corresponding to small differences between the growth rates of the two facets. On the contrary, if the two facets grow with rather different velocities, θ moves into the yellow regions in e)

and the slowest facet grows in extension by consuming the other. More specifically, for $\theta \in [\alpha, \beta + \pi/2]$ facet A expands and hence its growth rate is the slowest, while $\theta \in [\alpha + \pi/2, \beta + \pi]$ implies the opposite condition and it is facet B to expand because of a lower growth rate. Finally, the limiting values $\theta = \alpha$ and $\theta = \beta + \pi$ are obtained when the growth rate of facet A or B respectively is exactly zero and the evolution of the profile is directly given by the prolongation of the immobile facet.

So far we assumed that all points belonging to a facet move in the same way but in general this is not the case since the growth velocity is a local quantity. In particular, the deposition flux can vary along the profile as a consequence of mutual shielding by neighbouring crystals. Each point along the profile is then associated to a surface element of the proper facet orientation, i.e. a line segment in 2D, and moved indipendently during the growth, according to the local velocity along its normal. As sketched in Fig. 5.3 f), if the growth rate is not uniform along a facet, a stepped profile is obtained as a consequence of the different advancing of neighboring segments. Boundaries between facets are regularized according to the Borgstrom construction, by intersecting the prolongation of terminal segments, without introduction of new facets. When facets shrink, too small segments are removed, while new segments are created in the interface region when facets grow larger. Steps can be of any height so that there is no direct connection with atomic steps. Moreover, the orientation of the segments is never allowed to vary, even when the step density and height become so large that the transformation into a facet with different orientation could be favored.

Since the growth conditions vary during the deposition process, e.g. because of variations in the local transport or shadowing effects, the relative velocity of neighboring segments is continuously changing in time and hence the relative extension of facets as well as their stepped appearance are in general dynamically evolving from one profile to the other.

Finally, for a perfectly faceted surface, different diffusion coefficients could be expected for intra-facet diffusion, i.e. adatoms moving on the same facet, and inter-facet diffusion, i.e. adatoms moving from one facet to the other, the latter process eventually limited by kinetic barriers [37, 85, 156]. Similarly, additional energy barriers could be expected in correspondence of steps (e.g. Erlich-Schwoebel barriers [42]), thus altering the diffusivity on highly stepped facets.

5.1.2 Quasi-stationary solution without diffusion

Due to the high growth flux it is reasonable to assume that the limiting process for adatom diffusion is the high deposition rate. In a first approximation this allows to neglect the diffusion term in the rate equations (5.4) thus leading to a local growth rate that depends only on the balance between incorporation and desorption of the material deposited from

the flux at each point:

$$\frac{\partial N}{\partial t} = \Phi - \frac{N}{\tau} \tag{5.7a}$$

$$v = \frac{N}{\tau_c} \tag{5.7b}$$

Assuming as initial condition the equilibrium state $N(t = 0) = 0$ and a constant deposition flux Φ, the solution for the adatom density is

$$N(t) = \Phi\tau \left[1 - \exp\left(-t/\tau\right)\right]. \tag{5.8}$$

The evolution of N is then characterized by an initial transient during which the adatoms accumulate at the surface until the stationary value $N_{\text{staz}} = \Phi\tau$ is reached. According to eq. (5.7) the growth rate v then increases up to the stationary value:

$$v_{\text{staz}} = \frac{N_{\text{staz}}}{\tau_c} = \frac{1}{1 + \frac{\tau_c}{\tau_d}}\Phi = \chi\Phi, \tag{5.9}$$

where we define the incorporation factor $\chi = \left[1 + \tau_c/\tau_d\right]^{-1}$ representing the fraction of the incident flux that is crystallized. At fixed temperature, χ is expected to depend on the crystal facet orientation.

Notice that the stationary condition is locally defined at each point of the surface and rely on the assumption of constant deposition flux. The existence of mutual shielding effects is however responsible of variations in the flux during the growth process, thus opposing to establishing a stationary state. Nevertheless, on practical purposes the evolution of the crystals grown of pillars here considered is quasi-stationary since the flux vary smoothly and slowly compared to the transient time constant τ. For the same reason, the transient from the initial equilibrium state is expected to play a very marginal role on the whole deposition process. Furthermore, it is during such initial stage that the typical facets are formed but this process cannot be considered within our simple model. To by-pass useless complications, simulations are started from a profile already including all characteristic facets, assuming that quasi-stationary conditions holds from the very beginning.

5.2 Growth of Ge crystals on Si pillars

The growth of 3D crystals of Ge on top of Si pillars was demonstrated in Ref. [2]. Therein it was shown that by depositing Ge onto several arrays of Si pillars, high quality 3D towers of Ge can grow up to tens of µm without coalescence (see Fig. 5.4 a). The morphology of these structures has been extensively investigated by high resolution SEM and AFM showing an almost perfect faceting characterized by in top region by well defined facets

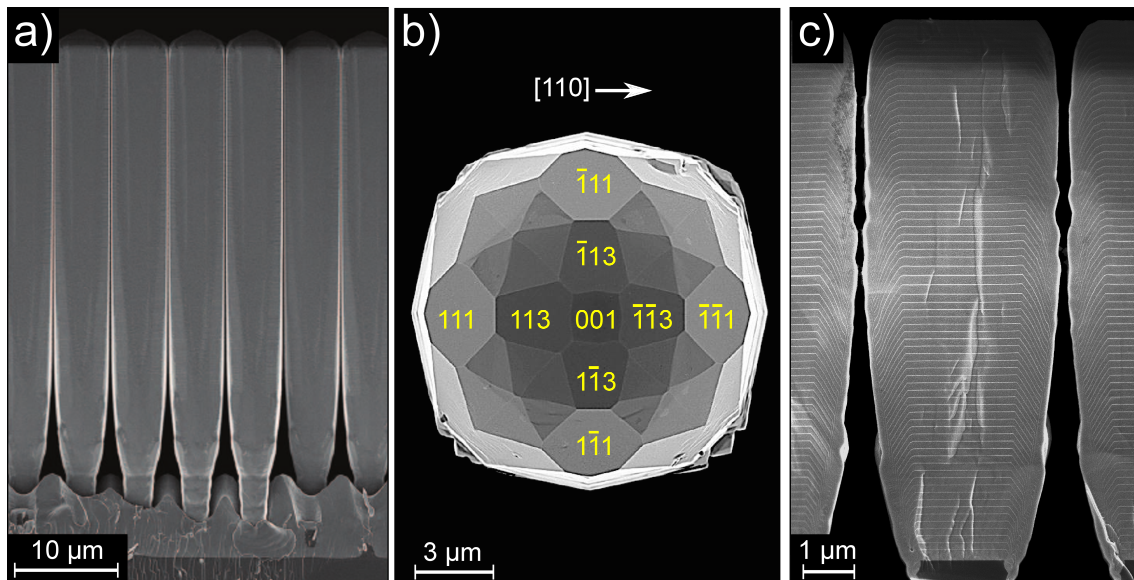

Figure 5.4: SEM images of 3D Ge crystals grown on 2µm wide Si pillars. a) Lateral view of crystals grown at 490°C up to 50 µm on a Si pillar array with 4 µm trenches (from Ref. [2]). Note that each crystal grows separated from each other by a small channel of ∼50 nm. b) Top view of an isolated pillar after 3 µm Ge deposition at 490°C, showing the typical (001), {113} and {111} facets. c) Cross-section along [110] direction of crystals grown introducing 10 nm thick marker layers of SiGe (10% Si) every 100 nm of Ge deposition. The sample was grown at 500°C up to 8 µm Ge deposition on a pattern with 2 µm trenches.

with main orientations (001), {113} and {111}, bounded by almost vertical {110} sidewalls. Samples were also grown introducing SiGe marker layers at regular intervals during the growth leaving a footprint of the profile evolution as shown in *Fig. 5.4* c).

The characterization of the key features of this peculiar growth modality was carried out by means of numerical simulations, as discussed in the remainder of this section.

5.2.1 Model definition

LEPECVD flux modeling

The deposition of Ge/Si at high rate was performed by Low-Energy Plasma-Enhanced Chemical Vapor Deposition (LEPECVD) reactor. An accurate modeling of the gaseous flux into the growth chamber was reported in Ref. [157, 158]. As a first approximation the gaseous reactants (mainly GeH_3 and GeH_2 from decomposition of GeH_4 precursor) originate from the region of the plasma in front of the sample and then reach its surface after several collisions so that the impinging material can be assumed to arrive from all directions of the hemisphere on the source side. A certain degree of directionality is however expected on the vertical direction between the emitter and the sample, mainly due to the contribution of ionized species, in particular GeH_3^+, drifting in the direction of the sample because of the electric field in the chamber. An essential description of the flux geometry can then be obtained assuming the superimposition of an isotropic contribution

$\Phi_\cap$ and a vertical one $\Phi_\downarrow$, as sketched in the Fig. 5.5 a). The isotropic contribution is dominant and was estimated to be ~70% of the total flux [1]. Due to the large distance between the sample and the emitting plasma (~cm) compared to the sample lateral size ($\sim \mu$m), all points on the sample are assumed to be exposed at the very same flux distribution $\phi(\theta, \varphi, \boldsymbol{x}) = \phi(\theta, \varphi)$.

In order to calculate the net flux at each point of the surface it is convenient to orient the spherical coordinate system as illustrated in Fig. 5.5 b), with the polar axis along the horizontal direction in the plane of the facet. For the sake of simplicity we assume that no shadowing occurs in this direction so that $\theta \in [0, \pi]$ and the available portion of the flux hemisphere is entirely traced by the azimuthal angle φ (this approximation would be strictly correct for infinite ridge structures). For this flux geometry, $f(\theta, \varphi) \sim \Phi_\cap + \Phi_\downarrow \delta(\theta - \pi/2)\, \delta(\varphi - \pi/2)$ so that eq. (5.5) becomes

$$\begin{aligned} \Phi(\boldsymbol{x}) &= \int_W \left[\frac{\Phi_\cap}{\pi} + \Phi_\downarrow \delta(\theta - \pi/2)\, \delta(\varphi - \pi/2) \right] \widehat{\boldsymbol{r}}(\theta, \varphi) \cdot \widehat{\boldsymbol{n}}_S(\boldsymbol{x}) \sin\theta d\theta d\varphi = \\ &= \frac{\Phi_\cap}{2} \int_C \sin(\varphi - \alpha(\boldsymbol{x})) d\varphi + \Phi_\downarrow \cos\alpha(\boldsymbol{x})\, \Theta(\pi/2 - \alpha(\boldsymbol{x})) \end{aligned} \tag{5.10}$$

where α is the surface inclination with respect to the (001) plane and the integration domain $C = C(\boldsymbol{x})$ is given by the range of admissible φ. The Dirac δ localize $\Phi_\downarrow$ along the vertical direction and contributes to the integral only if the facet inclination is less then vertical, as given by the Heaviside Θ function.

In the absence of shadowing effects it is straightforward to obtain $C : \varphi \in [\alpha, \pi]$ and hence the net flux at the surface depends only on the local surface orientation $\alpha(\boldsymbol{x})$ as:

$$\Phi(\alpha) = \Phi_\cap \frac{1 + \cos\alpha}{2} + \Phi_\downarrow \cos\alpha\, \Theta(\pi/2 - \alpha) \tag{5.11}$$

The function $\Phi(\alpha)$ is shown in Fig. 5.5 c), where the separated contributions from $\Phi_\cap$ and $\Phi_\downarrow$ are also reported. For a flat (001) facet the flux is the maximum value $\Phi_0 = \Phi_\cap + \Phi_\downarrow$. By inclining the surface, the flux gradually decreases both because part of the hemisphere is covered by the facet itself and because of the oblique incidence. For angles larger than 90°, the vertical direction is excluded and hence the net flux is only given by the isotropic contribution $\Phi_\cap$.

When accounting for the geometric shielding due to other regions along the profile, the available window through which the gas can reach the surface point $\boldsymbol{x}$ is reduced as sketched in Fig. 5.2 b).

[1] The actual ratio $\Phi_\cap/\Phi_\downarrow$ was justified *a posteriori* by a systematic analysis of the material accumulation into the deep trenches between ridge structures.

Kinetic parameters

Despite the rich literature concerning SiGe and their growth, most of the system parameters are far from being well established due to its large variability of conditions and growth modality.

In a first approximation, it is possible to exclude the contribution of adatom diffusion. From a simple Arrhenius law: $D \sim \exp(-E_a/kT)$, where E_a is the activation energy for diffusion that we expect to be $\gtrsim$1 eV [114], for the typical temperature range of experiments $T = 400$-600°C and high growth rate considered Φ_0 ~nm/s, the expected diffusion length is ~100-200 nm, that is much smaller than the pillar dimensions. Accordingly, the length of the line segments considered in the profile discretization (as illustrated in *Fig. 5.3* f) was chosen to match, on average, this size.

In order to estimate the other kinetic parameters, the role of the different facets must be accounted for. Attempts to define a hierarchy for the growth rates of stable facets are reported in Refs. [77, 153, 159–161]. Consistently it is recognizable that SiGe crystal commonly exhibits {111} and {113} facets, as observed for the crystals here considered, the former are expected to be the most stable while the latter are exposed because of their low growth velocity. To escape from the literature indeterminacy we followed an a posteriori approach using the experimental data to determine a best fit of the model parameters.

In particular, in the absence of shielding effects, i.e. for isolated pillars, the growth flux on each facet is uniform and constant in time and its values is given by the modeling

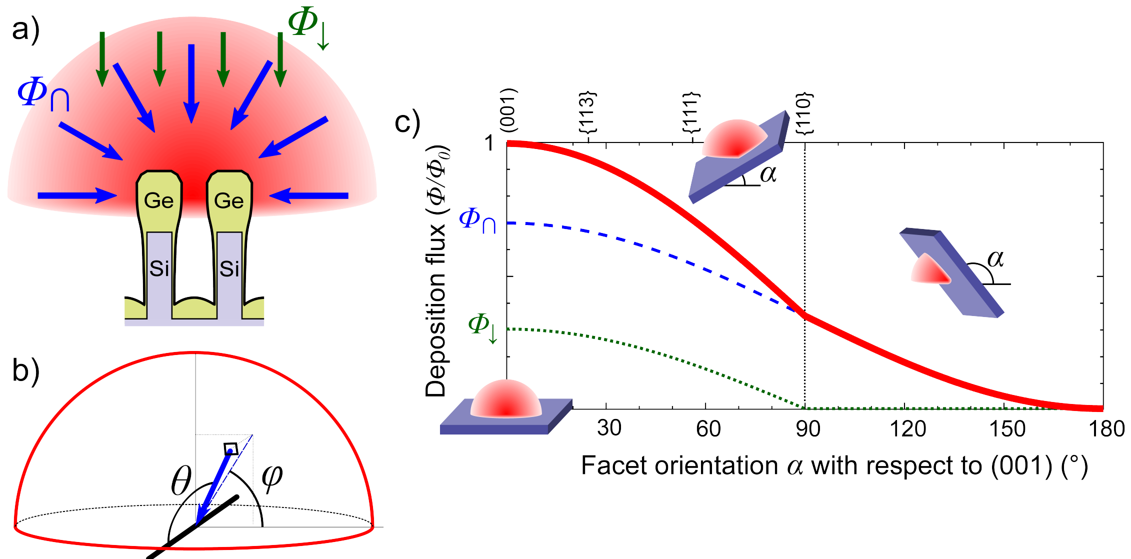

Figure 5.5: a) Schematic representation of the deposition flux given by an isotropic contribution $\Phi_\cap$ from the hemisphere above the sample and a vertical contribution $\Phi_\downarrow$. b) Geometrical definition of angles θ and φ for the integration of the flux distribution in eq. (5.10). c) Variation of the net flux as a function of the angle formed by the facet with the (001) plane. The trend of the isotropic $\Phi_\cap$ and $\Phi_\downarrow$ contributions are also shown.

	v/v_{001}	Φ/Φ_{001}	χ	τ_c (s)	N_{staz}
001	1	1	0.91	0.010	0.31
113	0.91	0.94	0.87	0.014	0.40
111	0.65	0.74	0.80	0.024	0.48
110	0.28	0.38	0.67	0.049	0.42

Table 5.1: Model parameters for the different facets of the profile. Growth velocities with respect to (001) facets are obtained from the experimental profiles. τ_d=0.1 s for all facets.

of LEPECVD discussed above. Furthermore, since the flux is not changing, stationary conditions hold (*Sect. 5.1.2*) and hence the growth velocity of each facet is constant during the whole growth process. This is confirmed in the experimental profiles of isolated pillars (Fig. 5.6) by observing that the edge between two facets (the vertexes in the 2D cross-sections) is moved along a straight line, whose direction is determined by the ratio of the facets growth rates, according to the eq. (5.6). The measure of the angle θ formed by the lines traced by connecting the profile vertexes at different growth stage thus permit a direct estimation of the relative growth rates for each facet (this procedure is equivalent to measure the ratio between the motion along the normal for each facet, but we expect it to be more accurate). Notice that since the growth velocities for each facet are uniform and constant, the observed profiles corresponds to the kinetic crystal shape as discussed in *Sect. 5.1.1*. Since the flux distribution for isolated pillars is known (see Fig. 5.5 c), once the relative growth rates have been determined, it is straightforward to evaluate the ratio between incorporation factors.

Notice that relative velocities fully characterize the evolution of each facet so that in principle it is not necessary to define absolute values. Nevertheless, a reasonable guess of the parameters for the (001) reference facet can be done to estimate such quantities. In particular we assumed that the probability for an adatom to evaporate or being etched by H species is at least one order of magnitude lower than that of being incorporated into the crystal and set τ_c(001)= 0.01 s and τ_d= 0.1 s, leading to $\chi_{(001)}$=0.91. This choice ensure that the excess adatom density N is always less than 1 monolayer and that stationary conditions are quickly reached after depositing a few nm of Ge. Since $\chi_{(001)} < 1$, in order to keep the growth rate for the (001) at the nominal value of v_{001}=4 nm/s the total impinging flux was estimated to be $\Phi_0 \approx v_{001}/\chi_{001}$=4.4 nm/s. Finally, in the further assumption that the evaporation process do not depend on the facet orientation (i.e. τ_V is a constant), the different incorporation lifetimes τ_c can be directly estimated for each facet from the values of χ. The actual values of model parameters, calculated from the isolated pillar profiles in Fig. 5.6 a), are reported in Table 5.1.

5.2.2 Simulation results

As discussed above, the tuning of the kinetic parameters required for the growth simulations are directly based on the analysis of SEM profiles of isolated pillars. First of all it is

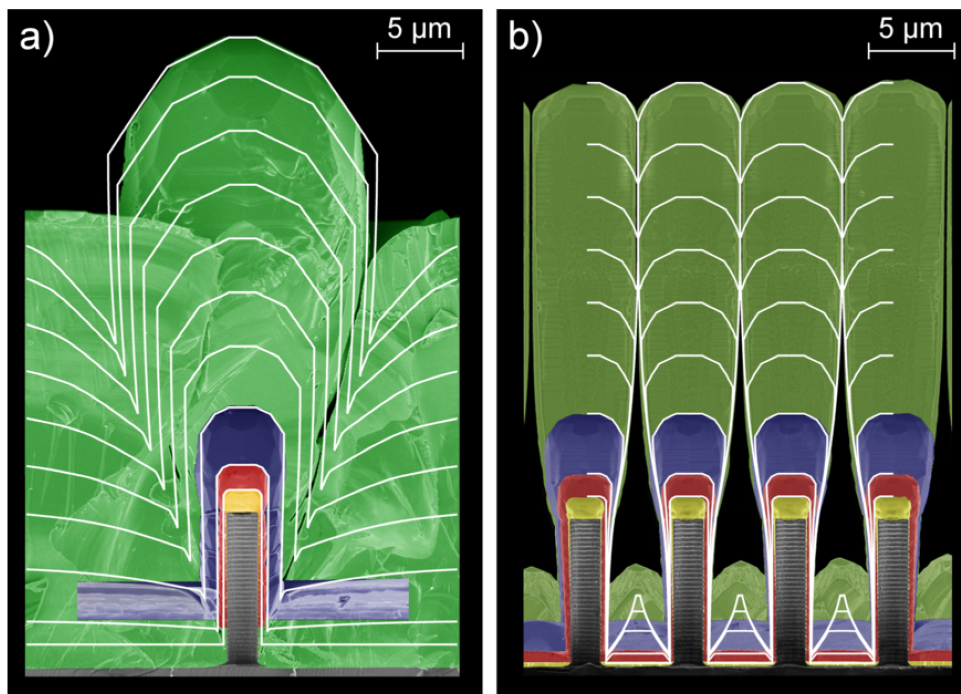

Figure 5.6: Comparison between SEM micrographs (colored images) and simulated profiles (white lines) for the growth of an isolated pillar a) and an array of pillars spaced by 4 μm trenches b). SEM profiles are obtained by alignment of images of samples obtained by deposition of different amount of Ge, corresponding to the different growth stages. In both cases, the initial Si pillars are 2 μm wide and 8 μm high and the growth temperature is 490°C. (Pictures are published in Ref. [2]).

then crucial to verify the consistency of such estimates by reproducing the growth of the very same isolated pillars. The result is reported in Fig. 5.6 a) where the profiles obtained by the simulations are directly superimposed to the SEM micrograph of samples at different growth stages. The experimental morphology is well reproduced by the simulations, especially for the initial deposition up to 10 μm. Notice that the pillar partially shields the substrate immediately around, leading to a zone of partial depletion surrounding the pillar.

When pillars are put one close to each other, as in Fig. 5.4 a), crystals grow almost vertically. A sequence of the different growth stages is reported in Fig. 5.6 b), where SEM micrographs measured for samples at different deposition thicknesses are compared with the corresponding predictions of growth simulations, performed with the very same parameters considered for the case of isolated pillar. The good overlap between experimental and calculated profiles permits to explain the crystals self-alignment as a direct consequence of the mutual shadowing between neighboring pillars, responsible for the shrinkage of the deposition flux, and hence of the growth velocity, on the {110} sidewalls while the gap decreases. However, in contrast with experiments, in the simulations crystals are bound to touch each other and fuse together. This fate is however delayed to later deposition stages thanks to the strong drop of the impinging flux at small distances. For the

deposition range considered in the simulations, Ge crystals never touch but continuously get closer, up to fractions of nm. A small cutoff on the flux would be enough to stop the lateral growth as in the experiments but the physical description of such phenomenon is beyond the definition of the present model. Moreover, fusion between crystals was observed for different growth conditions so that the actual behavior when the crystals get closer demands for further investigations. Finally, notice that the accumulation of material into the bottom trenches leads to sharp peaks that would be made smooth by the activation of some diffusion.

It is important to notice that despite the smooth appearance of the simulated profiles, they are always meant as composed by line segments along the main directions: (001), {113}, {111} and {110}. The apparent curvature of regions along the profile is then the result of the sequence and amplitude of steps between neighboring segments. In Fig. 5.7 a magnification of the most relevant regions along the profile is shown. Regions 1 and 3, i.e. the top and bottom part of the pillar sidewalls are nearly flat since all segments tend to move with very similar velocity because the incoming flux was uniform and close to zero by full shielding. On the contrary the region 2 in the middle, is rather curved since the incoming flux there suffered the largest variation during the growth, as the pillar-pillar distance was critically decreasing, leading to significant differences in the motion of neighboring segments and hence to taller steps.

Finally, the detailed view of region 4, corresponding to the {111}-{110} border reveals a curved profile of the {111} facets, determined by a slower motion of the line segments close to the border with respect to those far away. This is clearly another consequence of flux shadowing since the border region is the part of {111} facet at the smaller distance

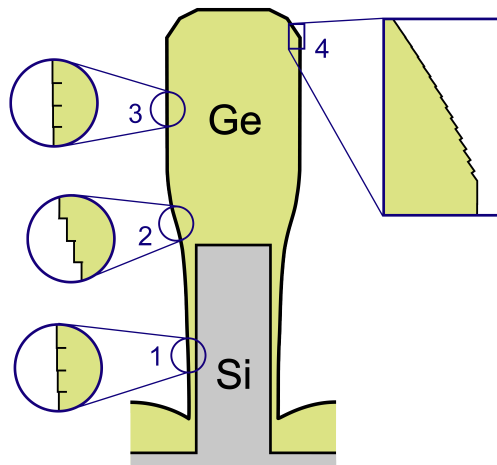

Figure 5.7: Magnification of the structural details of a typical pillar profile showing the relative positions of each line segment along the {110} sidewalls (regions 1-3) and on the {111} top facet (region 4). Notice how curved regions are formed by larger steps between the segments. The curved profile of {111} facets arise from the different shielding effect along the facet when pillars gets close together.

from the neighboring pillar where a larger reduction of the flux occurs. The same effect should happen also on the {113} facet but, due to the larger distance from the neighboring crystals, the flux cutoff becomes negligible.

Samples were grown for different pattern geometries, changing both the pillar size (from 1 up to 15 µm) and the gap (from 1 up to 50 µm). Again, experimental observations are in good agreement with simulation predictions. In particular, a close comparison of the profiles in Fig. 5.8 a-c), differing only for the width of the gap, show that it mainly affects the extension of the lateral growth because of the variation in the mutual shadowing of neighboring pillars. The smaller is the gap (a) the stronger is the cutoff of the flux from the very beginning of the growth and hence a negligible amount of material is attached on the sidewalls of the initial Si pillars and in the bottom of the trenches. The lateral expansion of the crystals occurs only at the top region and shortly leads to the closure of the gap. On the contrary, a larger spacing between the pillars (c) permits a larger penetration of the flux into the bottom trenches and on the sidewalls. In order to close the gap a larger lateral expansion is required and this happens only at later stages of the growth. It is interesting to notice that in the top region, both {111} and {113} gets larger when increasing the pillar-pillar gap, while the top (001) flat region is almost the same. This can be explained again as a consequence of mutual shielding. Notice how the sequence of profiles is consistent with the evolution observed for the samples grown with marker lines, as in *Fig. 5.4* c). In particular, notice the close similarity between *Fig. 5.4* c) and the calculated profiles in *Fig. 5.8* b), obtained for very similar conditions.

In fact, while pillars are well separated, both {111} and {113} expands as for the isolated system but when the gap shrinks, their relative extension decreases since {111} facets shrinks from the border with {110} and expand at the expenses of the neighboring {113} facet, because v_{111} is decreased by the flux shadowing

The role of the pillar size is more trivial, just affecting the extension of the (001) tops at the different growth stages as observed when comparing the profiles in Fig. 5.8 c-d). No effect is found on the relative growth of the facets and on the lateral expansion, the lateral profiles being exactly the same.

So far the same temperature of 490°C was considered since a complete set of experiments was performed at such temperature allowing for a better fitting of the model parameters. Several samples were however grown at different temperature, ranging from 415°C to 585°C, revealing the occurrence of different morphologies as shown by the SEM profiles in Fig. 5.9 a-c). In particular, as evidenced in the insets, the profile of the pillars top changes continuously from almost flat (001) surface at the lowest temperature of 415°C (a), to partly faceted at 515°C (b), and finally to a full pyramidal shape at 585°C (c). On the basis of the principle that a facet grows larger when its velocity is small compared to neighbors, this shrinkage of the flat top region at increasing temperature can be associated with an increase of the relative growth rate of the (001). By measuring the size variation of the (001) facet with respect to the initial pillar geometry, following the geometrical

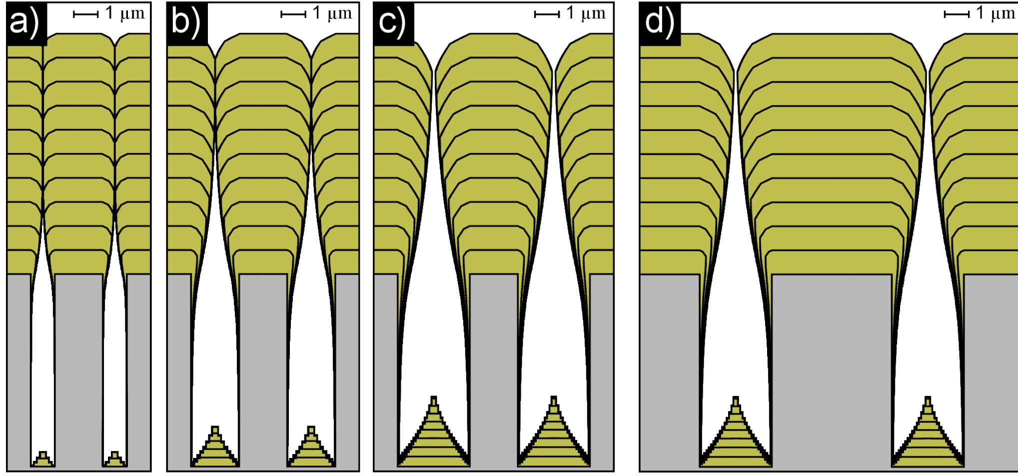

Figure 5.8: Growth simulations for different pattern geometry. In a-c) the pillar size is 2 µm and trenches are a) 1, b) 2 and c) 3 µm wide; in d) 5 µm pillars are considered with 3 µm trenches. Profile are shown every 1 µm of Ge deposition, up to 10 µm.

construction of Fig. 5.3, it is possible to roughly estimate the velocity ratio v_{113}/v_{001} facets at each growth temperature. In particular, we obtain v_{113} ≈93% v_{001} for the lowest temperature of 415°C, 89% at 515°C and 86% at the highest temperature of 585°C. Since no data are available for isolated pillars and at different growth stages, rates for the other lateral facets cannot be extrapolated. In order to perform simulations, we assume that their ratio with respect to the growth rate of {113} facets are the same determined for the case study at 490°C. The profiles predicted by the simulations are shown in Fig. 5.9 d-f), in good agreement with the experiments. As expected at the lowest temperature (d) the (001) top facet enlarges during the growth so that when the gap shrinks, a full tessellation of the space is achieved with flat units corresponding to each pillar. At intermediate temperature (e), both (001) and {113} facets coexist producing a dome-like faceted profile similar to the one observed at 490°C (Fig. 5.6). Finally for the highest temperature (f) the (001) top region grows much faster than neighboring facets and shrinks until it disappears, leading to a pyramidal structure at the top, bounded by {113} facets.

The physical reasons of the variation in the relative growth rates at different temperatures can be quite complicated since in principle material parameters χ (i.e. τ_c and τ_d) and D are temperature dependent. One possibility could be that at higher temperature χ_{113} decreases (i.e. lower efficiency of the crystallization process or higher rate of vaporization) then reducing the grow rate of {113} facets. On the other hand, the higher thermal energy can activate the mechanisms for diffusion both inside a facet (intra-facet diffusion) and between neighboring facets (inter-facet diffusion). If adatoms tend to accumulate on the {113} facets they can be transferred toward the (001) facet, then causing the enhancement of its growth rate.

In order to inspect the effect of diffusion that was so far assumed as negligible it is necessary to restore the term $\nabla_S \cdot [D\nabla_S N]$ in eq. (5.7). In Fig. 5.10 a) a comparison of the

profile evolution obtained for the case of no diffusion, intra-facet diffusion only and both intra- and inter-facet diffusion is reported at different growth stages. Profiles obtained when activating intra-facet diffusion only are quite similar to the case with no diffusion at all. The main effect of diffusion inside a facet consists in making the adatom density homogeneous all along the facet. This mainly affects the lateral growth redistributing the larger amount of material deposited at the top part of the {110} toward the lower part so that the sidewalls looks smoother. The same smoothing effect give raise to a more gentle peak of the material filling the trenches.

The profile obtained when activating also the inter-facet diffusion is much different from the case with no diffusion. In particular, adatoms are removed from {113} and {111} facets and accumulated on the (001) and {110} facets respectively. A clear trace of this transfer is the material overgrowth on top of such facets (recognizable also in some experimental profiles). The direction of this motion is given by the adatom density difference between the facets that for our choice of parameters imply accumulation on the {113} and {111} facets. The macroscopic effect of this material transfer is equivalent to an increase of the growth velocity of the (001) and {110} facets, leading to a shrinkage

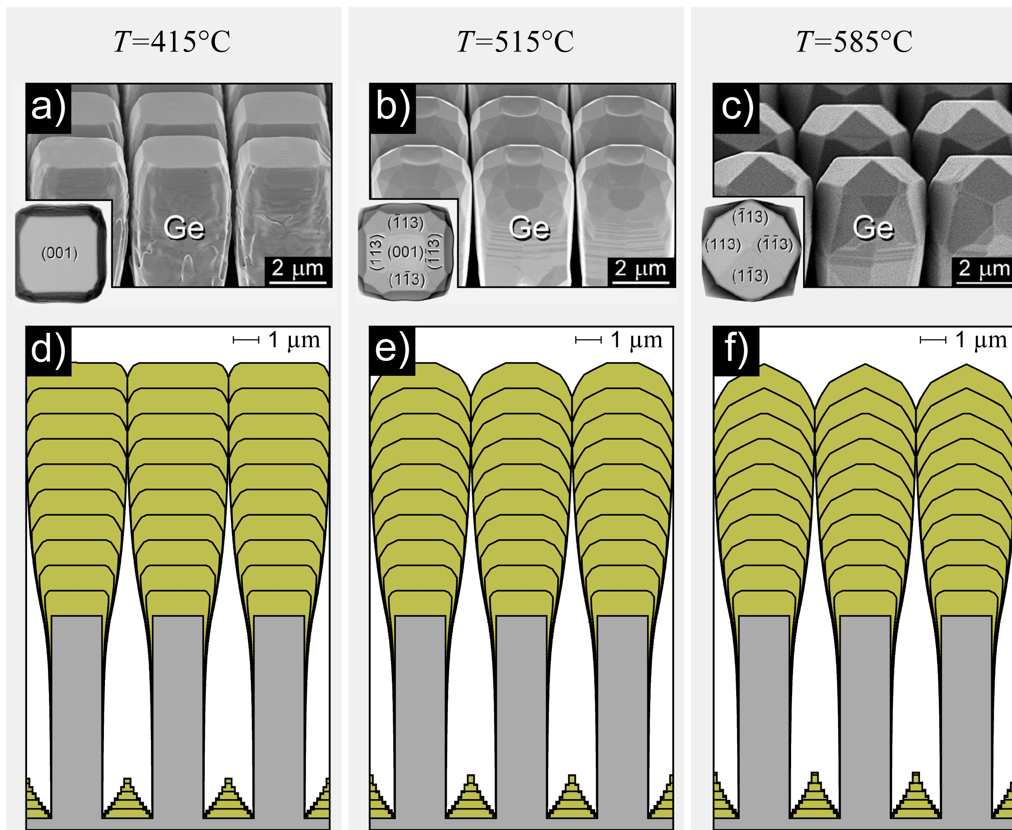

Figure 5.9: a-c) SEM profiles of pillars grown at three different temperatures, compared with simulations d-f) showing the evolution at the different deposition stages. Pillars are 2 μm large and spaced by 2 μm. Experimental profiles are measured after growing 8 μm Ge, while simulated profiles are reported for each μm deposited, up to 10 μm.

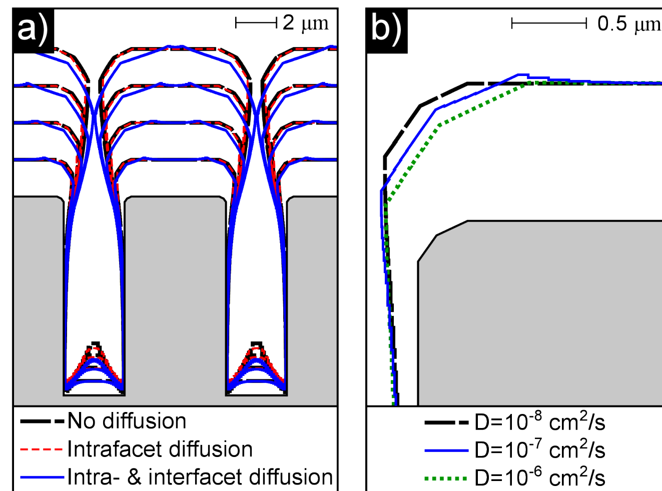

Figure 5.10: a) Comparison of the profile evolution for different activation of the diffusion mechanisms ($D = 10^{-7}$ cm^2/s). b) Detail of the profiles after deposition of 1 µm Ge for three different values of D. In both a) and b), parameters are the same evaluated for the case at 490°C of Fig. 5.6. Notice that at this temperature $D \sim 10^{-8}$cm^2/s. Pillars are 2 µm large and spacing is 3 µm.

in their extension. Notice that the evolution closely resembles that of samples grown at high temperature (Fig. 5.9 c) thus suggesting a possible explanation for the trend observed experimentally since D is expected to increase with temperature ($D \sim \exp(-E_a/kT)$).

The effect of the diffusion term strongly depends on the magnitude of the diffusion coefficient D as evidenced in Fig. 5.10 b). For the lowest value of 10^{-8} cm^2/s the profiles looks practically the same of the case with no diffusion at all. Since such a value of D is our estimate for the diffusion coefficient at 490°C considered in the previous analysis, this confirms our assumption of neglecting the contribution of diffusion. When increasing D by an order of magnitude we obtain the overgrowth effect on (001) and {110} facets discussed before while the growth of {113} and {110} facets is slower. Finally, when increasing again D by ten times more, {113} and {110} facets growth rates decrease further but the overgrowth peaks disappear since the larger adatom mobility allows for a redistributing of the transferred material all along the facet. This reveals that the overgrowth effect is limited to intermediate diffusivity, such to have enough adatom mobility to allow for their transfer between the facets but sufficiently slow to avoid that they redistribute uniformly on the entire facets.

Finally, it is important to address that the assumption of short diffusion lengths, considered in all previous calculations, is well suited for high flux conditions. Diffusion can however play a role where the flux is diminished by shadowing effects, in particular on the lateral sidewalls when pillars get closer.

5.3 Growth of GaAs crystals on Si pillars

It has been recently demonstrated [38] that 3D crystals of GaAs can be successfully grown on Si pillar patterns by MBE heteroepitaxial growth. Crystal quality is found to be very high, even comparable in the top region to GaAs bulk, and, after deposition of few μm almost all dislocations are removed.

An example of such structures is shown in Fig. 5.11. The deposition is highly non-conformal, characterized by limited lateral expansion and small growth on the pillar lateral sidewalls. The top morphology is given by well defined facets, with an anisotropy between the [110] and [$1\bar{1}0$] directions due to the substrate miscut of 6°, which reduces the crystal symmetry. The morphological evolution of the GaAs crystals can be followed in Fig. 5.11 c), where SEM images of the top of the 3D-crystals are shown for 1, 2 and 4 μm epilayer thicknesses. In d) a TEM image of a cross-section along the [110] direction of a sample grown with AlGaAs markers every 250 nm is shown, revealing the sequence of growth of the crystal up to 4 μm GaAs deposition. The crystal growth front is constituted, up to ~1 μm thickness, by the coexistence of a (001) surface, which tops the crystal, and inclined facets with {11n} orientation. The average inclination corresponds to {113} facets, however accurate AFM analysis shows the simultaneous presence of {112} and {114} facets with large steps among the terraces. Moreover, due to the substrate miscut a certain anisotropy is found in the top morphology, with steeper facets along the [$1\bar{1}0$] direction. Increasing the GaAs coverage the central (001) area completely disappears (b) and, starting from 4 μm, new {012} stepped surfaces appear at the four pillar corners and lead to a faceted top, rotated by 45°on the (001) plane.

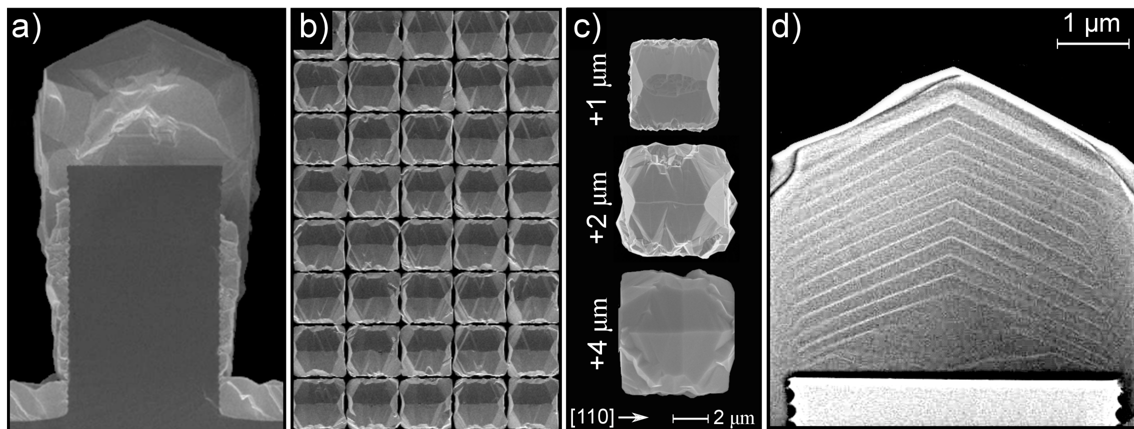

Figure 5.11: a-c) SEM micrographs of GaAs crystals grown at 580°C on a squared pattern of Si pillars 5 μm wide and 8 μm high, separated by 4 μm trenches. The geometry obtained after deposition of 4 μm of GaAs is reported for a pillar cross-section, cut along [110] direction a), and in top view b). In c) the different top morphology is reported at different thickness of GaAs deposited (1,2 and 4 μm). d) TEM cross-section along [110] direction of a sample grown as in a), including AlGaAs markers every 250 nm of GaAs deposition in order to track the profile evolution at different growth stages. AlGaAs lines are ~20 nm thick, except the last one that is ~200 nm.

Growth simulations are limited to two dimensions and hence they can only offer a qualitative characterization of the profile evolution in cross-section. In particular, a reasonable representation of the system geometry can be defined by considering a [110] cross-section with (001) and {113} facets for the top region and {110} sidewalls. Of course, this is valid up to the appearance of {012} facets, whose description demands for a proper 3D description that is out of the scope of the present model.

5.3.1 Model definition

MBE flux modeling

The growth of GaAs/Si was performed by Molecular Beam Epitaxy (MBE), operated at high deposition flux. In particular a nominal grow rate of 0.15 nm/s was used, much slower than the LEPECVD value but corresponding to a very high flux for the typical MBE growth conditions. Atomic Ga is deposited on the sample surface and incorporated in the GaAs crystal by interacting with the As atoms introduced in the gaseous phase of the growth chamber with an appropriate partial pressure. For the typical growth conditions here considered it is assumed that As is always available to interact with Ga at the surface so that the growth rate is fully determined by Ga. The As/Ga ratio is $\sim$30 limiting Ga mean free path to less that 100 nm.

In a first approximation the MBE flux can be defined as sketched in Fig. 5.12 a). The flux emitted from the source is directed along a direction forming an angle θ_i from the vertical direction. The sample rotates around the vertical axis. The average flux impinging at each point is then originating from the cone of opening angle θ_i traced by the relative motion of the source so that the flux distribution has cylindrical symmetry $f(\theta, \varphi, \boldsymbol{x}) \sim \delta(\theta - \theta_i)$. Eq. (5.5) then reads as:

$$\begin{aligned} \varPhi(\boldsymbol{x}) &= \frac{\varPhi_0}{2\pi \cos\theta_i} \int_C \widehat{\boldsymbol{r}}(\theta_i, \varphi) \cdot \widehat{\boldsymbol{n}}_S(\boldsymbol{x}) d\varphi = \\ &= \varPhi_0 \cos\alpha(\boldsymbol{x}) \left[\frac{1}{2\pi} \int_C d\varphi \right] - \varPhi_0 \tan\theta_i \sin\alpha(\boldsymbol{x}) \left[\frac{1}{2\pi} \int_C \cos\varphi d\varphi \right], \end{aligned} \tag{5.12}$$

where $\varPhi_0$ is the nominal flux, corresponding to the growth rate of a (001) surface, C is the part of the base circumference of the cone from which material can reach the surface, α is the angle formed by the surface with respect to the (001) plane at the given point $\boldsymbol{x}$.

When neglecting the shadowing effects, the net flux at each point depends on the local surface orientation only, as shown in Fig. 5.12 b) for the incidence angle $\theta_i = 30°$ of the MBE machine used to grow the sample here considered.

Three different conditions can be distinguished according to the different alignment between the surface and the flux cone. For α ranging from $0°$ to $90° - \theta_i$, the whole deposition cone contributes to the net flux. The evaluation of the integral of eq. (5.12) over the entire domain $C : \varphi \in [0, 2\pi]$ leads to $\varPhi = \varPhi_0 \cos\alpha$, i.e. the net flux is equal to

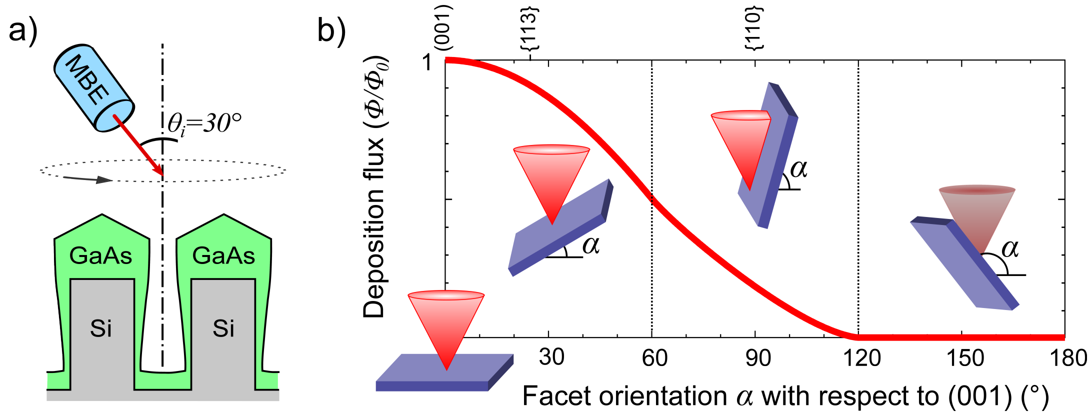

Figure 5.12: a) Schematic representation of the MBE flux geometry. b) Variation of the net flux as a function of the angle between the surface and the (001) plane for an incidence angle θ_i=30°.

the projection of the nominal flux along the normal to the surface, independently of the angle θ_i. Increasing the surface steepness, for angles in the range $90° \pm \theta_i$, part of the deposition cone is covered by the facet itself and do not contribute to the net flux. In this case $C : \varphi \in [\varphi^\star, 2\pi - \varphi^\star]$ where $\varphi^\star = \varphi^\star(\alpha)$. Finally, when the inclination gets larger than $90° + \theta_i$, no material can reach the surface since the deposition cone is fully excluded by the surface itself.

Shadowing effects can exclude additional parts of the deposition cone thus reducing the net flux. The shadowing is calculated in the approximation of infinitely extended facets. In this case, the effect is present only if the angle of shielding is in the range $90°\pm\theta_i$, i.e. such to reduce the actual deposition cone. For the present case of θ_i=30°, (001) and {113} facets forming the top of the GaAs crystals are not affected by any shadowing.

Kinetic parameters

Many studies of GaAs growth kinetics are available from literature [85, 93, 151] but data strongly depends on the specific growth technique and system conditions thus limiting the possibility to extract some general information.

In order to setup the growth simulations to reproduce the formation of pillars, some approximations can be considered. First of all, it is reasonable to neglect adatom diffusion since an high partial pressure of As was imposed in the growth chamber (As/Ga ratio was set to be ~20) such to induce an almost immediate crystallization of the Ga deposited at the surface and hence limit the diffusion length to the order of ~100 nm. Secondly, MBE conditions ensure perfect sticking at the surface, so that $\tau_d \to \infty$ and hence the adatom lifetime is fully determined by the crystallization lifetime $\tau = \tau_c$. In stationary conditions, the growth velocity then coincide with the deposition flux itself:

$$v(\boldsymbol{x}) = \Phi(\boldsymbol{x}) \tag{5.13}$$

In other words, all facets are expected to have the same incorporation factor $\chi = 1$. Deviations from eq. (5.13) can be ascribed to some diffusion exchange between neighboring facets since no material can escape from the crystal surface.

This picture of course over-simplifies the real growth dynamics. To get a better understanding of the actual growth rates of facets, a dedicated set of growth experiments was performed by introducing thin (20 nm) marker layers of AlGaAs at regular intervals during the deposition of GaAs (every 230 nm deposited). As shown in *Fig. 5.11* d), the TEM analysis of the pillar cross-section permits to distinguish the marker profiles at the different growth stages and hence to reconstruct the profile evolution leading to the final geometry. Interestingly, an accurate analysis of the distances between the marker lines in *Fig. 5.11* d), reveals that the growth rate of {113} facets at the beginning of the growth is rather small and abruptly increases when the (001) facet on the top disappears. A rough estimation of the growth rates indicates that v_{113} is equal to the deposition flux $\Phi_{113} = \Phi_0 \cos\alpha_{113} \approx$, as expected from eq. (5.13), only after the complete removal of the (001) facet, while in the initial stages it is reduced by $\sim$45%Φ_0. On the other hand, the actual growth rate of the (001), also determined from the markers in *Fig. 5.11* d), is larger than the nominal flux by $\sim$45%Φ_0. Moreover, a larger amount of material is accumulated at its borders than at the center. It is straightforward to conclude the existence of a significant transport of material from {113} facets towards the (001) flat region. In principle this should be included via a diffusion contribution as discussed for Ge/Si pillars (see Fig. 5.10), but because of the lack of experimental data we prefer to give a qualitative description by considering an effective extra flux contribution $\Delta\Phi$ $\sim$45%Φ_0 removing material from {113} facets and accumulating it uniformly on top of the (001) facets:

$$v_{113} = \Phi_{113} - \Delta\Phi \tag{5.14}$$

$$v_{001} = \Phi_{001} + \Delta\Phi \tag{5.15}$$

Notice that the growth rate of the (001) bottom of trenches is not modified by the additional flux here discussed and then grows at the nominal grow rate Φ_0.

5.3.2 Simulation results

First of all a simulation of growth for an isolated pillar was performed in order to determine the profile evolution without effects due to mutual shielding. The result is shown in Fig. 5.13 a) up to a deposition of 4 µm of GaAs. Facets move parallel to themselves according to the impinging flux as stated in eq.(5.13); the extra flux on {113} and (001) facets (eq. (5.14)) was included too. Due to the small flux impinging on the sidewalls the lateral growth of the pillar is rather limited. The growth of the substrate area closer to the pillar is partially shielded and hence a zone of partial depletion is formed. Notice that, due to the flux directionality, the effect of shadowing disappears at large distances from

the pillar, where no cutoff of the flux cone occurs, and the substrate grows conformal at the nominal flux Φ_0. By considering an array of pillars one close to each other, shadowing effects must be considered. As shown in Fig. 5.13 b), growth simulations capture the main features of experimental profiles, correctly accounting for both the lateral expansion and faceting on top. Notice in particular the inclination of {110} sidewalls compared to the isolated pillar in a), directly reflecting the mutual shielding of the flux cone. The capability of the growth model to reproduce the experimental behavior is made evident in Fig. 5.13 c) where calculated profiles are superimposed to the TEM image of the cross-section of the sample grown with AlGaAs markers, given in *Fig. 5.11* d). A close match of growth profiles is observed thus offering a confirmation of the main assumptions introduced in the model. Notice in particular that in agreement with experiments, the (001) flat top region quickly shrinks and disappear within the deposition of the first µm of GaAs. This offers a proof a posteriori of the accelerated motion of the (001) facets that in the simulations is accounted by the effective extra flux term of eq. (5.14).

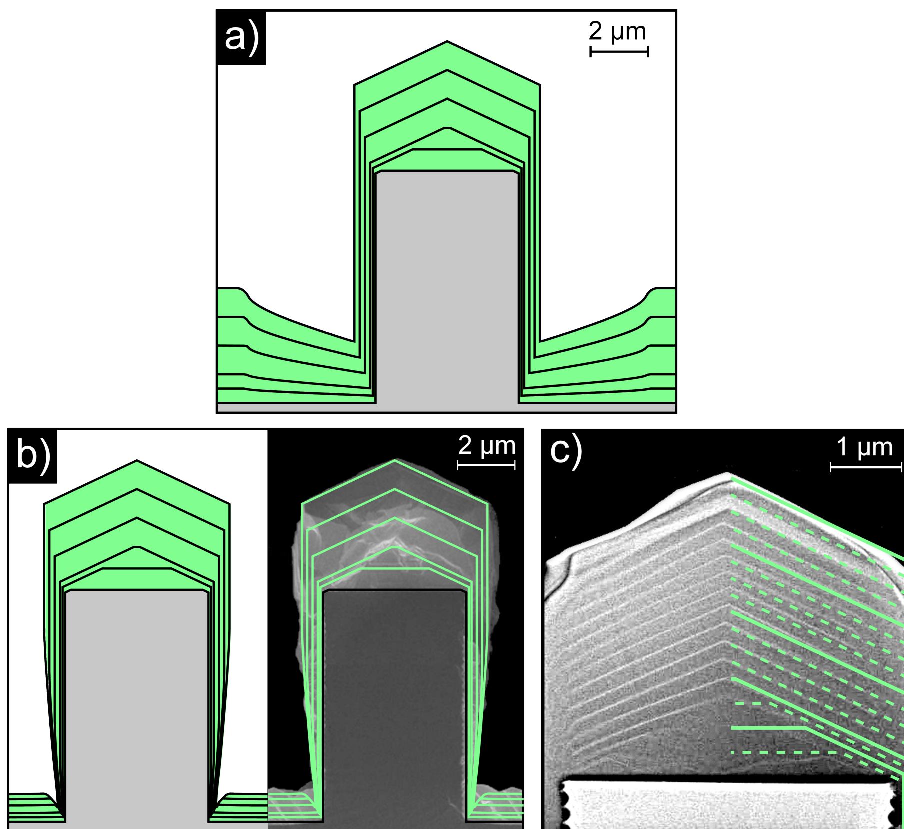

Figure 5.13: Results of growth simulations of GaAs on Si pillars 5 µm wide and 8 µm high at 580°C. In a) an isolated pillar is considered while in b) a squared pattern of pillars spaced by 4 µm trenches is reported and (on the right) profiles are superimposed to the SEM image of the pillar of Fig. 5.11 a). Profiles in a) and b) are obtained for deposition of the first 500 nm and for each µm deposited up to 4 µm. In c) simulation profiles (on the right side) are superimposed to the TEM cross-section of Fig. 5.11 d). A very good matching is observed between the experimental AlGaAs marker lines and the profiles predicted from the simulations at the same growth stages.

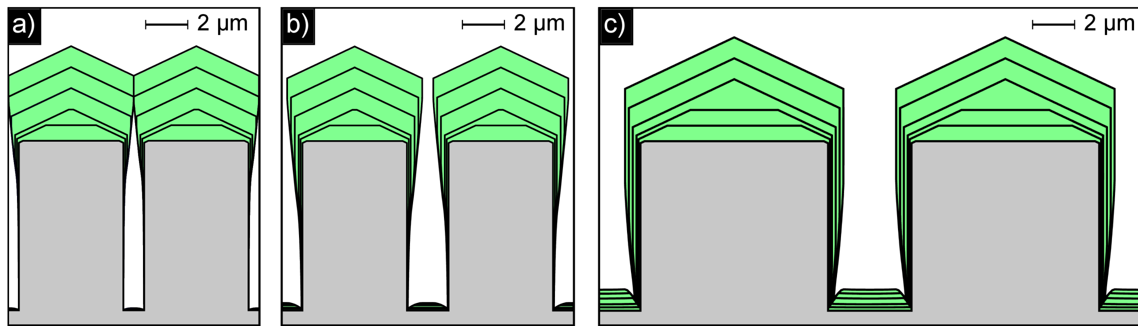

Figure 5.14: Simulation profiles for deposition of GaAs on different patterns of Si pillars (height 8 µm) for the same conditions used for Fig. 5.13. In a) and b) the Si pillar is 5 µm wide and a separation of 1 and 2 µm respectively is considered. In c) the initial Si pillar is 9 µm wide and a trench of 4 µm is considered. Profile lines are traced after deposition of the first 500 nm and for every µm of deposition up to a total of 4 µm.

By using the same parameters, it is then possible to inspect the effect of the pattern geometry. In particular, in Fig. 5.14 a) and b) simulation profiles are showed for different trench widths, 1 and 2 µm respectively, while 4 µm trenches were already considered in Fig. 5.13 b). As evident, trenches width determines the extent of the lateral growth by controlling the penetration of material toward the bottom, i.e. the mutual shadowing. For the narrowest trenches here considered (panel a), the material deposition on the initial Si pillar sidewalls is rather negligible and the lateral growth starts at its top leading to a quick closure of the gap. By considering larger trenches (panel b), a certain amount of material can attach deeper on the Si pillar sidewalls and eventually accumulate in the bottom of the trenches. Notice that the apparent inclination of the {110} sidewalls is almost the same in all cases so that the lateral growth at the same deposition stage is unchanged ($\sim$250 nm for each µm deposited). The effect of changing the Si pillar size can be inspected by comparing the profiles in Fig. 5.13 b), for a width of 5 µm, with those in Fig. 5.14 c), where the pillar width is increased to 9 µm. The global evolution is essentially the same, the only difference consists in the amount of material that must be deposited before the (001) top region disappears. While on 5 µm pillars it is extinguished after deposition of the first µm of GaAs, for 9 µm pillars this is delayed by one more µm, as obvious consequence of the larger flat region of the initial profile. No effect is observed on the relative growth rates so the growth on the wider pillar simply reproduce on a larger scale that of the narrow one but with a delay of $\sim$1 µm.

It is finally interesting to observe how the flux orientation θ_i can influence the pillars profile. In Fig. 5.15 a) the flux dependence on the facet angle is compared for different incidence angles. All curves are superimposed to the same cosine function, corresponding to vertical incidence (θ_i=0°), for small angles ($\alpha < 90° - \theta_i$) and then deviates from it when the surface crosses the deposition cone. Such deviations are toward larger values since the lost of a part of the cone is largely compensated by the alignment of some flux directions closer to the surface normal. For the higher value of θ_i shown in the plot (75°), this effect is

so strong that the maximum deposition flux occurs for a facet different from (001). Finally, the flux becomes zero for steeper facets ($\alpha > 90° + \theta_i$). The simulation profiles reported in panels b-d) of Fig. 5.15 show the different evolution expected at different incidence angles, θ_i=15°, 45°and 60°respectively. The evolution of the top regions are barely distinguishable since, according to Fig. 5.15, both Φ_{001} and Φ_{113} are the same. Large differences are instead evident in the extension of the lateral growth, determined both by the variations of Φ_{110}, increasing for larger θ_i, and by the different shadowing effect, possible only if the opening window gets smaller than the cone opening 90°$\pm\theta_i$. For θ_i=15°(b) {110} facets move very slowly and remains perfectly straight since their distance is enough to avoid mutual shielding on the sidewalls. The only region affected by the shadowing is the bottom of the trenches where a substantial accumulation of material is however still possible. Moving to θ_i=45°(c) a marked lateral expansion can be observed leading to a gradual closure of the pillar-pillar gap. The growth on the {110} sidewalls is clearly non uniform because of the shadowing effect so that the bottom grows much slower than the upper region leading to a conic expansion. The material reaching the bottom of the trenches is very small because of this stronger shadowing effect. For the largest value of θ_i=60°(d) finally the lateral expansion of the {110} facet becomes very fast but the stronger shadowing effect limits this only at the very top of the sidewalls. The gap is closed after the very first stages of the growth. At this short distance, shadowing effects occur also at the borders of the {113} facet that gets curved because of the smaller income of material. In these conditions, practically no material can reach the bottom of the trenches.

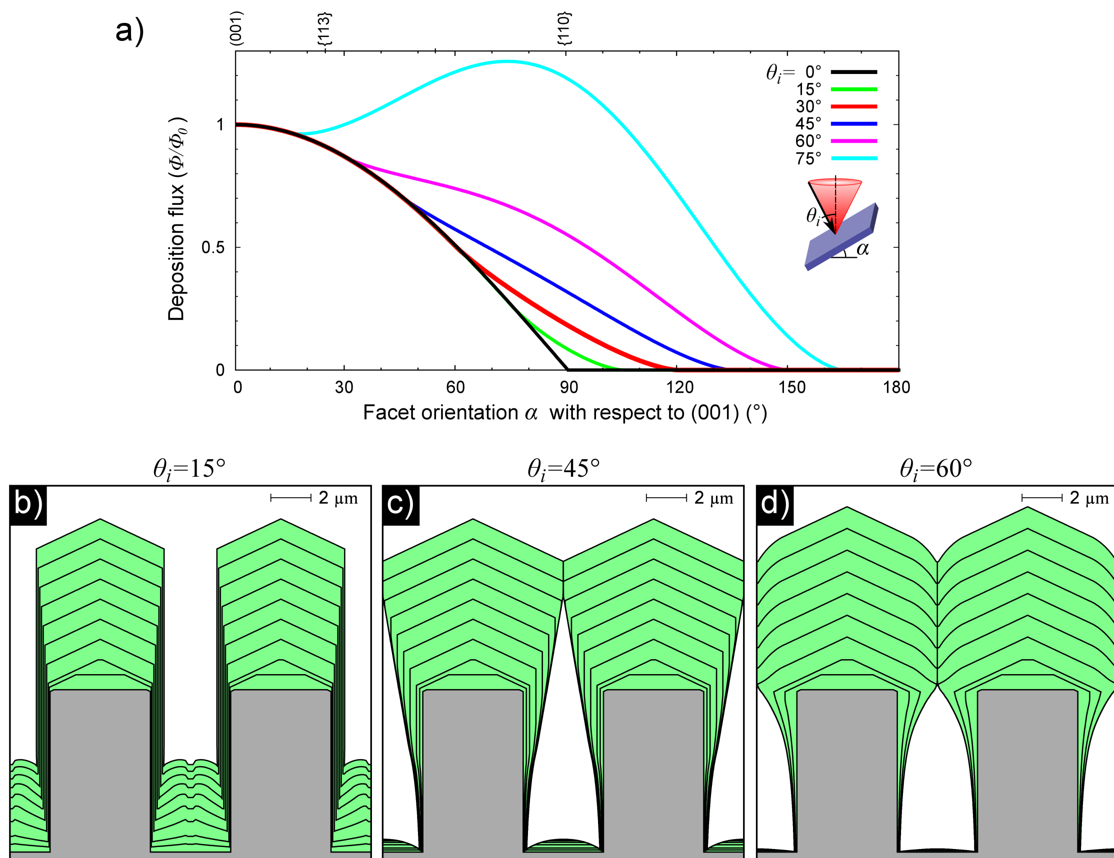

Figure 5.15: a) Deposition flux calculated as a function of the facet angle α with respect to the (001) plane for different incidence angles θ_i. Curves are normalized to have the same nominal flux on the (001) surface (0°). b-d) Simulations of the pillar growth for different incidence angles θ_i of the deposition flux. Profiles are reported after deposition of the first 500 nm and after every µm deposited, up to 8 µm. Initial Si pillars are 5 µm large and a gap of 4 µm is considered.

Conclusions

In the present Thesis different models have been discussed for the characterization of the growth processes in heteroepitaxial systems. In particular a distinction was introduced between systems grown in conditions close to equilibrium, dominated by thermodynamic driving force, and those evolving far from equilibrium, in conditions where kinetic effects prevail. In the former case the target of the modeling was the characterization of the processes involved in the Stranski-Krastanow growth, with particular reference to pit patterned profiles. In the latter case, the growth of micrometer size, three-dimensional crystals on a pillar patterned substrate was investigated.

Two different thermodynamic models have been considered, both accounting for the effects of surface energy, elastic energy and mixing entropy and considering a faster dynamics at the surface with respect to the bulk.

The first model implemented was Tersoff model, discussed in *Ch. 3*, based on the distinction between an evolving surface layer and the frozen-in bulk underneath. An extension of the approach already discussed in literature Refs. [22–24] was developed for the case of growth on patterned substrate, including a more realistic description of the different mobility of the two components, dependent on the local composition at the surface. The model was then applied to the growth of Ge/Si. A short review of simulation results for flat substrate was firstly reported, successfully reproducing the general phenomenology of Stranski-Krastanow, in agreement with the results in literature [23, 24]. Simulations were then performed for the growth of Ge on a Si pit-patterned substrate, resulting again in the expected phenomenology leading to the island growth into the pits in agreement with the experiments. More specifically, an anomalous effect of smoothing of the pit profile preceding the island growth was investigated and explained in terms of the activation of the motion of the Si in the substrate in consequence of the deposition of a small amount of Ge. In particular, according to simulation results, the enhancement of Si motion observed in the experiments was justified in terms of the lowering of its diffusion barrier on a Ge rich substrate, formed in the initial stages upon Ge surface segregation. Results here presented ended in the publication in Ref. [25]. The observed formation of islands eventually undergoing shape transitions captures the main effects of Stranski-Krastanow growth on patterned substrate but some aspects, such as the

composition profile of the islands, still demand for further investigation. An interesting aspect that was not accounted for in the present work and could be the object of future study could be the effect of different surface anisotropies of the two components as it is expected for real systems, in order to define how the evolution would be affected by the relative stability of different faceting. Also plastic effects mimicking the formation of dislocations into the island or in flat films could be another possible future application for the model as intermixing plays crucial role also for plastic relaxation.

The second thermodynamic model, discussed in *Ch. 4* [26], was an original phase-field description of the heteroepitaxial growth developed in order to extend Tersoff model to more complex situations. The implementation in a powerful phase-field framework with Finite Element Methods offers in fact the opportunity to overtake most of the limitations imposed by the simple Tersoff models, making possible to consider more complex geometries, eventually three-dimensional, with no restriction to shallow morphologies, and offering full access to the exact solution of the elastic problem coupled with the morphological and compositional evolution. In this Thesis no specific application of the model to physical problems was considered but the focus was on the model formulation itself supported by some simple case study as a proof of concepts. All the main aspects that were already part of Tersoff model were included in this new description and tested to properly reproduce the main aspects characterizing heteroepitaxial systems. At this point, we then proved the consistency of the model with previous literature, paving the way for the next application to the growth on patterned substrates and for more realistic geometries and physical parameters. This will be part of future work, demanding for a fine tuning of the numerical aspects determining the efficiency and stability of the simulations. With this respect, the development of the model into the proficient FEM solver AMDiS is expected allow high parallelization efficiency and strong optimization of the solution methods making possible the application of the approach here considered to a full, realistic, 3D system.

The kinetic approach in *Ch. 5* successfully allowed to characterize the growth of crystals on pillar patterned substrate for both Ge/Si [2] and GaAs/Si [38]. In particular the characteristic growth of this structures was found to be direct consequence of short diffusion lengths and mutual flux shielding between neighboring crystals. A close comparison between experimental profiles and results from simulations was considered for both systems and various growth conditions, showing a very good agreement. Despite the model was found to capture the qualitative behavior, some aspects of the growth are still unsolved demanding for additional extensions of the model. For example, an explanation of the actual mechanisms leading to self-alignment of the crystals or to their coalescence was not found so far. Moreove, the actual relation of the diffusion mechanisms between facets and the differences in the growth rates was only preliminary considered and demand for an additional work to motivate the definition of the kinetic parameters. In particular, the dependence on the growth conditions, was here established only by a fitting of the

experiments but surely a more physical analysis is required. Finally, an extension of the model to the full 3D case would be highly desirable in order to properly account for the competitive evolution of facets aligned in different directions on the growth plane, an effect that becomes unavoidable, in particular, for the characterization of the growth of GaAs/Si pillars at later growth stages, as a rotation of the facet system from {11n} to {10n} family was observed and cannot be handled in the simple 2D case. On the other hand, more experiments are planned to explore this growth modality in different conditions and also for different materials (e.g. GaN/Si or SiC/Si) so that the adaption of the model to such different case will constitute another possible application for the present treatment.

Notice that all the approaches here considered, even if mostly referred to the prototype Si-Ge system, are defined in a rather general way so that they can be in principle be extended to other similar systems.

In conclusion, it is important to underline that the separation between thermodynamic and kinetic system here considered was obviously an oversimplified picture of the growth processes, that proved to be effective for the specific systems here presented as the actual growth conditions therein were well suited for such two limiting cases. Evidently the evolution in many systems is expected to arise from the simultaneous effects of both thermodynamic driving forces and kinetic phenomenon increasing in this way the degrees of freedom of the growth process that are expected to characterize the real systems. The integration of the approaches discussed in *Ch. 2* and *Ch. 5* in a unified model is then an hoped-for perspective for the future developments as this would largely improve the possibilities to explore intermediate growth conditions, where the balance between thermodynamic and kinetic effects is expected to have a role in the system evolution.

List of publications

- R. Bergamaschini, F. Montalenti, and L. Miglio.
  "Optimal Growth Conditions for Selective Ge Islands Positioning on Pit-Patterned Si(001)".
  Nanoscale Res. Lett. **5**, 1873 (2010).

- R. Bergamaschini, M. Brehm, M. Grydlik, T. Fromherz, G. Bauer, and F. Montalenti.
  "Temperature-dependent evolution of the wetting layer thickness during Ge deposition on Si(001)".
  Nanotechnology **22**, 285704 (2011).

- C.V. Falub, H. von Känel, F. Isa, R. Bergamaschini, A. Marzegalli, D. Chrastina, G. Isella, E. Müller, P. Niedermann, and L. Miglio.
  "Scaling hetero-epitaxy from layers to three-dimensional crystals".
  Science **335**, 1330 (2012).

- R. Bergamaschini, J. Tersoff, Y. Tu, J. Zhang, G. Bauer, and F. Montalenti.
  "Anomalous Smoothing Preceding Island Formation During Growth on Patterned Substrates".
  Phys. Rev. Lett. **109**, 156101 (2012).

- R. Backofen, R. Bergamaschini, and A. Voigt.
  "The interplay of morphological and compositional evolution in crystal growth: A phase-field model".
  Euro. Phys. J. Spec. Topic (in press).

Bibliography

[1] J. Stangl, V. Holý, and G. Bauer, *Reviews of Modern Physics* **76**, 725 (2004).

[2] C. V. Falub, H. von Känel, F. Isa, R. Bergamaschini, A. Marzegalli, D. Chrastina, G. Isella, E. Müller, P. Niedermann, and L. Miglio, *Science* **335**, 1330 (2012).

[3] W. W. Mullins, *Journal of Applied Physics* **28**, 333 (1957).

[4] W. Carter, A. Roosen, J. W. Cahn, and J. Taylor, *Acta Metallurgica et Materialia* **43**, 4309 (1995).

[5] B. Li, J. Lowengrub, and A. Voigt, *Communications in Computational Physics* **6**, 433 (2009).

[6] Y.-W. Zhang, *Physical Review B* **61**, 10388 (2000).

[7] Y.-W. Zhang and A. F. Bower, *Applied Physics Letters* **78**, 2706 (2001).

[8] B. J. Spencer, P. W. Voorhees, and S. H. Davis, *Physical Review Letters* **67**, 3696 (1991).

[9] Y.-W. Zhang and D. J. Srolovitz, *Physical Review B* **70**, 041402(R) (2004).

[10] J.-N. Aqua and T. Frisch, *Physical Review B* **82**, 085322 (2010).

[11] G. Biasiol and E. Kapon, *Physical Review Letters* **81**, 2962 (1998).

[12] P. Liu, Y.-W. Zhang, and C. Lu, *Physical Review B* **68**, 195314 (2003).

[13] P. Liu, Y.-W. Zhang, and C. Lu, *Applied Physics Letters* **80**, 3910 (2002).

[14] P. Liu, Y.-W. Zhang, and C. Lu, *Applied Physics Letters* **90**, 071905 (2007).

[15] P. Liu, C. Lu, and Y.-W. Zhang, *Physical Review B* **76**, 085336 (2007).

[16] H. Wang, Y. Zhang, and F. Liu, *Journal of Applied Physics* **104**, 054301 (2008).

[17] X. Xu, J.-N. Aqua, and T. Frisch, *Journal of Physics: Condensed Matter* **24**, 045002 (2012).

[18] B. J. Spencer, P. W. Voorhees, and J. Tersoff, *Physical Review B* **64**, 235318 (2001).

[19] L. Klinger, *Acta Materialia* **50**, 3385 (2002).

[20] V. B. Shenoy, *Journal of the Mechanics and Physics of Solids* **59**, 1121 (2011).

[21] G. Vastola, V. B. Shenoy, J. Guo, and Y.-W. Zhang, *Physical Review B* **84**, 035432 (2011).

[22] J. Tersoff, *Applied Physics Letters* **83**, 353 (2003).

[23] Y. Tu and J. Tersoff, *Physical Review Letters* **93**, 216101 (2004).

[24] Y. Tu and J. Tersoff, *Physical Review Letters* **98**, 096103 (2007).

[25] R. Bergamaschini, J. Tersoff, Y. Tu, J. Zhang, G. Bauer, and F. Montalenti, *Physical Review Letters* **109**, 156101 (2012).

[26] R. Backofen, R. Bergamaschini, and A. Voigt, *Euro. Phys. J. Special Topics* (2012), in press.

[27] N. Provatas and K. Elder, *Phase-field methods in material science and engineering* (Wiley-vch, 2010).

[28] A. Rätz and A. Voigt, *Communications in Mathematical Sciences* **4**, 575 (2006).

[29] J. J. Eggleston, G. B. McFadden, and P. W. Voorhees, *Physica D* **150**, 91 (2001).

[30] A. Rätz and A. Voigt, *Nonlinearity* **20**, 177 (2007).

[31] S. Torabi, J. Lowengrub, A. Voigt, and S. Wise, *Proceedings of the Royal Society A* **465**, 1337 (2009).

[32] A. Rätz, A. Ribalta, and A. Voigt, *Journal of Computational Physics* **214**, 187 (2006).

[33] D.-H. Yeon, P.-R. Cha, and M. Grant, *Acta Materialia* **54**, 1623 (2006).

[34] Z. Bi and R. F. Sekerka, *Physica A* **261**, 95 (1998).

[35] W. J. Boettinger, J. A. Warren, C. Beckermann, and A. Karma, *Annual Review of Materials Research* **32**, 163 (2002).

[36] M. Ohtsuka and S. Miyazawa, *Journal of Applied Physics* **64**, 3522 (1988).

[37] S. Li, Q. Xiang, D. Wang, and K. L. Wang, *Journal of Crystal Growth* **157**, 185 (1995).

[38] S. Bietti, A. Scaccabarozzi, R. Bergamaschini, C. Frigeri, C. V. Falub, M. Bollani, E. Bonera, P. Niedermann, H. von Känel, S. Sanguinetti, and L. Miglio, Submitted.

[39] J. E. Ayers, *Heteroepitaxy of semiconductors* (CRC Press, 2007).

[40] I. Daruka and A.-L. Barabasi, *Physical Review Letters* **79**, 3708 (1997).

[41] E. A. Fitzgerald, *Materials Science Reports* **7**, 87 (1991).

[42] R. L. Schwoebel, *Journal of Applied Physics* **37**, 3682 (1966).

[43] A. A. Stekolnikov, J. Furthmüller, and F. Bechstedt, *Physical Review B* **65**, 115318 (2002).

[44] M. J. Beck, A. van De Walle, and M. Asta, *Physical Review B* **70**, 205337 (2004).

[45] P. Müller and R. Kern, *Applied Surface Science* **102**, 6 (1996).

[46] I. Berbezier and A. Ronda, *Surface Science Reports* **64**, 47 (2009).

[47] L. Miglio and F. Montalenti, *Silicon-germanium (SiGe) nanostructures: Production, properties, and applications in electronics*, edited by Y. Shiraki and N.Usami (Woodhead Publishing - UK, 2011).

[48] G. Vastola, R. Gatti, A. Marzegalli, F. Montalenti, and L. Miglio, "Self-assembled quantum dots," (Springer, 2008) Chap. Detailed Analysis of the Shape-dependent Deformation Field in 3D Ge Islands on Si(001), pp. 421–438.

[49] F. Montalenti, P. Raiteri, D. B. Migas, H. von Känel, A. Rastelli, A. Manzano, G. Costantini, U. Denker, O. G. Schmidt, K. Kern, and L. Miglio, *Physical Review Letters* **93**, 216102 (2004).

[50] G. Medeiros-Ribeiro, A. M. Bratkovski, T. I. Kamins, D. A. A. Ohlberg, and R. S. Williams, *Science* **279**, 353 (1998).

[51] F. M. Ross, R. M. Tromp, and M. C. Reuter, *Science* **286**, 1931 (1999).

[52] A. Vailionis, B. Cho, P. Desjardins, D. G. Cahill, and J. E. Greene, *Physical Review Letters* **85**, 3672 (2000).

[53] Y. W. Mo, D. E. Savage, B. S. Swartzentruber, and M. G. Lagally, *Physical Review Letters* **65**, 1020 (1990).

[54] M. Stoffel, A. Rastelli, J. Tersoff, T. Merdzhanova, and O. G. Schmidt, *Physical Review B* **74**, 1 (2006).

[55] E. Sutter, P. Sutter, and J. E. Bernard, *Applied Physics Letters* **84**, 2262 (2004).

[56] R. Bergamaschini, M. Brehm, M. Grydlik, T. Fromherz, G. Bauer, and F. Montalenti, *Nanotechnology* **22**, 285704 (2011).

[57] G.-H. Lu, M. Cuma, and F. Liu, *Physical Review B* **72**, 125415 (2005).

[58] A. Rastelli and H. von Känel, *Surface Science Letters* **515**, 493 (2002).

[59] G. Capellini, M. De Seta, Y. Busby, M. Pea, F. Evangelisti, G. Nicotra, C. Spinella, M. Nardone, and C. Ferrari, *Journal of Applied Physics* **107**, 063504 (2010).

[60] F. Zipoli, S. Cereda, M. Ceriotti, M. Bernasconi, L. Miglio, and F. Montalenti, *Applied Physics Letters* **92**, 191908 (2008).

[61] M. Brehm, M. Grydlik, H. Lichtenberger, T. Fromherz, N. Hrauda, W. Jantsch, and G. Bauer, *Applied Physics Letters* **93**, 121901 (2008).

[62] S. A. Chaparro, Y. Zhang, and J. Drucker, *Applied Physics Letters* **76**, 3534 (2000).

[63] A. Marzegalli, V. A. Zinovyev, F. Montalenti, A. Rastelli, M. Stoffel, T. Merdzhanova, O. G. Schmidt, and L. Miglio, *Physical Review Letters* **99**, 235505 (2007).

[64] J. Zhang, A. Rastelli, O. G. Schmidt, and G. Bauer, *Applied Physics Letters* **97**, 203103 (2010).

[65] D. Digiuni, R. Gatti, and F. Montalenti, *Physical Review B* **80**, 155436 (2009).

[66] Z. Zhong and G. Bauer, *Applied Physics Letters* **84**, 1922 (2004).

[67] G. Bauer, Z. Zhong, A. Halilovic, T. Fromherz, and F. Schäffler, *Applied Physics Letters* **82**, 4779 (2003).

[68] S. Kiravittaya, A. Rastelli, and O. G. Schmidt, *Applied Physics Letters* **87**, 243112 (2005).

[69] T. I. Kamins and R. S. Williams, *Applied Physics Letters* **71**, 1201 (1997).

[70] Z. Zhong, A. Halilovic, M. Mühlberger, F. Schäffler, and G. Bauer, *Applied Physics Letters* **82**, 445 (2003).

[71] G. Chen, H. Lichtenberger, G. Bauer, W. Jantsch, and F. Schäffler, *Physical Review B* **74**, 035302 (2006).

[72] J. Zhang, M. Stoffel, A. Rastelli, O. G. Schmidt, V. Jovanović, L. K. Nanver, and G. Bauer, *Applied Physics Letters* **91**, 173115 (2007).

[73] E. Lausecker, M. Brehm, M. Grydlik, F. Hackl, I. Bergmair, M. Mühlberger, T. Fromherz, F. Schäffler, and G. Bauer, *Applied Physics Letters* **98**, 143101 (2011).

[74] S. Watanabe, E. Pelucchi, B. Dwir, M. H. Baier, K. Leifer, and E. Kapon, *Applied Physics Letters* **84**, 2907 (2004).

[75] A. Pascale, I. Berbezier, A. Ronda, and P. C. Kelires, *Physical Review B* **77**, 075311 (2008).

[76] H. Hirayama, M. Hiroi, and T. Ide, *Physical Review B* **48**, 17331 (1993).

[77] S.-H. Lim, S. Song, E. Yoon, and J.-H. Lee, *Journal of Vacuum Science & Technology B* **22**, 275 (2004).

[78] G. Kozlowski, Y. Yamamoto, J. Bauer, M. A. Schubert, B. Dietrich, B. Tillack, and T. Schroeder, *Journal of Applied Physics* **110**, 053509 (2011).

[79] S. Y. Shiryaev, F. Jensen, L. Hansen, J. W. Petersen, and A. N. Larsen, *Physical Review Letters* **78**, 503 (1997).

[80] F. Montalenti, A. Marzegalli, G. Capellini, M. D. Seta, and L. Miglio, *Journal of Physics: Condensed Matter* **19**, 225001 (2007).

[81] R. Bergamaschini, F. Montalenti, and L. Miglio, *Nanoscale Research Letters* **5**, 1873 (2010).

[82] T. U. Schülli, G. Vastola, M.-I. Richard, A. Malachias, G. Renaud, F. Uhlík, F. Montalenti, G. Chen, L. Miglio, F. Schäffler, and G. Bauer, *Physical Review Letters* **102**, 025502 (2009).

[83] Z. Zhong, W. Schwinger, F. Schäffler, G. Bauer, G. Vastola, F. Montalenti, and L. Miglio, *Physical Review Letters* **98**, 176102 (2007).

[84] H. Lüth, *Surfaces and interfaces of solid materials*, 3rd ed. (Springer, 1995).

[85] T. Nishinaga, *Progress in Crystal Growth and Characterization of Materials* **48/49**, 104 (2004).

[86] C. Rosenblad, H. R. Deller, A. Dommann, T. Meyer, P. Schroeder, and H. von Känel, *Journal of Vacuum Science & Technology A* **16**, 2785 (1998).

[87] L. Onsager, *Physical Review* **37**, 405 (1931).

[88] L. Onsager, *Physical Review* **38**, 2265 (1931).

[89] A. Pimpinelli and J. Villain, *Physics of Crystal Growth* (Cambridge University Press, 1998).

[90] C. Herring, *Physical Review* **82**, 87 (1951).

[91] P. Müller and J. J. Métois, *Thin Solid Films* **517**, 65 (2008).

[92] D. B. Migas, S. Cereda, F. Montalenti, and L. Miglio, *Surface Science* **556**, 121 (2004).

[93] S. C. Lee, D. L. Huffaker, and S. R. Brueck, *Applied Physics Letters* **92**, 023103 (2008).

[94] P.-S. Wong, B. Liang, R. Molecke, J. Tatebayashi, and D. L. Huffaker, *Crystal Growth & Design* **10**, 2509 (2010).

[95] C. J. W and H. D. W, *Acta Metall.* **22**, 1205 (1974).

[96] D. W. Hoffman and J. W. Cahn, *Surface Science* **31**, 368 (1972).

[97] W. W. Mullins, *Journal of Applied Physics* **30**, 77 (1959).

[98] G. Wullf, *Z. Krystallogr.* **34**, 449 (1901).

[99] R. F. Sekerka, *Journal of Crystal Growth* **275**, 77 (2005).

[100] B. J. Spencer, *Physical Review E* **69**, 011603 (2004).

[101] L. D. Landau and E. M. Lifshitz, *Theory of Elasticity*, Course of Theoretical Physics, Vol. 7 (Elsevier, 1986).

[102] J. D. Eshelby, *Proceedings of the Royal Society A* **241**, 376 (1957).

[103] J. Tersoff and R. M. Tromp, *Physical Review Letters* **70**, 2782 (1993).

[104] V. A. Zinovyev, G. Vastola, F. Montalenti, and L. Miglio, *Surface Science* **600**, 4777 (2006).

[105] *Numerical Recipes: The Art of Scientific Computing*, 3rd ed. (Cambridge University Press, 2007) Chap. 12.

[106] R. J. Asaro and W. A. Tiller, *Metallurgical Transactions* **3**, 1789 (1972).

[107] M. A. Grinfeld, *Journal of Nonlinear Science* **3**, 35 (1993).

[108] D. Srolovitz, *Acta Metallurgica* **37**, 621 (1989).

[109] H. Gao and W. D. Nix, *Annual Review of Materials Science* **29**, 173 (1999).

[110] B. J. Spencer, P. W. Voorhees, and J. Tersoff, *Physical Review Letters* **84**, 2449 (2000).

[111] B. J. Spencer, P. W. Voorhees, and J. Tersoff, *Applied Physics Letters* **76**, 3022 (2000).

[112] B. P. Uberuaga, M. Leskovar, A. P. Smith, H. Jonsson, and M. Olmstead, *Physical Review Letters* **84**, 2441 (2000).

[113] J. Tersoff, B. Spencer, A. Rastelli, and H. von Känel, *Physical Review Letters* **89**, 196104 (2002).

[114] D. J. Godbey, J. V. Lill, J. Deppe, and K. D. Hobart, *Applied Physics Letters* **65**, 711 (1994).

[115] Y. W. Mo and M. G. Lagally, *Surface Science* **248**, 313 (1991).

[116] A. van de Walle, M. Asta, and P. W. Voorhees, *Physical Review B* **67**, 041308(R) (2003).

[117] L. Huang, F. Liu, and X. G. Gong, *Physical Review B* **70**, 155320 (2004).

[118] X. R. Qin, B. S. Swartzentruber, and M. G. Lagally, *Physical Review Letters* **85**, 3660 (2000).

[119] S. M. A. R. W. Balluffi and W. C. Carter, *Kinetics of Materials* (Wiley, New York, 2005).

[120] L. Huang, F. Liu, G.-H. Lu, and X. G. Gong, *Physical Review Letters* **96**, 016103 (2006).

[121] R. Kube, H. Bracht, J. L. Hansen, A. N. Larsen, E. E. Haller, S. Paul, and W. Lerch, *Journal of Applied Physics* **107**, 073520 (2010).

[122] J.-N. Aqua, T. Frisch, and A. Verga, *Physical Review B* **76**, 165319 (2007).

[123] J.-N. Aqua, A. Gouyé, T. Auphan, T. Frisch, A. Ronda, and I. Berbezier, *Applied Physics Letters* **98**, 161909 (2011).

[124] M. Ozdemir and A. Zangwill, *Journal of Vacuum Science & Technology A* **10**, 684 (1992).

[125] M. Grydlik, M. Brehm, F. Hackl, H. Groiss, T. Fromherz, F. Schäffler, and G. Bauer, *New Journal of Physics* **12**, 063002 (2010).

[126] B. J. Spencer and J. Tersoff, *Physical Review Letters* **79**, 4858 (1997).

[127] I. Daruka, J. Tersoff, and A.-L. Barabasi, *Physical Review Letters* **82**, 2753 (1999).

[128] J. Zhang, F. Montalenti, A. Rastelli, N. Hrauda, D. Scopece, H. Groiss, J. Stangl, F. Pezzoli, F. Schäffler, O. G. Schmidt, L. Miglio, and G. Bauer, *Physical Review Letters* **105**, 166102 (2010).

[129] S. Vey and A. Voigt, *Computing and Visualization in Science* **10**, 57 (2006).

[130] A. A. Wheeler, W. J. Boettinger, and G. B. McFadden, *Physical Review E* **47**, 1893 (1993).

[131] D. J. Seol, S. Y. Hu, Y. L. Li, J. Shen, K. H. Oh, L. Q. Chen, and W. Lafayette, *Metals and Materials International* **9**, 1 (2003).

[132] X. D. Liang, Y. Ni, and L. H. He, *Computational Materials Science* **48**, 871 (2010).

[133] R. F. Sekerka, *Crystal Research and Technology* **40**, 291 (2005).

[134] Y. Wang and J. Li, *Acta Materialia* **58**, 1212 (2010).

[135] K. Elder, M. Katakowski, M. Haataja, and M. Grant, *Physical Review Letters* **88**, 245701 (2002).

[136] K. R. Elder and M. Grant, *Physical Review E* **70**, 051605 (2004).

[137] Q. A, *Numerical Models for Differential Problems* (Springer, 2009).

[138] P. G. Ciarlet, *The Finite Element Method for Elliptic Problems*, Classics in Applied Mathematics, Vol. 40 (SIAM, 2002).

[139] R. H. Nochetto, *Proceedings of the International Congress of Mathematicians* , 2805 (2010).

[140] J. W. Cahn and J. E. Hilliard, *Journal of Chemical Physics* **28**, 258 (1958).

[141] K. E. Teigen, X. Li, J. Lowengrub, F. Wang, and A. Voigt, *Communications in Mathematical Sciences* **4**, 1009 (2009).

[142] D. J. Paul, *Semiconductor Science and Technology* **19**, R75 (2004).

[143] A. Madhukar, *Thin Solid Films* **231**, 8 (1993).

[144] T. H. Loh, H. S. Nguyen, C. H. Tung, A. D. Trigg, G. Q. Lo, N. Balasubramanian, D. L. Kwong, and S. Tripathy, *Applied Physics Letters* **90**, 092108 (2007).

[145] S. Fündling, U. Sökmen, E. Peiner, T. Weimann, P. Hinze, U. Jahn, A. Trampert, H. Riechert, A. Bakin, H.-H. Wehmann, and A. Waag, *Nanotechnology* **19**, 405301 (2008).

[146] P. Zaumseil, Y. Yamamoto, A. Bauer, M. A. Schubert, and T. Schroeder, *Journal of Applied Physics* **109**, 023511 (2011).

[147] E. A. Fitzgerald, G. P. Watson, R. E. Proano, D. G. Ast, P. D. Kirchner, G. D. Pettit, and J. M. Woodall, *Journal of Applied Physics* **65**, 2220 (1989).

[148] J.-S. Park, J. Bai, M. Curtin, B. Adekore, M. Carroll, and A. Lochtefeld, *Applied Physics Letters* **90**, 052113 (2007).

[149] J. Bai, J.-S. Park, Z. Cheng, M. Curtin, B. Adekore, M. Carroll, A. Lochtefeld, and M. Dudley, *Applied Physics Letters* **90**, 101902 (2007).

[150] M. Ohtsuka and A. Suzuki, *Journal of Applied Physics* **73**, 7358 (1993).

[151] M. Ohtsuka, *Journal of Crystal Growth* **205**, 112 (1999).

[152] W. Wegscheider, L. Pfeiffer, and K. West, *Simulation of Molecular-Beam epitaxial growth over nonplanar surfaces*, edited by K. Eberl, P. M. Petroff, and D. Piet, Low dimensional structures prepared by epitaxial growth or regrowth on patterned substrates. NATO ASI series: Series E (Kluwer Academic Publishers, 1995) pp. 283–290.

[153] Q. Xiang, S. Li, D. Wang, K. L. Wang, J. G. Couillard, and H. G. Craighead, *Journal of Vacuum Science & Technology B* **14**, 2381 (1996).

[154] D. W. Shaw, *Journal of Crystal Growth* **47**, 509 (1979).

[155] S. Jones, L. K. Siedel, and K. M. Lau, *Journal of Crystal Growth* **108**, 73 (1991).

[156] K. Shiraishi, Y. Y. Suzuki, H. Kageshima, and T. Ito, *Applied Surface Science* **130-132**, 431 (1998).

[157] M. Rondanini, S. Cereda, F. Montalenti, L. Miglio, and C. Cavallotti, *Surface and Coatings Technology* **201**, 8863 (2007).

[158] M. Rondanini, C. Cavallotti, D. Ricci, D. Chrastina, G. Isella, T. Moiseev, and H. von Känel, *Journal of Applied Physics* **104**, 013304 (2008).

[159] A. Oshiyama, *Physical Review Letters* **74**, 130 (1995).

[160] L. Vescan, K. Grimm, and C. Dieker, *Journal of Vacuum Science & Technology B* **16**, 1549 (1998).

[161] J.-S. Park, J. Bai, M. Curtin, M. Carroll, and A. Lochtefeld, *Journal of Vacuum Science & Technology B* **26**, 117 (2008).

Acknoledgements

First of all I acknowledge Cariplo foundation for the continuous financial support to my PhD. Special thanks are due to Prof. G. P. Brivio.

I am grateful to my supervisor Prof. F. Montalenti for his constant support and precious indications and to Prof. Miglio for his helpful suggestions and support.

I also deeply thank Prof. A. Voigt, for hosting me for six months in his group, teaching me about phase-field and AMDiS FEM code. My gratitude goes also to the members of his group, in particular to R. Backofen, who actively supported me during the work.

I sincerely thank J. Tersoff for all the precious discussions and enlightening hints during all my PhD work.

I also acknowledge Prof. G. Bauer and J. Zhang, Prof. H. von Känel and Dr. C. Falub, and Prof. S. Sanguinetti, who provided a constant support for the experimental data.

Special thanks are for my office colleagues in Milano.

Finally, I cannot avoid to thank my family and above all my girlfriend.